ABSTRACT

Title of Dissertation: Probing the Dynamics of Ultra-Fast Condensed State Reactions in Energetic Materials

Nicholas W. Piekiel, Doctor of Philosophy, 2012

Directed By: Michael R. Zachariah, Professor
Department of Mechanical Engineering and Chemistry

Energetic materials (EMs) are substances with a high amount of stored energy and the ability to release that energy at a rapid rate. Nanothermites and green organic energetics are two classes of EMs which have gained significant interest as they each have desirable properties over traditional explosives. These systems also possess downfalls, which could potentially be overcome if more were understood about the nature of their reactions. However, ultra-fast reactions are prominent during ignition and combustion, and increase the difficulty in probing the initial and intermediate reaction steps. The goal of this study is to probe the early phases of reaction in nanothermites and green EMs, and to do so we have developed a Temperature-Jump/Time-of-Flight Mass Spectrometer (T-Jump/TOFMS) capable of rapid sampling and heating rates. Various nanothermites have been investigated with this system, and analysis has shown that nanothermite ignition is dependent on the decomposition of the metal oxide, and in certain systems there is distinct evidence of condensed phase initiation. Carbon/metal oxide mixtures, which have application to chemical looping combustion, were also investigated and further demonstrate condensed phase reaction. Aside from mass

spectrometry, complementary high heating rate SEM/TEM, pressure cell, and optical experiments were also performed.

Many organic energetics including a variety of tetrazole containing ionic salts have also been examined. To investigate the breakdown of the tetrazole ring, a common substructure in green organic energetics, several tetrazole containing salts with minor variations in either functional group or anion composition were studied. Two main tetrazole decomposition pathways were identified and are affected by the placement of functional groups along the tetrazole ring. Many differences were also observed in comparison to previous works at slow heating rates due to either different reaction processes or the presence of secondary reactions in the previous studies. A μ-DSC experiment showed a decrease in activation energy for tetrazole containing materials under high heating rates, further suggesting different mechanistic processes are at play.

Probing the Dynamics of Ultra-Fast Condensed State Reactions in Energetic Materials

By

Nicholas William Piekiel

Dissertation submitted to the Faculty of the Graduate School of the
University of Maryland, College Park in partial fulfillment
of the requirements for the degree of
Doctor of Philosophy
2012

Advisory Committee:

Professor Michael Zachariah (Chair)
Professor Bryan Eichhorn
Professor Gregory Jackson
Professor Peter Sunderland
Professor Kenneth Yu

To my family and friends who have given their unconditional support.

Thank you.

Acknowledgements

I would like to thank my thesis advisor, Dr. Michael Zachariah, for his guidance and support throughout my studies. His advisement has been an invaluable resource and has truly made me a better person, personally and professionally. Thank you to my lab mates, particularly Lei Zhou and Kyle Sullivan for their leadership in the early stages of my thesis, and all others for their years of help and suggestions. I would also like to acknowledge Richard Cavicchi for his generosity in assistance and use of the micro-calorimetry setup. Thank you to my advisory committee as their ideas and recommendations have been crucial to the completion of this process. Lastly, none of this work would be possible without the financial support of the Office of Naval Research and their University/Laboratory Initiative program, the Army Research Office, the Army Research Laboratory, the Defense Threat Reduction Agency and the National Energy Technology Laboratory.

Table of Contents

List of Tables

Chapter 2

Chapter 5

Chapter 6

Chapter 7

Chapter 8

List of Figures

Chapter 1

Chapter 2

Chapter 3

Chapter 4

Chapter 5

Chapter 6

Chapter 7

Chapter 8

List of Abbreviations

EM	Energetic Material
GEM	Green Energetic Material
T-Jump	Temperature Jump
TOFMS	Time-of-Flight Mass Spectrometry
TGA	Thermogravimetric Analysis
DTA	Differential Thermal Analysis
DSC	Differential Scanning Calorimetry
FTIR	Fourier Transform Infrared Spectroscopy
MCP	Micro-Channel Plate
SEM	Scanning Electron Microscopy
TEM	Transmission Electron Microscopy
EDS	Energy-Dispersive X-ray Spectroscopy
CLC	Chemical Looping Combustion

List of Material Abbreviations

RDX	Research Department Explosive (Cyclotrimethylenetrinitramine)
HMX	Cyclotetramethylenetetranitramine
PETN	Pentaerythritoltetranitrate
CL-20	Hexanitrohexazaisowurtzetane (HNIW)
TNT	Trinitrotoluene
5-AT	5-amino-1H-tetrazole
MeHAT_DN	5-amino-1-methyl-1*H*-tetrazolium dinitramide
MeDAT_DN	1,5-diamino-4-methyl-1*H*-tetrazolium dinitramide
DAT_N	1,5-diamino-1*H*-tetrazolium nitrate
MeDAT_N3	1,5-diamino-4-methyl-1*H*-tetrazolium azide
HAT_DN	5-aminotetrazolium dinitramide

List of Publications

N.W. Piekiel and M.R. Zachariah. *Decomposition of Aminotetrazole Based Energetic Materials under High Heating Rate Conditions.* Journal of Physical Chemistry A, 116 (6), pp 1519-1526. (2012).

N. W. Piekiel, R. E. Cavicchi, and M. R. Zachariah. *Rapid-Heating of Energetic Materials using a Micro-Differential Scanning Calorimeter.* Thermochimica Acta, 521, 125 (2011).

K.T. Sullivan, **N.W. Piekiel**, C. Wu, S. Chowdhury, S. T. Kelly, T.C. Hufnagel, Kamel Fezzaa, and M.R. Zachariah. *Reactive Sintering: An important Component in the Combustion of Nanocomposite Thermites.* Combustion and Flame, 159, 2-15. (2012). (**Feature Article**).

K. Sullivan, **N. Piekiel**, S. Chowdhury, C. Wu, C. Johnson, M.R. Zachariah. *Ignition and Combustion Characteristics of Nanoscale Al/AgIO3: A Potential Energetic Biocidal System*. Combustion Science and Technology, 183, 205. (2011).

L. Zhou, **N. Piekiel**, S. Chowdhury, M.R. Zachariah. *Time Resolved Mass Spectrometry of the Exothermic Reaction between Nanoaluminum and Metal Oxides: The Role of Oxygen Release*. J. Physical Chemistry C, 114, 14269. (2010).

G. Young, **N. Piekiel**, S. Chowdhury, and M. R. Zachariah. *Ignition Behavior of a-Alane*. Combustion Science and Technology, 182, 1341, (2010).

S. Chowdhury, K. Sullivan, **N. Piekiel**, L. Zhou and M. R. Zachariah. *Diffusive vs. Explosive Reaction at the Nanoscale*. J. Phys. Chem. C, 114, 9191. (2010)

L. Zhou, **N. Piekiel**, S. Chowdhury, D. Lee and M. R. Zachariah. *Transient ion ejection during nanocomposite thermite reactions*. Journal of Applied Physics, 106, 083306, (2009).

L Zhou, **N. Piekiel**, S. Chowdhury, and M.R. Zachariah. *T-Jump/Time-of-Flight Mass Spectrometry for Time Resolved Analysis of Energetic Materials.* Rapid Communications in Mass Spectrometry, 23, 194, (2009).

N.W. Piekiel, L. Zhou, K.T. Sullivan, and M.R. Zachariah. *Initiation and reaction in Al/Bi_2O_3: Evidence for Condensed Phase Chemistry.* In progress.

N.W. Piekiel and M.R. Zachariah. *Evidence for Condensed Phase Initiation for Carbon/Metal Oxide Nanocomposites.* In progress.

N.W. Piekiel, and M.R. Zachariah. *The Decomposition of Potential Green Energetic*

Materials Under Rapid Heating Rates. In progress

Chapter 1: Introduction

1.1. Motivation

1.1.1. The Development of Energetic Materials

Energetic materials (EMs) can be loosely defined as substances with a significant amount of potential energy that also rapidly react to release that energy. From this definition a large number of materials could be classified as EMs, but in the context of this work energetic materials are considered to be substances used as propellants, pyrotechnics, or explosives. One of the first energetic materials, gunpowder (black powder), is reported to date back to as early as 220 BC China [1]. In the 13th century gunpowder was brought to Europe [1, 2] and eventually became the first mass produced energetic material. Due to its ease of use, relative safety, and diversity as an energetic material, gunpowder was the prominent EM until the mid-1850's. As technology advanced, the desire for a 'jack of all trades' material was replaced by the need for materials to meet specific applications. The main requirement at that time was a more powerful material, one could that could produce more energy in a shorter timespan than gunpowder. Thus by early in the 20th century a number of notable EMs, including nitroglycerine (the energetic foundation of dynamite), PETN (pentaerythritoltetranitrate), RDX (cyclotrimethylenetrinitramine), and TNT (trinitrotoluene) had all emerged [2]. These materials are called high explosives as they detonate during combustion, and most of them are commonly used today. These were of course some of the few successes out of many attempts to create new materials, yet these successes showed some of what could

be done in this field. This helped to push the field of energetic materials as with each new material came the question, how can we make this material better? The goal to create a material with greater explosive properties has continued to this day, peaking in 1986 with the discovery of CL-20 [3].

Despite over a century of work to create better energetic materials, some of the most common high explosives today are RDX and HMX which were originally discovered in 1899 and 1930, respectively [2]. There are many factors that have kept these materials relevant including cost, availability, and stability, combined with their energetic properties. However, at this point there should be concern with the lack of success in developing new materials. To address this issue, more attention needs to be lent to investigation of how these materials work. Even for materials like RDX that have been extensively studied, there still exists uncertainty in the reaction mechanisms. A more thorough knowledge of how these materials form their final reaction products would provide the information to more effectively design new materials. If the individual steps of the molecular breakdown of an energetic material are known, then it may be possible to tune that material to react in a certain way. This seems like a relatively simple solution, but the nature of energetic materials and their ultra-fast reactions make this a formidable task. Traditional experiments for characterization of energetic reactions work at a timescale that is orders of magnitude greater than the reaction of the energetic material itself (microseconds). Therefore new methods are desired to investigate the reactions of energetic materials at a rapid timescale to probe the initial and intermediate events.

1.1.2. New Energetic Materials

This question of 'how can we make this material better?' continues to drive the field of energetics, but the definition of 'better' has evolved. While the performance of EMs has come a long way, current research also focuses on other aspects of the material, including the stability, environmental impact, and ability to tune the reaction. These factors have led to the pursuance of two classes of EM, thermites and 'green' energetics. Thermites, typically a mixture of particles of aluminum and metal oxide, fall in line with the goal of creating a material with a greater energy output. A typical thermite can have a higher potential energy than even CL-20 as shown in Figure 1.1. This figure shows the energy release per unit volume and per unit mass for a variety of thermites and high explosives. It can be seen that, especially on a per unit volume basis, the nanothermites have the potential to outperform CL-20, the current benchmark in EM performance. Unfortunately, thermites typically react much slower than traditional high explosives limiting the rate of energy release. However, thermites have further potential in that they are highly tunable, and therefore many of their reactive properties such as ignition temperature, burn rate, and sensitivity can be changed by the variation of stoichiometry, packing density, or oxidizer composition. This has led to the use of thermites in propellant and pyrotechnic applications, and their high amount of stored energy gives them further potential if the gap in reaction rate can be bridged.

'Green' energetic materials (GEMs) have been developed with the goal of improving the overall environmental impact of energetic materials. This includes all aspects of the material's life with particular focus on the formation of environmentally benign reaction products. Materials such as RDX and HMX have been known to be

hazardous at different stages of their lifetime [4]. Ideally a material could be made that supplant these materials from an energetics standpoint, without having the same negative environmental impact.

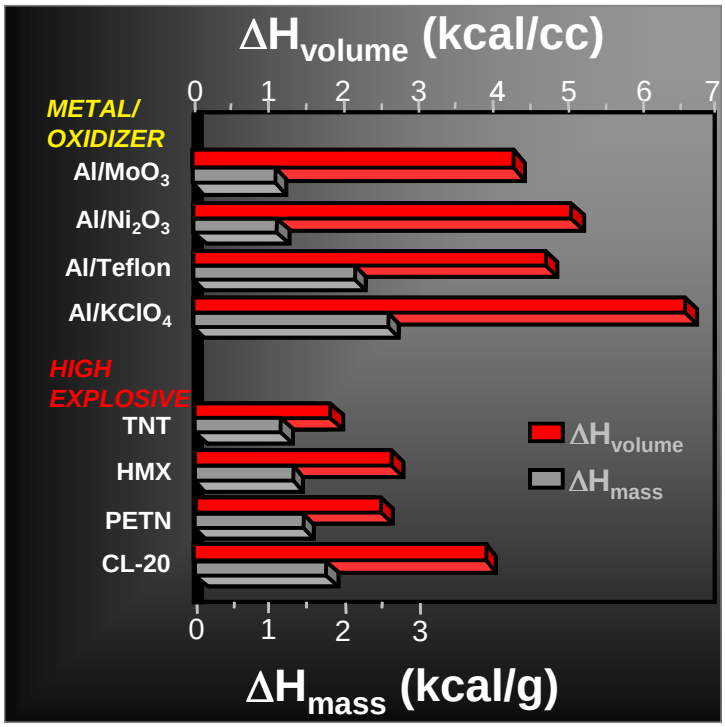

Figure 1.1: Energy release per unit of volume or mass for various thermites and high explosives (this image is from Fischer and Grubelich [5]).

Both thermites and GEMs have the potential to significantly change the current field of energetic materials. As with the formulation of new materials, more information on the decomposition and reaction of these materials could greatly enhance the overall understanding of how they work on a bulk scale, and thus lead to improvements in their functionality.

1.2. Nanothermites

Aluminum is the typical fuel of nanothermite systems due to its relative abundance, low cost, and high amount of stored energy. Metal oxide nanoparticles provide the oxidizer for the system and can be made up of a wide variety of oxides, which all have unique physical, chemical, and electrical properties, and will have different effects on the thermite reaction. Traditional thermite materials were made with micron sized particles, and burned very slowly compared to traditional organic energetics. This issue was addressed by shifting from micro-sized particles to nanoparticle systems, which led to the term nanothermites. It was found that a decrease in primary particle size in thermite composites from the micro to the nanoscale, increased burn rates in burn tube and open tray experiments by up to three orders of magnitude [6-8]. This enhancement is due to decreased diffusion lengths and an increase in surface area of the reactants. This improvement in performance over the traditional microscale thermites brings the reaction rates closer to that seen in organic EMs. If the reaction rate of nanothermites could be increased even further, then it may be possible to formulate nanothermite high explosives. This would be a considerable accomplishment due to the amount of potential energy in nanothermites.

However, due to an inherent oxide shell on the aluminum nanoparticles made up of inert Al_2O_3 (alumina), there is a limit to how small the primary nanoparticles can be before the Al_2O_3 starts to detrimentally affect the thermite reaction. Ideally the fuel and oxidizer in a thermite would be mixed as intimately as in an organic energetic, but our current technology limits this process. Since nanothermites show considerable promise in the energetics field, and are composed of materials that are relatively cheap and readily

available, there is a push to gain a greater understanding of the reaction and initiation mechanisms of these materials. This will hopefully enhance the ability to tune these systems for optimal performance in a variety of applications.

1.2.1. Aluminum Combustion

Given the central role that nanoaluminum plays in nanothermites many efforts have been dedicated to understanding its combustion. Due to a large number of potential experimental variations, results on aluminum combustion may differ significantly.

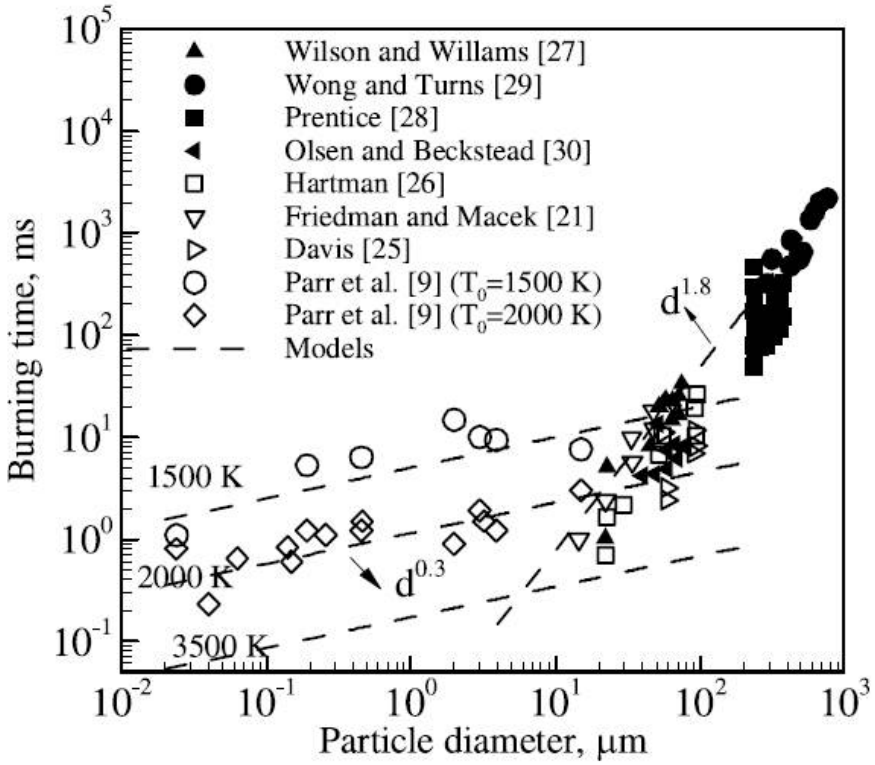

Figure 1.2: The burning time of aluminum particles as a function of diameter (this image is from Huang *et al.* [9]).

Figures 1.2 and 1.3 show some examples of how the combustion kinetics of Al nanoparticles differ from microparticles, as the burn time and ignition temperature are

both experimentally shown to be lower in nanoparticles. The question remains, why do nanoparticles burn differently, and how do they actually initiate their ignition and combustion processes. Since aluminum nanoparticles show substantially different characteristics than micron-sized particles, and are primarily used in nanothermites, focus will remain on Al nanoparticle combustion.

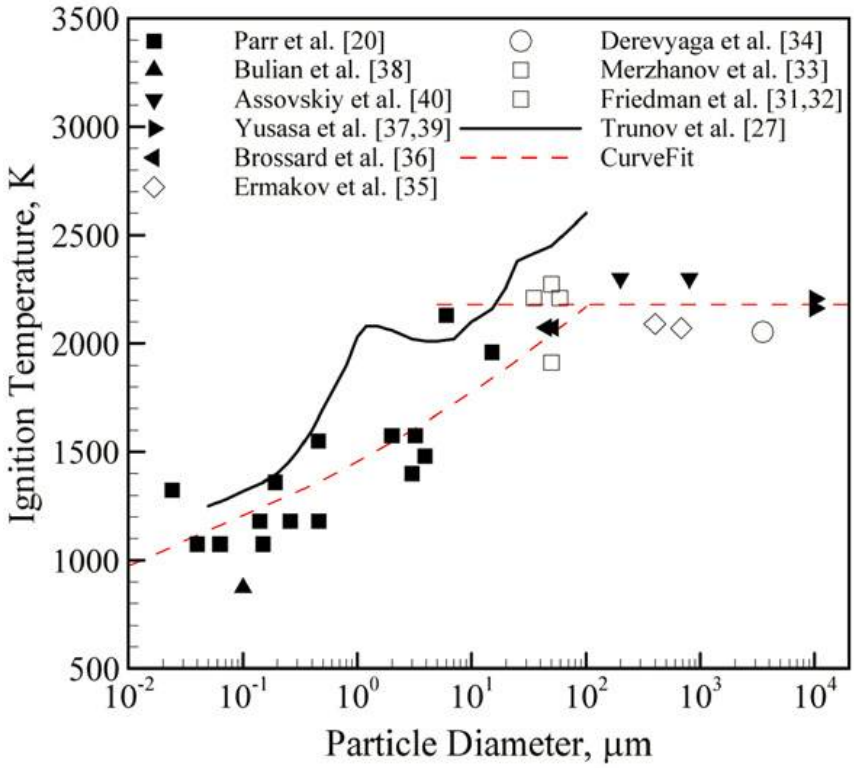

Figure 1.3: Particle ignition temperatures as a function of particle size (this image is from Huang *et al.* [10]).

Much attention has been given to understanding the transport of aluminum with respect to its Al_2O_3 shell. Figure 1.4 shows a TEM image of the inherent Al_2O_3 of an aluminum nanoparticle. This shell is typically 2-3 nm in thickness, but can be grown larger in different environments. The Al_2O_3 shell acts as a protective barrier for the aluminum fuel and prevents complete oxidation. For the underlying aluminum to react

with and oxidizer, it must either escape from the Al_2O_3 shell, or an oxidizer must diffuse through. During slow heating, aluminum ions can diffuse outwards out of the Al_2O_3 shell, and O_2 can diffuse inwards, thus making the reaction diffusion controlled.

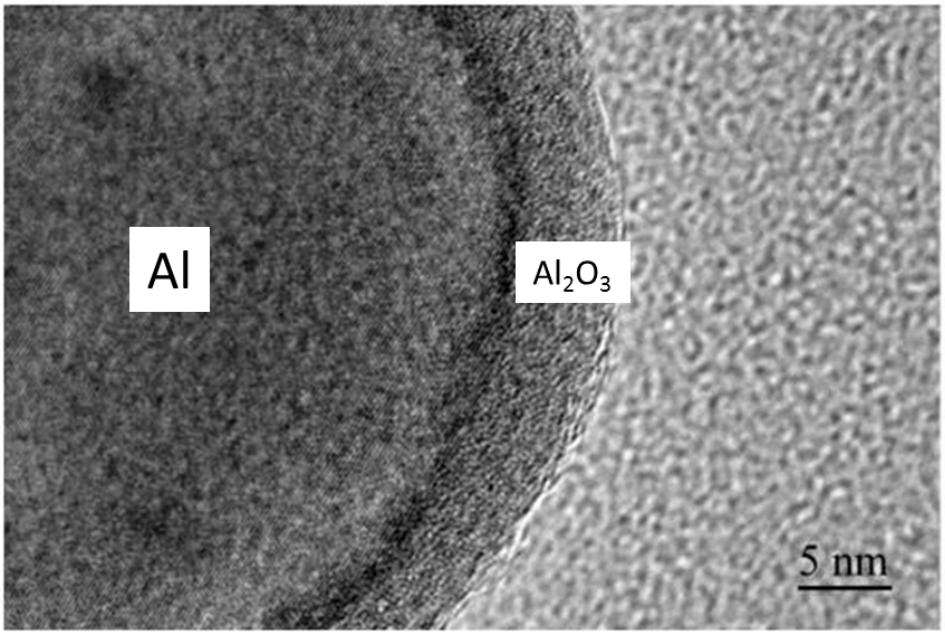

Figure 1.4: TEM image of aluminum ~50nm aluminum nanoparticle (this image is from Sullivan [11]).

If the aluminum nanoparticle is rapidly heated, the nearly instantaneous melting of the aluminum could have considerable effects in aiding the transport processes. The exact nature of aluminum transport in this case is not known, but several models have been proposed.

Levitas *et al.* [7, 12] suggest that aluminum escapes from the oxide shell via a "melt dispersion" mechanism. This mechanism proposes that under rapid heating conditions as the aluminum core melts and the alumina shell remains in the solid phase, the aluminum volumetrically expands by up to 6% creating a strong, repulsive force on the outer shell. This force causes rupturing of the Al_2O_3 shell and results in an unloading

wave through the molten Al, which causes spallation into bare Al clusters travelling at speeds of up to 250 m/s. Based on a more moderate heating rate experiment, Rai *et al.* [13] proposed a diffusion based model to help explain the appearance of hollow core aluminum particles after heating. They suggest that there are two regimes, a fast and slow oxidation regime where the oxidation respectively occurs above and below the melting point of Al. The slow heating regime occurs when the Al core is still in the solid phase and is dependent on oxygen diffusion through the Al_2O_3 core, while the fast oxidation occurs after the melting of Al and depends on the diffusion of both oxygen and aluminum, and can be further enhanced by breaking of the alumina shell. While Levitas [7, 12] suggests that the extreme pressure within the alumina shell causes spallation of the aluminum core, Rai [13] suggests that this pressure serves to enhance the diffusion through the shell. For Al nanoparticle ignition, an alumina shell breaking mechanism is also suggested by Trunov *et al.* [14]. This mechanism is designed to explain the burning of a wide variety of aluminum particles, at the micro or nanoscale, and is based on the varying morphology of the Al_2O_3 shell. For nanoparticles they suggest that the alumina shell can quickly shift from the natural amorphous phase to γ-phase crystals that produce gaps in the shell exposing the bare aluminum for oxidation.

The method of aluminum transport through the Al_2O_3 shell has been a topic of much debate, but regardless, it can be concluded that rapid heating of an aluminum particle will have an enhancing effect on the transport of aluminum. With improved transport of aluminum comes the ability to oxidize faster and to shift the reaction towards an ultra-fast, kinetically controlled reaction. In some nanothermite systems, where rapid combustion occurs, inherent heating rates can reach up to 10^6 K/s. Thus self-heating of

the nanothermite allows for fast transport processes and further promotes reaction. Since some of these reactions occur very rapidly with high energy release, it is difficult to investigate the intermediate steps of the reaction.

1.2.2. Oxide Role in Nanothermites

The nanothermite reaction is a two-component process as an aluminum fuel and an oxidizer must be present. Common oxides in the nanothermites are CuO, Fe_2O_3, Bi_2O_3, and MoO_3, each of which creates a unique reaction. Differences include ignition temperature, reaction rate, gas production, flame temperature, etc., and these differences are caused by the different properties of the oxides. In particular, two major properties that can affect the nanothermite reaction are the oxide's ability to produce a mobile oxidizer, and the temperature at which this oxidizer is formed. The phase of the oxidizer is also important as it will affect the transport process.

Several other factors also play a role in the reaction including the order of events. For example, if an oxide can produce an abundance of free O_2, which is typically advantageous, at what temperature will this occur? If the O_2 is released at 600 K, but aluminum does not escape its Al_2O_3 shell until 933 K, then it is possible that the majority of O_2 will diffuse away prior to reaction. It is also necessary for the metal oxide to produce a “free” oxidizer, as in the oxidizer must be readily available for transport to the aluminum. This transport process could occur in either the condensed phase or the gas phase and may be different for each oxidizer, but regardless it must be a fast process to sustain a rapid nanothermite reaction. Thermodynamically, the metal oxide could also affect the maximum temperature of the reaction if it forms a product that is difficult to

melt or vaporize. The final temperature is limited as energy is used for the phase change processes, which can therefore limit the reaction rate, as a higher temperature promotes a faster reaction. In some nanothermite systems the aluminum can be vaporized, resulting in a greatly enhanced reaction. However, if energy is spent on phase change processes of metal oxide products, this may not be possible.

1.3. "Green" Energetic Materials (GEMs)

Many of the traditional organic EMs have been thoroughly researched, but the recent shift towards environmentally friendly materials has brought many new formulations. Some GEMs have the energetic properties to replace current EMs, but more must be understood about their performance and stability. With these materials concern is given to the synthesis, storage, and combustion of the material, and how each of these steps in the material's lifetime can damage the environment.

A recent goal for the combustion process is to reduce the formation of harmful reaction products. In some GEMs this is performed by using high nitrogen content materials that have high heats of formation and create energy by breaking their many N-N bonds. Many materials release energy by forming carbon containing products with negative heats of formation. The goal of using high nitrogen/low carbon content materials is to prevent the production of harmful carbon containing reaction products (CO) and produce relatively benign nitrogen containing products (N_2). One common structure used for this is the tetrazole ring, which can be modified to accept various functional groups. The tetrazole structure can also be positively charged relatively easily so that it can be paired with a functional anion. When paired with an anion a relatively stable

energetic salt is formed. Figure 1.5 is an example of a tetrazole containing cation (right side) paired with a nitrate anion. These materials such have negligible vapor pressures, and are well suited for energetic applications.

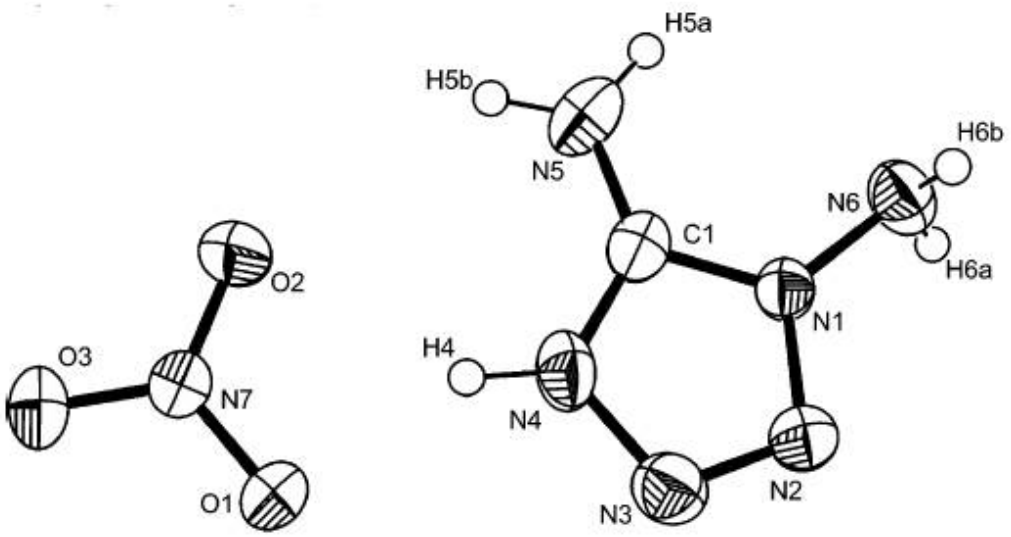

Figure 1.5: Molecular structure for 1,5-diamino-1*H*-tetrazolium nitrate (this image is from Galvez-Ruiz *et al.* [15]).

Typical energetic material characterization methods can determine the final reaction products that are formed, but the uncertainty lies in *how* those products are formed. By understanding the initiation and decomposition of green energetics, one can identify *how* the reaction products are formed. With knowledge of the decomposition pathways, it may be possible to formulate materials to produce certain benign reaction products. The synthesis process for these materials, while typically complex, is highly tunable so that slight variations in molecular structure are possible. These slight variations can have significant effects on the decomposition mechanism and can promote different reaction products. For example, with the tetrazole containing salts, if a functional group on the tetrazole ring is removed or replaced with a different molecule,

what effect will this have on the overall decomposition? Unfortunately, as with the nanothermite reactions, organic EMs react very quickly and therefore it is difficult to probe the intermediate steps of the reaction.

As previously mentioned, some systems like RDX have been around for over a century. These materials have had hundreds of articles dedicated to their reaction mechanisms, yet these mechanisms are still uncertain. For GEMs, new materials are rapidly being produced so there are only a very limited number of studies on specific materials and their decomposition properties. The amount of literature dedicated to these materials is far exceeded by that of traditional organic EMs. With many new materials it would be impossible to dedicate this much time to each. Even in in the most well-studied materials there exists uncertainty in reaction processes, and may signify the need for new techniques to approach this problem. New methods are required to improve upon previous experiments for better probing of the reactions of these, which is the goal of this research.

1.4. Ultra-Fast Reactions in Energetics

GEMs and thermites can be put into two different classes of energetic, organics (GEMs) and inorganics (thermites), which have significant chemical, physical, and mechanistic differences. Despite their differences both of these have the ability to participate in ultra-fast chemical reactions, which is necessary for a high rate of energy release. Ultra-fast reactions within EMs largely depend on the mixing of the fuel and oxidizer within the material, as mass transport effects can often be the rate limiting step in a chemical reaction. One major difference between GEMs and nanothermites is that

their fuel and oxidizers are mixed at different length scales that affect the speed of their reactions. Traditional organic explosives (TNT, RDX, HMX) and GEMs have a fuel and oxidizer mixed at the atomic level allowing for a very fast reaction rate as there are negligible mass transfer delays for diffusion of the fuel and the oxidizer. On the other hand, a thermite made up of an intimate mixture of metal and metal oxide nanoparticles still has a relatively large distance between the fuel and the oxidizer that restricts the speed of the reaction. The nanoparticles in traditional nanothermites can be tens to hundreds of nanometers. With a 100 nm aluminum particle as the fuel in a nanothermite system, part of the fuel is at least 50 nm from an oxidizer, compared to angstroms for organic EMs. Although the nanothermite reaction is slower than organic EMs it is still fast, but leaves obvious questions into how the nanothermite reaction can be sped up. These questions could potentially be answered if the reaction processes of nanothermites were more thoroughly understood.

1.5. Slow Heating vs. Rapid Heating

Many combustion and ignition processes are known to display high heating rates, so to mimic these processes high heating rate experiments should be used. While low heating rate experiments can be beneficial in determining the thermal stability of a system, and uncovering some mechanistic processes, high heating rate experiments are still needed to understand and verify the processes that occur during rapid combustion events. Reaction kinetics can vary greatly as a function of heating rate [16], but these changes are not fully understood, although it is typically assumed that kinetic variations at different heating rates are due to changes in the dominant chemical processes. There

are trends that support this concept including the increase of the observed nanothermite ignition temperature with an increase in heating rate [17, 18] while apparent activation energies tend to decrease [19, 20]. Nanoaluminum provides a good example of how burning times can change with heating rates as at moderate heating rates it has been shown to burn on the order of 1s [20], but at very high heating rates it burns on the order of 100µs [21]. Clearly there are significant differences in slow and rapid heating experiments, and since ultra-fast energetic reactions demonstrate rapid heating conditions, it is desirable to study these materials under a similar environment.

1.6. Experimental Needs

To study the initiation mechanism of an ultra-fast reaction such as that of the nanothermites and organic EMs, there are several key factors that are desired from an investigative instrument:

1. Species Identification:

   For probing the reactions of combustion events, it is desirable to have species identification capabilities for the reaction products. This will enable us to understand more about what reactions are occurring, and what is necessary for ignition of a given energetic material.

2. High Sampling Rate:

   The sampling rate of an instrument capable of species identification is the biggest concern, and the most difficult to overcome. If a combustion event occurs on the order of microseconds, an instrument that can sample on the microsecond timescale is needed. Most experiments that investigate the products of

combustion operate on long time scales that are only capable of capturing the final reaction products. Species identification at fast timescales is difficult because with a reduction in time scale there is a reduction the amount of material that is collected for analysis. For spectrometry purposes, this can often result in poor spectral resolution.

3. High Heating Rates With Known Temperatures

During combustion or ignition events, heating rates greater than 10^6 K/s can be obtained. Therefore, experimental heating rates that mimic those of an actual combustion event should be used. While some methods such as laser heating are effective in heating a sample very rapidly, it is not possible to simultaneously record the temperature of the sample during heating. Therefore, the temperature of initial reaction is still unknown. Knowing the ignition temperature of individual samples is necessary for characterization purposes, and can also be valuable when analyzing reaction mechanisms.

4. Probing of Initial Reactions /Elimination of Secondary Gas Phase Reactions

Investigation of initial and intermediate processes is a primary concern, and consideration must be given to the atmosphere in which the system operates. To accurately probe the initial and intermediate events, care must be taken to eliminate or reduce secondary reactions. Secondary reactions can occur either through the reaction of volatile products with the atmosphere, or through re-combination reactions between multiple products. With a proper experimental

setup, the first detected product species should be the first product species that are produced by the reaction. If secondary reactions occur, these reactions will make it difficult to determine what processes are related to the primary reaction.

Chapter 2: Temperature-Jump/Time-of-Flight Mass Spectrometry

2.1. System Introduction

A temperature–jump/time-of-flight mass spectrometer (T-Jump/TOFMS) [22] pictured in Figure 2.1, was developed with the goal of satisfying the above mentioned experimental needs, and Figure 2.2 shows the key features of the system.

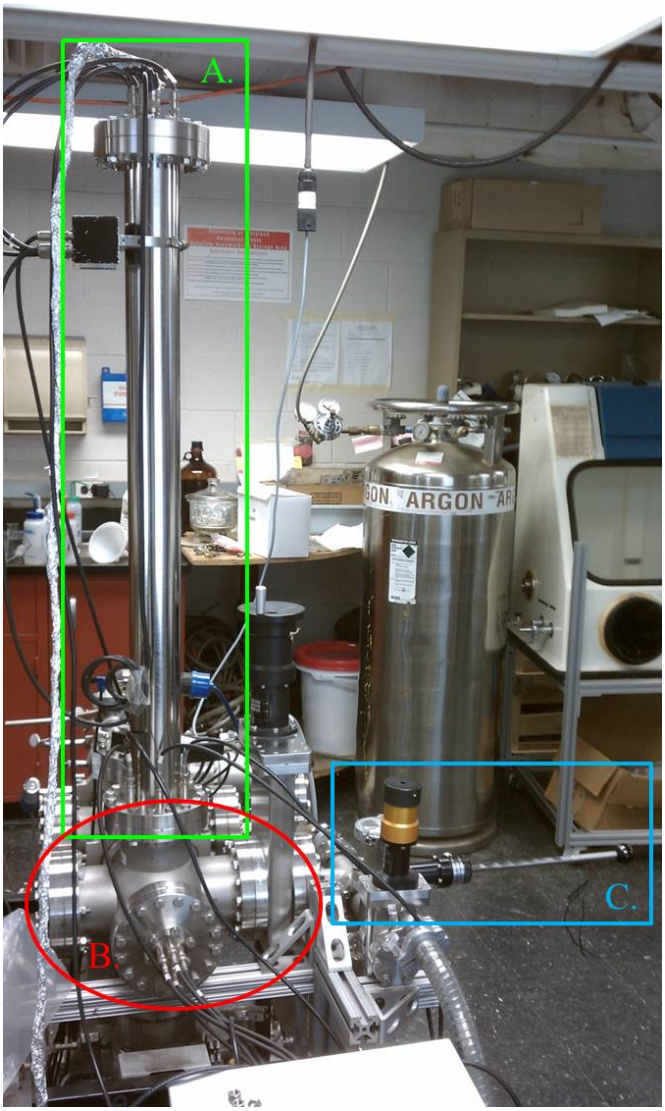

Figure 2.1: Image of T-Jump/TOFMS. A. Time-of-Flight tube. B. Ionization region (in vacuo) and electron gun. C. Sample insertion probe and gate valve.

The system is designed to rapidly heat energetic materials and simultaneously sample the reaction products at a fast time resolution. By using very small samples this system allows for the probing of the initial reaction events, and the reduction of secondary reactions that are sometimes associated with the use of large samples.

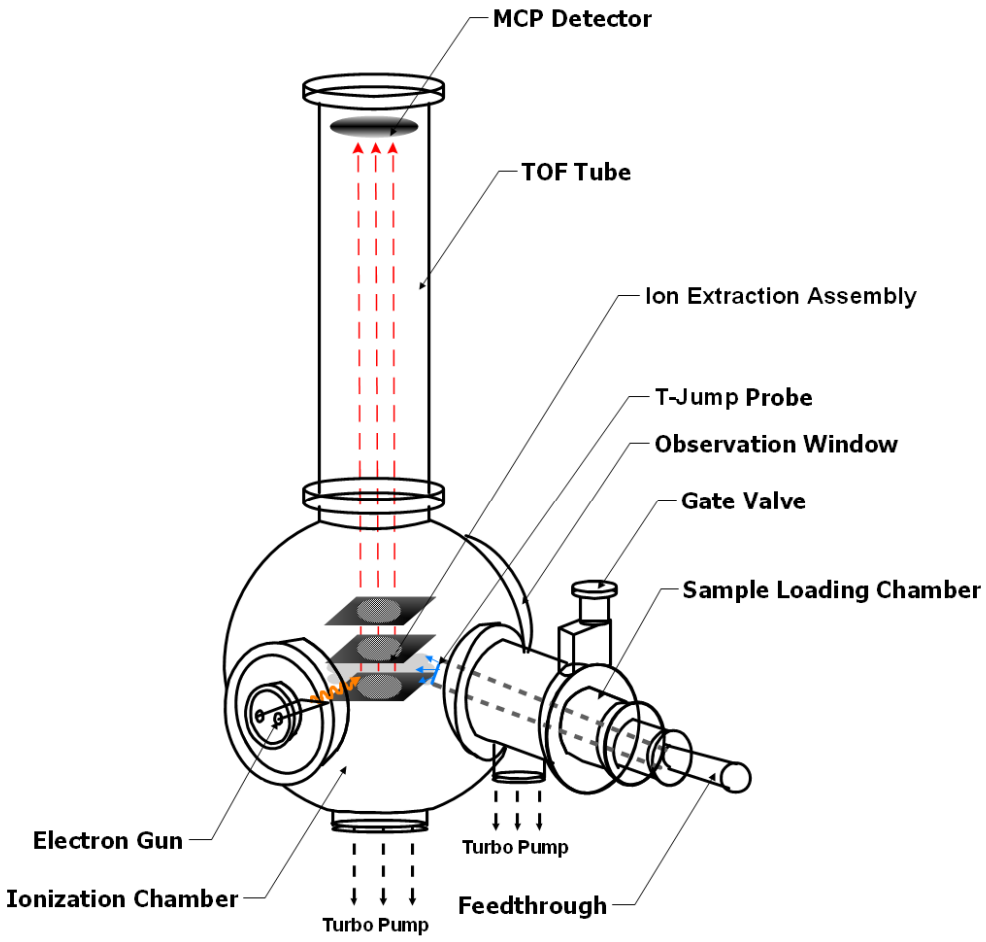

Figure 2.2: Schematic of primary components in the T-Jump/TOFMS setup [22].

The minimization of secondary reactions is further aided by heating of the samples under high vacuum. This eliminates the oxidizing environment of air, and the products have a large mean free path and quickly move away from the reaction zone. At atmospheric

pressure, when reaction products are formed, they can create a higher local pressure around the reaction zone and promote reaction of volatile products.

2.1.1. Rapid Heating

The essence of the temperature-jump system is a fine platinum filament with a ~76 µm diameter and 1-2 cm length, which acts as the heating surface for the sample material. The filament is resistively heated by a tunable current pulse that is output by an in-house built power supply. This power supply is capable of heating pulses in the range of 2-20 ms, and heating rates of nearly 10^6 K/s. The maximum temperature is close to that of the melting point of platinum at 2043 K.

2.1.2. Temperature Calculation

During the heating events the current and resistance are simultaneously monitored to determine the resistance change of the filament with increased temperature. The current is measured using a Tektronix AM 503 Current Probe Amplifier, and the voltage is recorded by a Lecroy LT344 digital oscilloscope. Due to the known thermal properties of platinum the change in resistance can then be related to the temperature of the filament using the Callendar-Van Dusen equation [23],

$$R_T = R_o[1 + AT + BT^2] \qquad (2.1)$$

In this equation, R_T is the resistance at a certain temperature (T), R_o is the resistance at 0 ^oC, and A and B are material dependent constants, with typical parameters for platinum being A = 3.985×10^{-3} $^oC^{-1}$ and B = -5.85×10^{-7} $^oC^{-2}$ [24].

There are several factors that can contribute error to the temperature measurement. The goal is to obtain the temperature of initial reaction of the sample, but this method

determines the temperature of the filament. Heat transfer calculations show that the temperature of the particles nearest to the filament follow the temperature of the filament within 5 K [25]. Therefore, the temperature of initial reaction should be similar to that of the filament. Other potential sources of error are due to the use of a new filament for each experimental run. This requires measuring of the filament, and soldering the wire to the electrical leads. These tasks could lead to variations in initial resistance and contact resistance, which are both factored into the temperature calculation.

There are also concerns with physical properties of certain materials such as nanothermites. At the bulk scale, ignition and burn rate are dependent on the packing density and stoichiometry. These experiments are performed with very small samples (1-200 μg), so these factors may have little bearing on the initial reaction. However, stoichiometry may be of concern since we are dealing with sparsely coated agglomerates of fuel and oxidizer particles. The local stoichiometry near the filament could change between experiments producing differences in ignition temperature. Despite these factors and the rapid heating rates that are used, ignition temperature errors are typically below ± 40 K.

2.1.3. Samples

Nanothermite samples were prepared by mixing aluminum nanoparticles with Bi_2O_3, CuO, or Fe_2O_3 particles to obtain a stoichiometric mixture,

$$2Al + Bi_2O_3 \rightarrow Al_2O_3 + 2Bi \quad (1)$$

$$2Al + 3CuO \rightarrow Al_2O_3 + 3Cu \quad (2)$$

$$2Al + Fe_2O_3 \rightarrow Al_2O_3 + 2Fe \quad (3)$$

where the Bi_2O_3 is from Sigma-Aldrich and has a primary particle size of ~100 nm and the aluminum is from Argonide with an average particle size of ~50 nm. Carbon/metal oxide samples were also stoichiometrically mixed assuming,

$$C + 2MO \rightarrow 3CO_2 + 2M \qquad (4)$$

with "regal 300" carbon black attained from Cabot Corp (MO = metal oxide, M = metal).

When calculating stoichiometry, an Al_2O_3 shell, which makes up 30% of the mass of the aluminum sample is taken into account as previously determined through thermogravimetric analysis. The samples are initially placed in a hexane solution and sonicated for ~20 min to ensure a fine mixing of materials. The materials studied are 5-amino-1H-tetrazole (5-AT), 5-amino-1-methyl-1*H*-tetrazolium dinitramide (MeHAT_DN), 1,5-diamino-4-methyl-1*H*-tetrazolium dinitramide (MeDAT_DN), 1,5-diamino-1*H*-tetrazolium nitrate (DAT_N), 1,5-diamino-4-methyl-1*H*-tetrazolium azide (MeDAT_N3), and 5-aminotetrazolium dinitramide (HAT_DN). 5-aminotetrazole was acquired from Sigma-Aldrich and all other samples are provided by T.M. Klapötke of Ludwig-Maximilians University in Munich, Germany. With the exception of 5-aminotetrazole, the synthesis of each material is documented elsewhere [15, 26-28]. Each sample is placed in either ethanol or methanol to aid in applying the sample to the wire and to maintain stability of the material.

2.1.4. Sample Coating

The sample solutions are placed in a dropper and then manually applied to the platinum filament. The drop of sample is repeatedly contacted with the filament, typically until a small amount of sample is noticeable on the wire. With this method it is

difficult to ensure uniform sample properties such as mass, packing density, and sample thickness. However, it is a process that allows for relatively rapid repetition, and despite the non-uniformities, still produces repeatable results. Calculations predict that for organic samples, the mass of material varies between 1-10 µg, and for nanothermites between 1-200 µg. Figure 2.3 shows an SEM image of a filament sparsely coated with Al/CuO nanothermite.

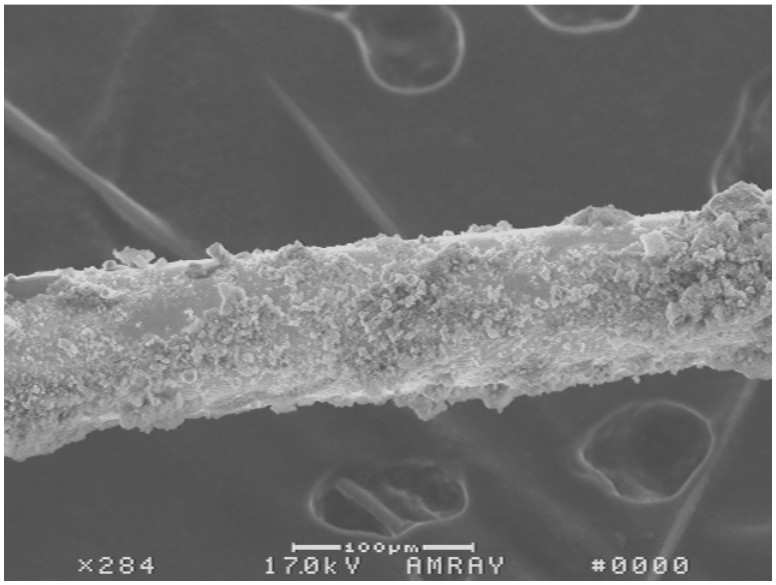

Figure 2.3: A SEM image of Al/CuO sparsely coated onto a platinum filament.

2.1.5. Sample Loading and Testing

The platinum filament is connected to an electrical vacuum feed-through that allows for insertion into the high vacuum chamber of the TOFMS by way of a gate valve. Insertion of the filament into the vacuum region without breaking the high vacuum allows for a reasonable repeat rate for the experiment. The TOFMS is a customized single particle mass spectrometer [20], and was fitted with an electron impact ionization source set to 70 eV for a "soft" ionization technique compared to the previous laser

ablation ionization method. The essence of this system is that the sample is inserted into the vacuum chamber of the TOFMS within close proximity to the ionization region of the MS and rapidly heated. Therefore, once the reaction occurs, the product species quickly travel through the vacuum to the sampling region and through the TOF tube (~10 µs). A schematic for the operation of the T-Jump/TOFMS system is given in Figure 2.4.

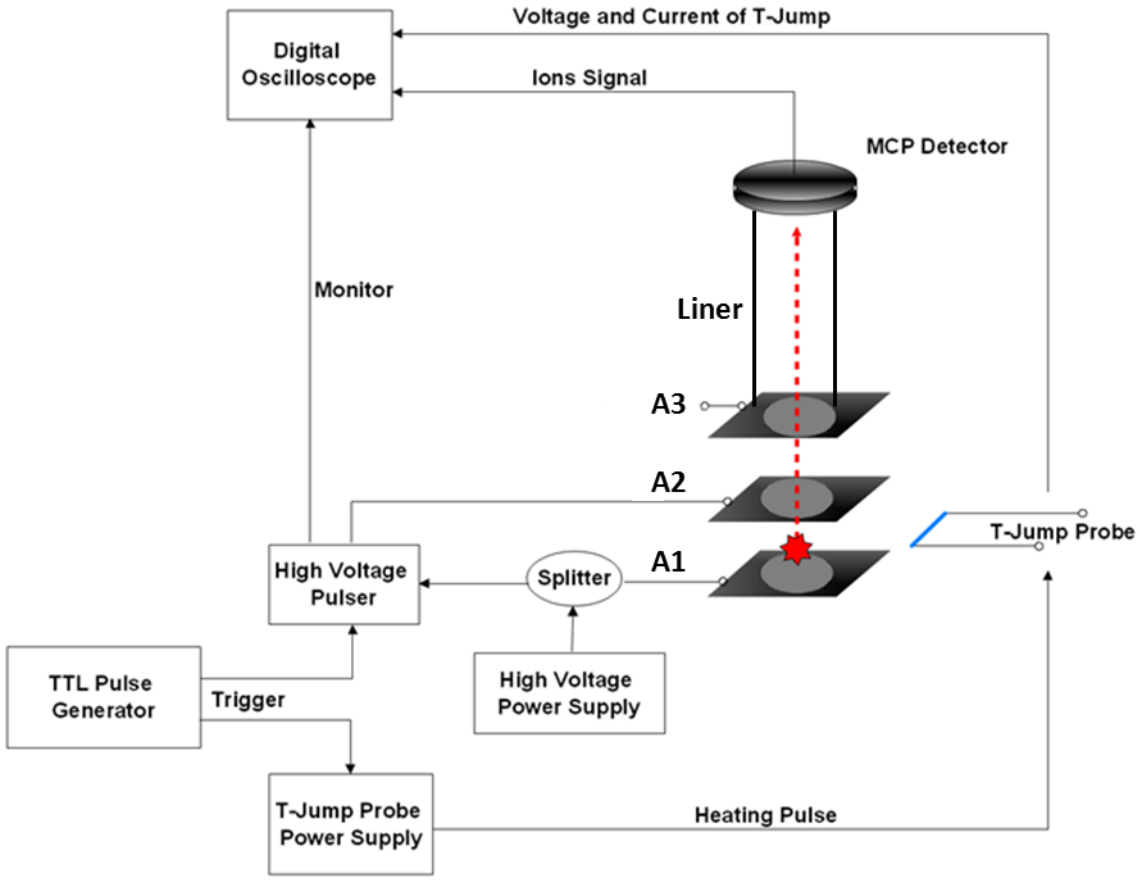

Figure 2.4: Schematic of the electrical connections for the high voltage extraction plates and heating pulse [22].

The sampling of the MS is performed at 10,000 Hz giving a 100 µs time resolution between each full spectrum, which ranges from m/z 0 to m/z ~400. A function generator triggers the heating event as well as the pulsing of the electric field in the ionization

region of the mass spectrometer. Pulsing of the extraction plate implements a gradient in the electric field that accelerates the ions through the TOF tube to the micro-channel plate (MCP) detector. There are several experiment variations that are possible with this system including the detection of ions formed inherently in the reaction, or self-ionization studies. The applied voltages for the various experimental setups are given in Table 2.1. In a typical T-Jump/TOFMS experiment the electron gun impaction is the primary method of ionizing product species. For self-ionization experiments, the main modification is the turning off of the electron gun. In this case, any ions that are detected are a direct result of the thermite reaction.

Experiment / Extraction Plates	Positive Ion Species Detection	Total Ion Detection (positive)	Total Ion Detection (negative)	Negative Ion Species Detection Proposed (1)	Negative Ion Species Detection Proposed (2)
Filament Placement	Edge	Center	Center	Edge	Edge
A1	Ground	Ground	-200	-1500	Pulsed (Ground to -200V)
A2	Pulsed (Ground to -200V)	-200V	Ground	Pulsed (-1500 to -1300V)	Ground
A3/Liner	-1500V	-1500V	-1300V	Ground	Ground

Table 2.1: Voltage specifications and filament position for various experimental setups.

2.1.6. Initial System Implementation

This system was designed to study the reaction events in both organic EMs and nanothermites. Initial testing of organic materials was successful with few setbacks, but testing of nanothermites was much more difficult. The issue that arose for nanothermite testing was the formation of ionic species during the initiation event (this was confirmed and characterized in a later study [29] and will be discussed in Chapter 3). In the initial system design, positive voltages were used on the extraction plates of the ionization region (A1 = +1500V, A2 = +1300V, A3/liner = ground), and it was the presence of the positive voltages, combined with the formation of a large amount of negatively charged ionic species during the nanothermite reaction that caused failure of the time-of-flight mass spectrometer. Figure 2.5 is a picture of the ionization region of the mass spectrometer taken during nanothermite combustion. The filament is located horizontally in the center of the image, in between the two extraction plates. The image was taken with a standard digital camera using a shutter time much longer than that of the heating pulse so that the entire reaction event could be captured. We suspect that the blue regions represent arcing as they are not present during instances without arcing. Due to the large amount of negatively charged species that are formed during the nanothermite ignition, adjustments were made to reduce the field gradient near the filament, and also to use only negative voltages (negative species are repelled). The current setup, that is successful for nanothermite testing is the ‘positive ion species detection’ configuration in Table 2.1.

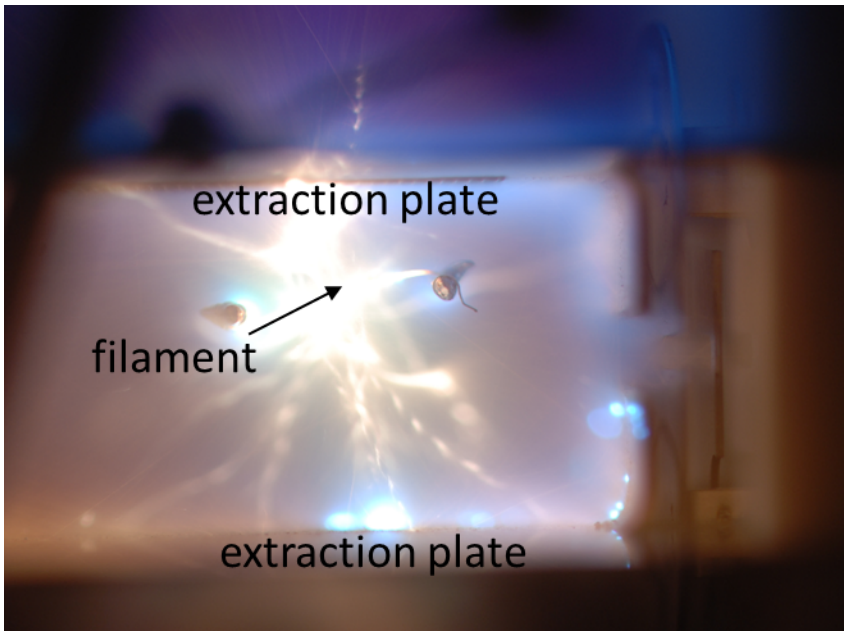

Figure 2.5: This image was captured using a shutter time much longer than that of the heating event to capture the entire event. Blue colored regions, likely represent arcing within the system.

To troubleshoot the arcing issue, SIMION 8.0 [30] was used to model the electric field and trajectory of ions in the mass spectrometer. Figure 2.6 shows a sample positive ion trajectory through the extraction region of the mass spectrometer for a high voltage configuration. This figure shows the changes in the electric field with and without the platinum filament. The modeled plate configuration is not listed in Table 2.1, but is essentially that of 'Negative Ion Species Detection Proposed (1)' but with reversed polarity. The simulation assumes that the ions are formed in the middle of the extraction region as this is the plane where the electron gun enters the extraction region. With such a large field gradient between the 'T-Jump Probe' (filament) and the extraction plates, there is a large flux of ions to the sample filament. This may have been part of the reason for the lack of success of the positively charged high voltage extraction region. A detailed description of the use of SIMION 8.0 is given in the appendix.

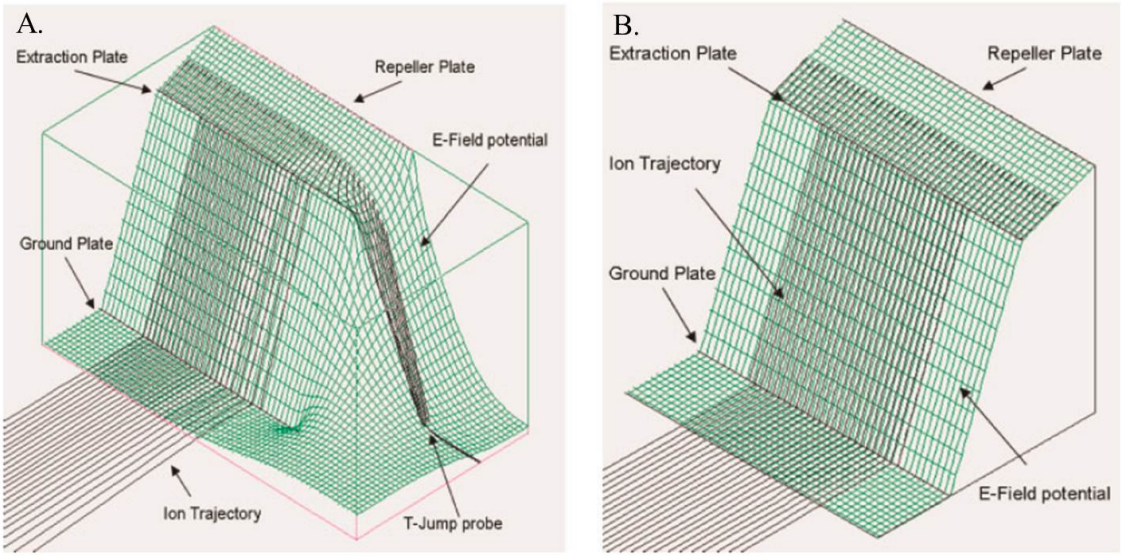

Figure 2.6: Ion trajectory model for the extraction region of the mass spectrometer using SIMION [22]. A. With the filament inserted near to the extraction plates of the spectrometer. B. Without the sample filament ("T-Jump probe").

2.2. Experimental Goals

The main objective of these studies is to gain a further understanding of the reaction mechanisms of both nanothermites and organic EMs. This knowledge could aid the advancement and tuning of energetic materials to create optimal conditions for their specific applications. For nanothermites it is necessary to study the role of both aluminum and the metal oxide during initiation and the overall reaction. By examining the effects of rapid heating on the nanothermite, as well as the neat metal oxide and nanoaluminum powders it may be possible to draw some conclusions about the nanothermite dependence on each of these components. The different properties of each metal oxide should effect the nanothermite reaction in some fashion, and this study may clear up which of these properties are most influential. Initiation of the nanothermite

reaction is difficult to study due to the speed of these reactions, but with the use of the high sampling rate, a clear set of reaction steps may be obtainable.

In organic EM reactions slight variations in molecular structure may significantly change the breakdown mechanism. The studying of the breakdown mechanisms of several similar materials, particularly tetrazole containing energetic salts, may allow for identification of the tetrazole ring breakdown mechanism under high heating rates. This could also reveal whether slight changes in molecular structure affect the final reactions products or the reaction mechanism. Furthermore, the dependence of decomposition on different functional groups or anion species and how they influence the reaction properties of the material can also be probed.

It is expected that there are some differences in reaction time or decomposition temperature for each material that can be observed with our system. With a system capable of high heating rates like our T-Jump/TOFMS, it is also interesting to examine the activation energies of materials under these conditions. Different mechanistic processes will likely be at play under high heating rates that could result in a change in activation energy. Our system works at heating rates that are orders of magnitude greater than traditional DSC experiments commonly used to detect activation energies, so it is unclear how these conditions will impact the reaction. Complementary high heating rate studies are used in conjunction with the T-Jump/TOFMS, including a DSC study to probe the activation energy.

Chapter 3: Review of T-Jump/TOFMS Nanothermite Ignition

The first issue addressed with the T-Jump/TOFMS concerning the nanothermite reaction was the dependence of the reaction on oxygen release. This study showed the correlation between the ignition of several nanothermites and the release of gaseous O_2 from the metal oxide, and further demonstrated variations in ignition temperature with different metal oxides. This was the first known study to incorporate a rapid heating and rapid product species detection process for in situ investigation of nanothermite reactions. To better understand the detailed aspects of a few systems in Chapters 4 and 5, we must first address our initial findings on the nanothermite reaction. This will shed light on the order of events throughout this study, and also bring forth key information that will contribute to the final conclusions.

3.1. Thermite Dependence on Oxygen Release

3.1.1. Oxygen Release Review

In nanothermites, mixing of the fuel and oxidizer at the nanoscale greatly reduces diffusion lengths and increases surface area allowing for a much more rapid reaction than their microscale counterparts. Nanothermites have demonstrated burn rates of several orders of magnitude higher than microscale thermites, and in some cases are approaching the reaction rates of organic energetics [6-8, 31, 32]. However, unlike organic energetics, nanothermites can be easily tuned through variations in oxidizer, packing density, or stoichiometry. Nanothermites have not been studied as extensively as traditional organic EMs, and limited diagnostic tools have been developed to study the unique features of

this class of materials. In situ investigation of nanothermites is a difficult task due to the intense, ultra-fast reactions that are present during ignition. Under slower heating conditions, slower thermite reactions have been observed and characterized to gain a better understanding of the mechanistic processes. However, a typical nanothermite reaction is very fast, and therefore these reactions may be controlled by different mechanisms. For aluminum thermites with CuO [18], Fe_2O_3 [33], and MoO_3 [17] multiple reaction steps have been observed, but as these were seen at slow heating rates they may not translate to the rapid heating conditions of the thermite reaction.

To understand the processes for typical nanothermite reactions, rapid heating rates must be used and a number of studies have been performed to examine combustion properties under such conditions. A laser induced initiation technique, which can be easily used with other diagnostic techniques, has been used to study thermite combustion processes [34, 35]. The nanoscale aluminum and molybdenum trioxide composite (Al/MoO_3) was studied using CO_2 laser ignition with a high speed camera system, and size dependent information about ignition behavior and burn rate was obtained [35]. Time-resolved spectroscopy was employed by Dlott and co-workers [36] to investigate laser initiated an Al/nitrocellulose mixture. The optical emission spectra were also used to investigate the rate and mechanism in the energy release processes. Moore *et al*. [37] used time resolved spectral emission technique to study the combustion of Al/MoO_3, where AlO was observed as the main reaction product. More recently, a fast synchrotron x-ray micro-diffraction technique was used to characterize the self-propagating exothermic reaction of Al/Ni multilayers, time-resolved measurement was achieved with temporal resolution of 55 µs and spatial resolution of 60 µm [38]. A hot filament heating

technique is also widely used in studying reaction kinetics under high heating rates. In particular, temperature-jump (T-Jump)/FTIR has been developed to study reaction kinetics of condensed-phase propellants, and many organic energetic materials have been studied using this technique [16, 39, 40]. Recently, this approach was applied for kinetic analysis of metal powders. Al/MoO_3 and Al/CuO nanocomposites were investigated using this technique and their kinetic reaction model was constructed from experimental data [17, 18]. Despite the use of a variety of experimental techniques, none of these systems combined rapid heating with a rapid sampling technique that is capable of in situ probing of the nanothermite reaction. This leaves a high degree of uncertainty for the nature of the initial and intermediate reaction processes in nanothermites.

Our T-Jump/TOFMS system is designed to probe the initial processes in the nanothermite reaction. The direct insertion of the sample into the vacuum region of the TOFMS allows for the in situ sampling of the reaction. It was initially used to study the aluminum/copper oxide (Al/CuO) and aluminum/iron oxide (Al/Fe_2O_3) reactions. The effect of high heating rates on the neat oxide powders is also studied. The spectra from both the thermite and oxide heating can be used to draw conclusions about the role of oxygen release on the initiation of nanothermite reactions.

3.1.2. Oxygen Release and the Nanothermite Reaction

The goal of this work is to gain a better understanding on the initiation of nanothermites, especially the mechanism of oxidation. To begin studying this process the T-Jump/TOFMS is used to investigate the nanothermites, but it is also necessary to study the neat oxide and aluminum powders under high heating rates. A typical time-resolved

spectrum for Al/CuO is shown in Figure 3.1, but to get a more detailed view the individual spectra for Al/CuO, Al/Fe_2O_3, CuO, Fe_2O_3, and Al are shown in Figure 3.2. Figure 3.2(a) is the background of our spectrometer, which shows a peak at m/z 18 for H_2O, as well as very small peaks at m/z 28 and 32 for N_2 and O_2 respectively.

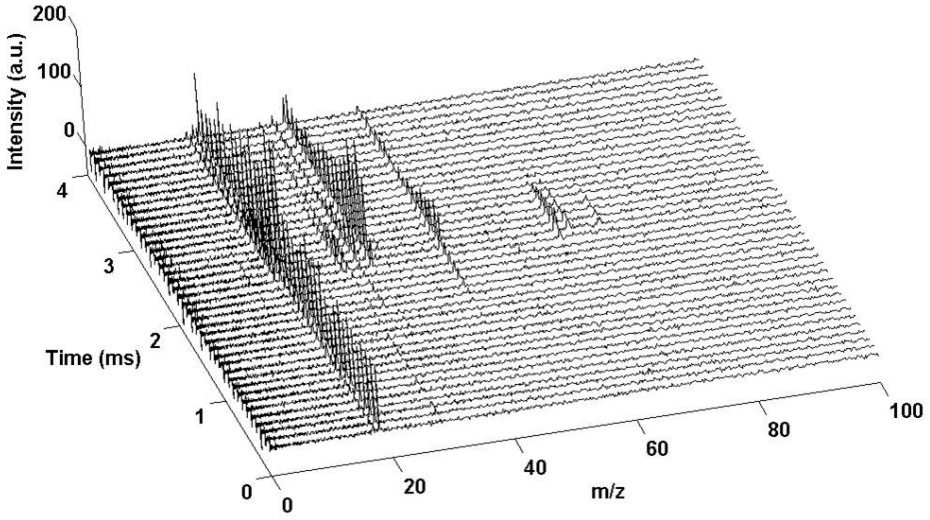

Figure 3.1: Time-resolved spectrum of Al-CuO nanothermite during a T-Jump/TOFMS experiment [41].

The neat oxide powders in Figures 3.2(e) and 3.2(f) typically have several product species in common: O_2, CO, and CO_2. The O_2 likely comes from decomposition of CuO to Cu_2O and O_2 or from Fe_2O_3 decomposing to Fe_3O_4 and O_2, while the CO and CO_2 are likely the product of a low temperature reaction between residual carbon (likely from hexane solvent) and the metal oxide. The production of CO_2 is addressed in greater depth in Chapter 5. There are some other products observed for each, including Al, Al_2O, and the respective metal of the metal oxide, Cu or Fe depending on the nanothermite. Looking at the spectrum for neat Fe_2O_3 and its nanothermite, a significant difference is observed in the O_2 production between the two. There is a small peak produced from the

neat oxide, but in the nanothermite there is virtually no O_2 peak. This suggests that the O_2 is completely consumed in the nanothermite reaction causing the peak reduction. In the Al/CuO reaction, there is likely an abundance of O_2 produced by CuO, therefore during the reaction the added heat accelerates the release of O_2 so that the detected O_2 concentration is even higher than that of the neat CuO.

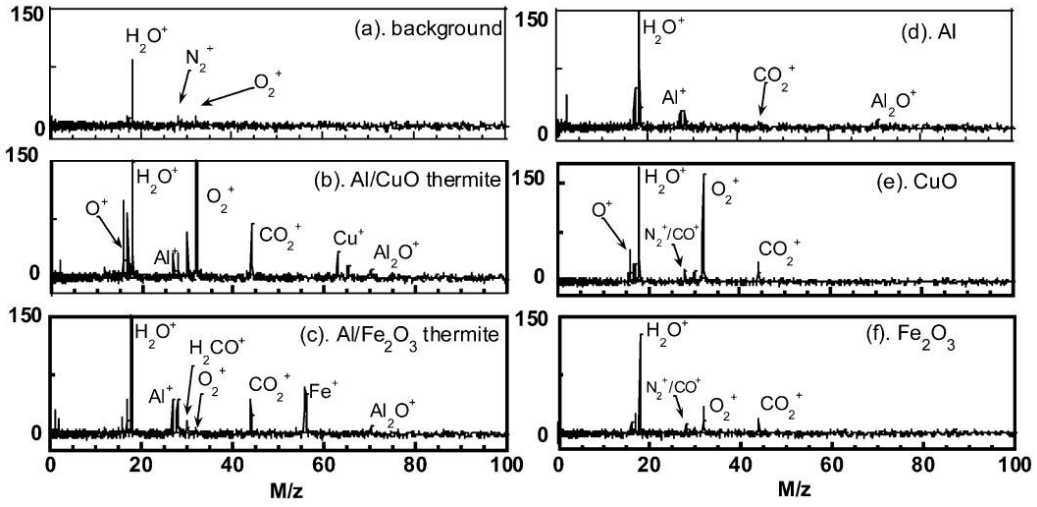

Figure 3.2: Individual spectra of nanothermites and neat nanopowders during T-Jump/TOFMS experiments [41].

The time-resolved spectrum for each sample can be used to study the evolution of each product species to better understand the order of events in the nanothermite reaction. Figure 3.3 shows the detected concentration of individual product species as a function of time for typical nanothermite runs. PMT traces from wire heating experiments in air are also shown in these plots to give a correlation between wire experiments in vacuum and at atmospheric pressure. These traces verify that the TOFMS measurements are a good determination of the burning time of nanothermites in the wire heating experiments. From this figure the order of the product species within the reaction are observed.

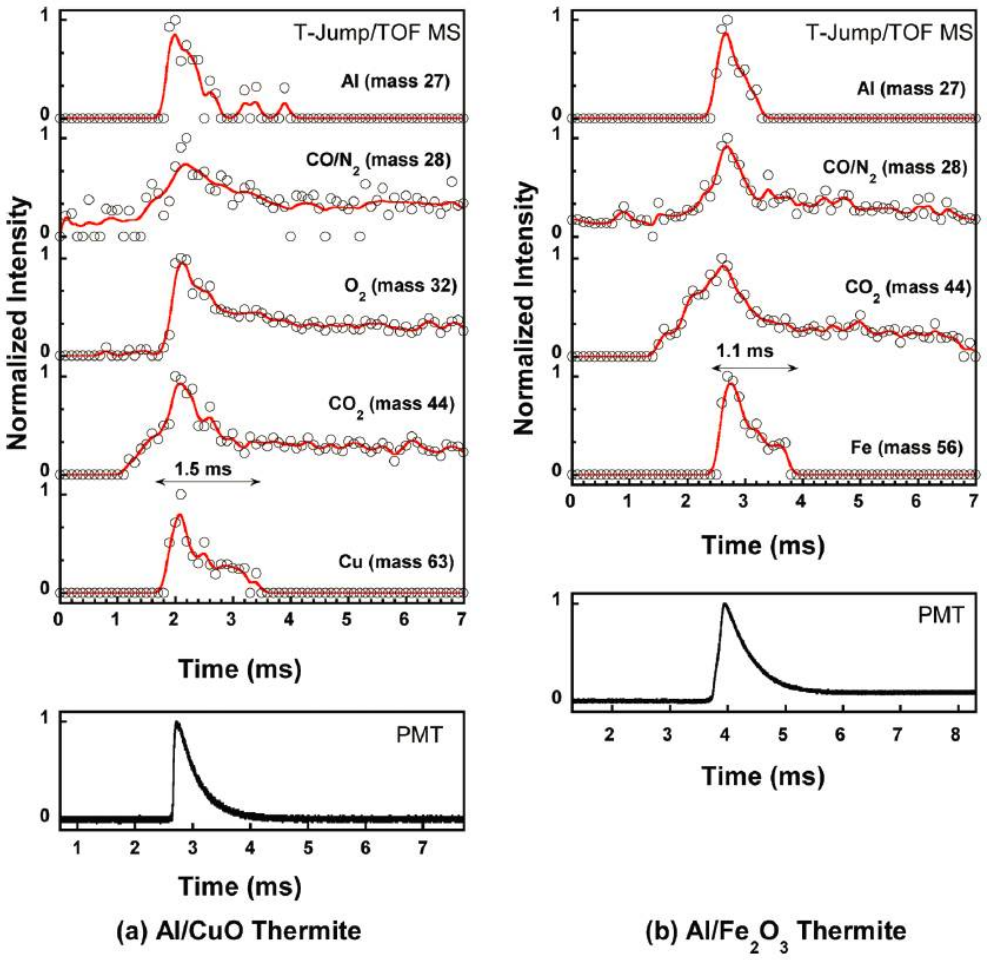

Figure 3.3: Detected species concentration as a function of time for individual product species from the T-Jump/TOFMS [41].

The first peaks observed are the CO and CO_2 peaks, which again can be attributed to a low temperature reaction between carbon and the metal oxides. After this process comes the appearance of O_2, Al and Cu or Fe, all within close proximity to each other. Occasionally the appearance of O_2 occurs ~100 µs earlier than the rest of these species, so it is expected that the oxide decomposition to produce gaseous O_2 precedes the ignition. At this point it is assumed that this gas phase O_2 is now readily available for oxidation of aluminum through one of the mechanisms in Chapter 1.2.1.

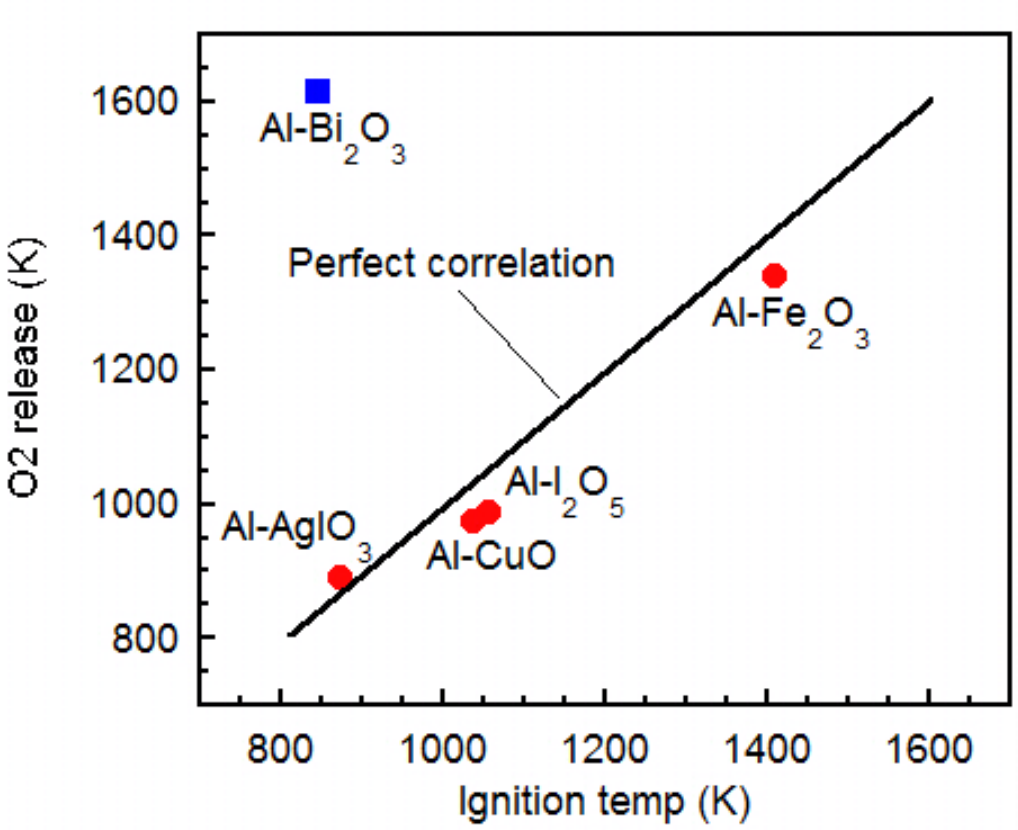

Figure 3.4: O_2 release temperature vs. the ignition temperature for various nanothermites.

Furthermore, these nanothermites will ignite at different temperatures with the varying oxidizers. To look further into the idea that gas phase O_2 release plays a large part in the nanothermite ignition, the temperature of gaseous oxygen release from a neat oxide powder is plotted vs. the ignition temperature of the respective nanothermite in Figure 3.4. The temperature for both the O_2 release and nanothermite ignition is determined from the onset of the product species. This figure shows that for several nanothermites, the ignition appears to strongly depend on the decomposition of the oxide. In fact for four of the five nanothermites shown here, the ignition point is close to the same point that the oxide decomposes to release gaseous O_2. This suggests that a gas

phase oxidizer is necessary for the rapid nanothermite reaction. However, results also showed that there was at least one thermite that did not adhere to this trend, Al/Bi_2O_3. This composite is the subject of Chapter 4, but it raises the question of whether the correlation of O_2 production and ignition is coincidental, or a necessary reaction step.

3.2. Ionization Experiments

Initial testing of nanothermites with our T-Jump/TOFMS produced many complications due to the presence of both high voltage plates in the TOFMS, and a very intense nanothermite reaction that produced a large amount of ionic species. Under the initial conditions the nanothermite reaction would shut down the mass spectrometer, and prompted a redesign of the high voltage system. Furthermore, these events prompted the characterization of ion production to better understand this phenomena and its relation to the overall nanothermite reaction.

3.2.1. Ionization During Combustion

The formation of ionic species has previously been observed in both organic and inorganic EMs under a variety of experimental conditions [42, 43]. For the combustion of nanothermites this could have significant mechanistic importance as ions are thought to have a large role in the diffusion of reactants through the Al_2O_3 shell of aluminum particles [13, 44, 45]. Several experimental works have noted the formation of an electric field during the combustion of metal containing systems. This has been demonstrated through the combustion of single metal particles [46-48], metal powders [49, 50], and also a variety of composite systems [51, 52]. The electric field formation in these systems may be due to the formation of an oxide layer, and a variance in diffusion

velocities of charged species across this layer [46, 51]. Simulations have supported this by showing that the alumina shell on an aluminum nanoparticle has a strong inherent electric field, and that this field aids the diffusion of aluminum ions outward through the Al_2O_3 shell [44]. It has also been shown that combustion events can be significantly affected by the application of an electric field [53-55]. Work by Martirosyan *et al.* [46] also showed that combustion of a single metal particle produced in electrical pulse that occurred very quickly compared to the to the total combustion time. Figure 3.5 shows an example from Martirosyan of the detected voltage from combustion of an iron particle in comparison with the total combustion.

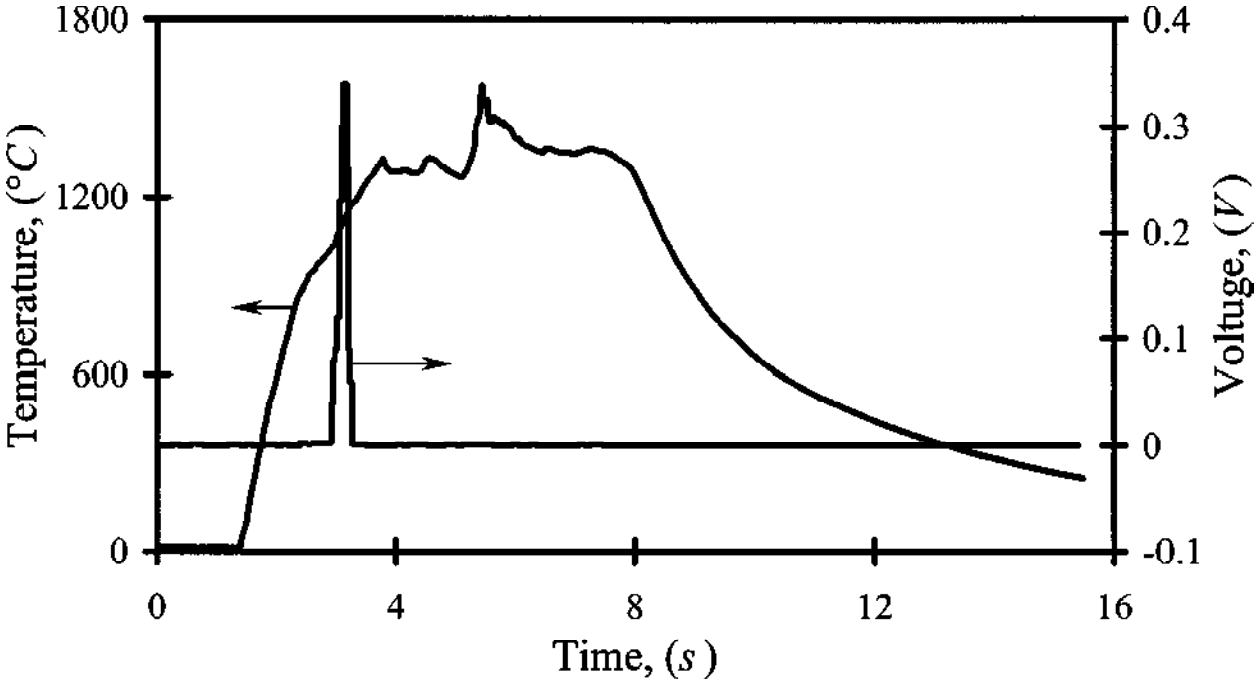

Figure 3.5: A plot of the temperature during the combustion of an iron particle with production of a sharp electrical pulse ~1 second after initiation [46].

From the above, it is difficult to conclude the role of ionized species within the nanothermite reaction, but evidence suggests that ions can enhance the diffusion within the nanothermite system. However, limited studies have noted the formation of ionic

species within a nanothermite system. Electric field formation has been noted for Al/Bi_2O_3 combustion [52], but aside from this work few others have noted ionization.

With the use of the T-Jump/TOFMS we attempt to characterize the ionization events during the nanothermite reaction. As noted, these events initially provided many difficulties in analyzing nanothermites, but with several adaptations we were able to capture the reaction products of nanothermites, and now can address the production of ions. Since the TOFMS system is designed to sample ionic species, we can test nanothermite samples without the presence of an outside ionization source (which is typically used), to probe the production of ions. Through variation of the voltages in the TOFMS system, it was also possible to analyze the positive and negative ionic species. The tests were also recorded with a high speed camera so that the ion pulse could be related to the overall combustion event. The voltage settings for the various aspects of these experiments are given in section 2.1.

3.2.2. Ionization During Nanothermite Reactions

We first examine where the ion pulses occur in relation to the entire nanothermite combustion event. Each of these tests was performed without the presence of an external ionization source so that any ions are a direct result of the nanothermite reaction. Four different samples were tested; Al/CuO, Al/Fe_2O_3, Al/WO_3, and Al/Bi_2O_3 and Figure 3.6 shows sample positive ion pulses for each of these systems. For each sample in Figure 3.6 the positive ion pulse is on the top part of the image, the optical trace is on the bottom, and a zoomed-in image of the ion pulse is given in the top right corner.

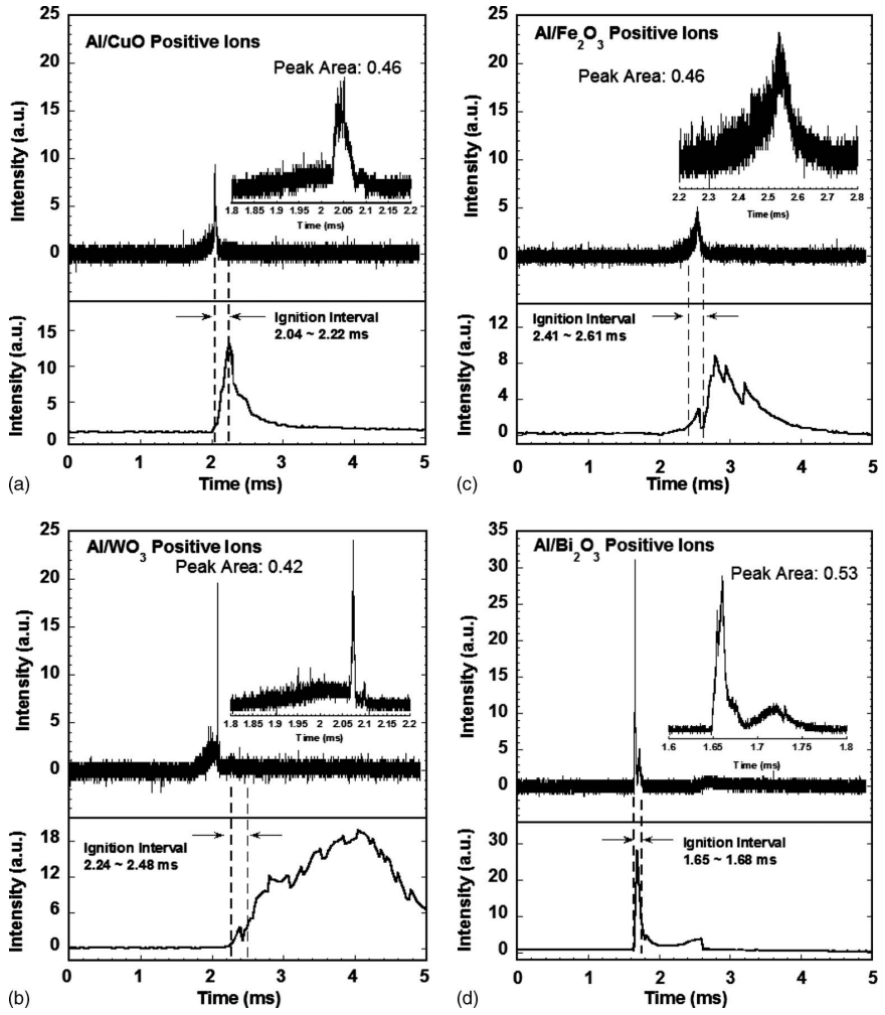

Figure 3.6: TOP: Detected positive ion signal for resepctive nanothermites, BOTTOM: optical signal taken during combustion [29].

For each ion peak the area under the peak was also determined to get an idea of the total amount positive ions produced. The term 'ignition interval' is also defined as the amount of time it takes for the nanothermite reaction to completely propagate down the wire, and is labeled in Figure 3.6. During typical nanothermite heating, the combustion starts at the ends of the filament and propagates to the center; the time it takes to do this is the 'ignition interval'.

Initial comparison of the ion pulse and the optical output suggests that the ion pulse only occurs in a small window of the combustion event. This is similar to what was observed by Martirosyan [46] for the combustion of single metal particles. In Figure 3.6a we see that the positive ion pulse for Al/CuO consists of a sharp ion peak that follows a relatively broad, less intense peak. The overall time for this event is ~300 µs, but the short peak is less than 100 µs, and the total time of the combustion event is ~ 1 ms. Further comparison of Figures 3.6a-d shows that Al/WO_3 has the sharpest ion pulse at ~20 µs, but has the longest burn time. Al/Bi_2O_3 has the most ionic species, but compared to the rest it is not significantly higher. However, the short duration of the main ionic peak for Al/Bi_2O_3 combined with the amount of ions produced give it the highest rate of ionization of the group. This also corresponds to a very rapid reaction as the bulk of the combustion is over after the ignition interval. Through comparison of the ion duration and the amount of positive ions produced, the ranking for the rates of positive ion production are Al/Bi_2O_3 > Al/WO_3 > Al/CuO > Al/Fe_2O_3. From this data there is not a conclusive correlation between the reaction rate, or ignition interval and the rate of ionization.

When the positive ion pulse occurs, the ion peak is slightly delayed (10-20 µs) due to the time-of-flight from the extraction region to the MCP detector. This is a small delay, and therefore was neglected, but if included would shift the ion peak to earlier in the event. In Figure 3.6a, the Al/CuO system ion signal starts slightly before the combustion event, and the main ionic peak is just after the start of combustion. This suggests that the formation of positive species in the nanothermite may play a role in ignition. Figures 3.6c and 3.6d show similar trends as the ionic peak coincides with

ignition, but do not appear to start before ignition as Figure 3.6a. For the Al/WO_3 combustion in Figure 3.6b it is apparent that the positive ions are released well before ignition. For this material the ion production could be a pre-cursor to ignition.

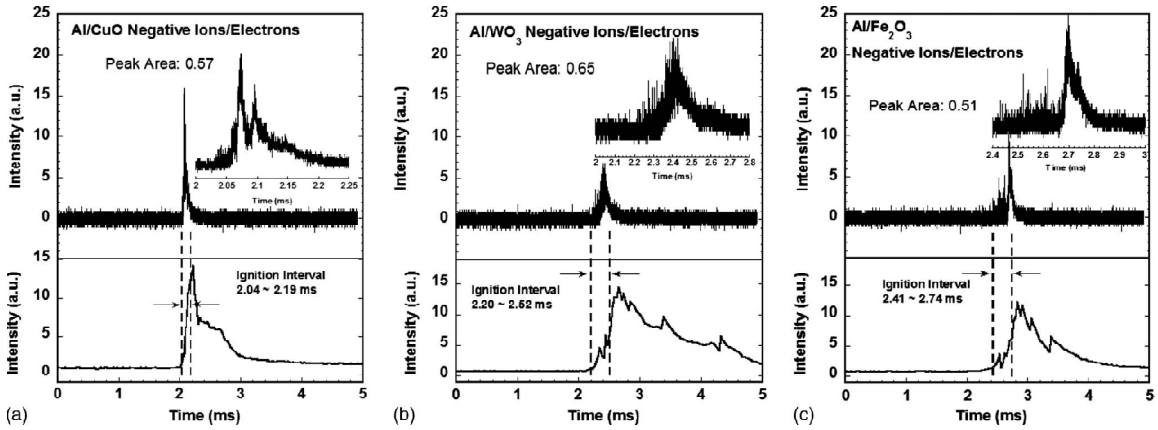

Figure 3.7: TOP: negative ion detection for respective nanothermites during combustion in T-Jump/TOFMS, BOTTOM: optical signal [29].

The negative ions were also probed in a similar fashion. The negative species trace with respect to the total combustion event is shown in Figure 3.7a-c for Al/CuO, Al/WO_3 and Al/Fe_2O_3. The negative pulse for Al/Bi_2O_3 was unattainable due arcing and subsequent shut down of the TOFMS due to the intensity of the pulse for this system. The duration of the negative species pulse is similar to that observed for the positive species, and also appears early in the combustion. However, unlike the positive species, negatively charged species are not observed before the ignition interval, but rather during the ignition interval. This may suggest two different ionization events for the positive and negative species. The positive ions are produced before the negative ions, and may at times occur before ignition. While both species appear to have a role in ignition, it

may be two different steps as the positive ions earlier. From Figures 3.7a-c, the amount of negative species that are produced is slightly greater than that of the respective positive ions for each system. If we further consider that the heating filament has a positive voltage, we can assume that the gap between positive and negative species is even larger as the negative species may be attracted back to the filament after formation. This could be similar to the effect seen in Figure 2.6. Although the voltage setups are different for this experiment, the negative ions may be drawn to the filament in the same fashion. We expect that the higher amount of negative species is due to the added presence of electrons. For the negative species, the ranking of production rate is Al/CuO > Al/Fe_2O_3 > Al/WO_3.

3.2.3. Ionic Species Identification

To better understand the role that ionic species are playing within the reaction it is necessary to determine their composition. In the above ion detection experiments the extraction plates of the mass spectrometer were not pulsed as in typical operation, but were left at a constant voltage. To identify the ionic species we ran the TOFMS in typical fashion, but again without the presence of the electron gun as an external ionization source.

Figure 3.8 shows a sample spectrum for the positive ion formation for Al/CuO. The observed species are m/z 23 (Na), 27 (Al), 39 (K), and a small peak at m/z 63 (Cu). The positive species were also identified for Al/WO_3 and Al/Bi_2O_3 and showed similar species of Na, K, Al.

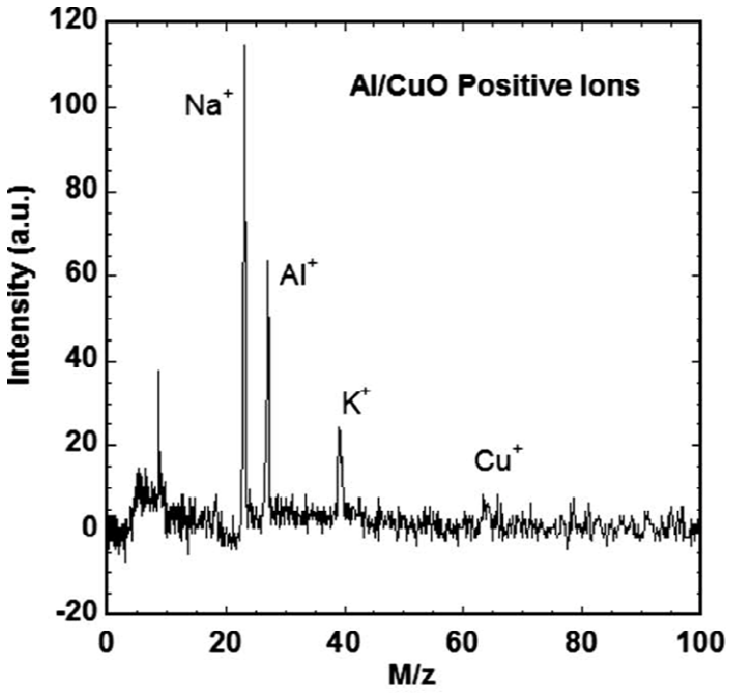

Figure 3.8: Species identification of ion emission during Al/CuO reaction [29].

The Al/WO_3 did not produce a noticeable tungsten ion, but Al/Bi_2O_3 showed a large bismuth peak. This is expected as Bi is highly electronegative and vaporizes at a relatively low temperature compared to reaction products of the other thermite systems. Al/Fe_2O_3 had the weakest positive ion peak, and no significant signal was obtained in the species identification experiments. It is interesting that the main ionic peak is that of sodium, a minor artifact within the thermite system. Sodium likely does not participate in the chemical reaction in nanothermites, but its charge may help in the diffusion of reactant species. The presence of positive aluminum ions supports the idea that diffusion of reactant ions may be aided by the presence of an electric field in the Al_2O_3. Detection of negative ion species was unsuccessful, as arcing was typically observed. Suggestions on how to effectively detect the negative species are given in section 8.2.1.

Chapter 4: Initiation and Reaction in Al/Bi_2O_3 Nanothermites: Evidence for the Predominance of Condensed Phase Chemistry

In an effort to confirm the dependence of the nanothermite reaction on the gaseous O_2 release by the metal oxide, similar studies were performed as those for Al/CuO and Al/Fe_2O_3, but for various other nanothermites. The intense ionic peaks observed for Al/Bi_2O_3 in the self-ionization study suggest that this system may have some unique properties, and therefore it was used for the oxygen release study. However, Al/Bi_2O_3 proved to be a unique material, and revealed different reaction characteristics than the previously studied nanothermites.

Chapter 4 Overview

In this study we explore the reaction between Al and Bi_2O_3 nanoparticles under high heating rate conditions with Temperature-Jump/Time of Flight Mass Spectrometry (T-Jump/TOFMS), high speed imaging, and rapid sample heating within a scanning electron microscope (SEM). High speed imaging indicates that the bismuth based nanothermite reaction is about twice as fast as a comparable copper oxide system, contrary to previous work with burn tubes and open burn trays. The initiation of the bismuth oxide nanothermite reaction occurs at a much lower temperature than the point where oxygen is released from the neat bismuth oxide powder. Thus, without the presence of a gas phase oxidizer, we conclude that a condensed phase initiation mechanism must be at play in the bismuth oxide nanothermite. C/Bi_2O_3 heating experiments were used for a mechanistic comparison between two different fuel types since the carbon represents a non-volatile fuel in contrast to the aluminum. This

formulation showed a similar condensed phase initiation as was seen with the aluminum nanothermite. Bi_2O_3 is known to possess unique ion transport properties, which combined with the presence of oxygen and aluminum ions within the nanothermite system may play a significant role in the speed of the nanothermite reaction.

4.1. Introduction

Thermite reactions are gaining increased interest in the field of energetic materials (EMs) due to high energy densities and adiabatic flame temperatures, which are comparable or greater than those of traditional organic based energetics (e.g. RDX). Unlike organic EMs, nanothermite performance is easily tuned through variations in stoichiometry, packing density, or oxidizer composition. However, due to large characteristic diffusion length scales, traditional thermites burn at a much slower rate than organic energetics, which have the fuel and oxidizer mixed at the molecular level. Nanothermites are most commonly comprised of aluminum (fuel) and metal oxide particles with primary sizes <100 nm. Reduced lengths scales, implying decreased diffusion lengths, help nanothermites to demonstrate burn rates up to several orders of magnitude higher than comparable microscale thermites [6-8, 31, 32].

Given the central role that nanoaluminum (by far the predominant fuel) plays in the reaction, much attention has been given to understanding the transport of metallic aluminum with respect to its inherent Al_2O_3 shell. The exact nature of aluminum transport is not known, but several models have been proposed including aluminum and oxygen diffusion through the alumina shell [13], pressure build up due to melting of the aluminum, which ruptures the shell allowing Al to leak out [56], and extreme pressure

build up causing eruption of the alumina shell that spallates the molten aluminum [12]. Regardless of the argument, it can be agreed that rapid heating of an aluminum particle will have a positive effect on the transport of aluminum.

In recent studies interest has shifted towards understanding the effect of different oxidizers on the nanothermite reaction [41, 52, 57]. Because of the large variety of metal oxides available, each with different physical, chemical, and electrical properties, the potential to change the energy release profile becomes feasible. One metal oxide of particular interest is bismuth trioxide (Bi_2O_3), which has a relatively low vapor pressure and unique conducting properties at higher temperatures. Bi_2O_3 is well known as a good oxide ion conductor, and has been highly researched for use in electrochemical cell applications [58-62]. The δ-phase of Bi_2O_3, which is stable from 1002-1097 K [59, 62], shows an advanced ion conductivity up to two orders of magnitude greater than that of its other phases [58].

When nanoscale Bi_2O_3 is combined with aluminum nanoparticles, a very reactive nanothermite is formed [57, 63-65]. Sanders *et al.* [57] investigated the difference between four aluminum nanothermites Al/CuO, Al/Bi_2O_3, Al/MoO_3, and Al/WO_3. Each of these thermite mixtures was subjected to tests in a closed bomb pressure cell, open tray burn, and burn tube. Their results show that Al/Bi_2O_3 produces the largest peak and average pressure, consistent with equilibrium calculations that indicate it produces the most gaseous species during combustion when compared to other oxidizers [52, 57, 66]. However, Al/Bi_2O_3 is reported to have the lowest propagation velocity in burn tube experiments and a slightly lower propagation rate than Al/CuO in the open tray experiments [57]. Contrary results were seen in open tray experiments by Puszynski *et al.*

where Al/Bi_2O_3 produced higher burn rates than Al/CuO, Al/MoO_3, or $Al\text{-}WO_3$ [66]. This group also performed DSC at slow heating rates of 1-20 K/min, and showed the peak of the exotherm to be in the range of ~839-861 K depending on the size of the Bi_2O_3 particles. A recent study on Al/Bi_2O_3, and its dependence on aluminum particle size and Al_2O_3 shell thickness was performed by Wang *et al.* [65]. They observe a burn rate nearly 30 times greater with nanoaluminum, relative to 70 micron aluminum. Measured ignition temperatures were between 749-797 K for heating rates of 53.4-92.5 K/min.

Our group has several previous studies characterizing nanothermite reactions [25, 29, 41, 67-69]. In particular, we have highlighted the role of oxygen release, and its relationship to ignition temperature and ignition delay [41]. We have also investigated the formation of ionic species during the nanothermite reaction in Al/Bi_2O_3, Al/CuO, Al/Fe_2O_3, and Al/WO_3, demonstrating that the bismuth oxide thermite produces the highest rate of ion release [29]. More recently, we proposed that nanothermites undergo a 'reactive sintering' mechanism when subjected to rapid heating [67, 70]. In this mechanism, initiation of the reaction occurs in the condensed-phase at points of interfacial contact. As heat is generated by the reaction, it is conducted to neighboring particles, which further induces melting and rapidly increases in the intimate contact at the reacting surface.

In this study the Al/Bi_2O_3 nanothermite is investigated with a variety of diagnostic tools at heating rates of more than 10^5 K/s. Because of the interesting and in some cases contradictory behavior of the Bi_2O_3 nanocomposites, and the lack of mechanistic studies at high heating rates, we present our results for time resolved temperature-jump mass spectrometry and temperature-jump SEM. C/Bi_2O_3 was also examined to further probe

the fuel/oxidizer interaction, under conditions where the fuel in this case is involatile. The results for C/Bi_2O_3 and Al/Bi_2O_3 are directly compared to draw some conclusions about the governing mechanisms in each system. Analysis suggests that Bi_2O_3 is indeed unique in that it clearly demonstrates the ability to rapidly initiate a reaction in the condensed phase, and provides further evidence towards a condensed state 'reactive sintering' mechanism.

4.2. Experimental

Nanothermite samples were stoichiometrically mixed using aluminum and Bi_2O_3 nanoparticles particles following the formula

$$2Al + Bi_2O_3 \rightarrow Al_2O_3 + 2Bi \qquad (1)$$

where Bi_2O_3 (Sigma-Aldrich) has a primary particle size of ~100 nm, and aluminum (Argonide, Corp.) has an average particle size of ~50 nm as specified by the manufacturer. C/Bi_2O_3 samples were also stoichiometrically mixed assuming

$$3C + 2Bi_2O_3 \rightarrow 3CO_2 + 4Bi \qquad (2)$$

with "regal 300" carbon black (Cabot Corp.), which has a primary particle size of ~50 nm (determined by SEM). While calculating stoichiometry the inherent Al_2O_3 shell on the aluminum nanoparticle was considered. The shell was taken to be 30% of the mass as previously determined through gravimetric analysis.. The samples are initially placed in a hexane solution and are sonicated for ~20 min to ensure a fine mixing of materials.

The primary experimental tool is the Temperature-Jump/Time-of Flight Mass Spectrometer (T-Jump/TOFMS) [22]. In addition to the T-Jump/TOFMS, several complementary studies were performed. The experimental procedure for our

nanothermite self-ionization study is given elsewhere [29], but in short, the setup is that of the normal T-Jump/TOFMS without the use of the electron gun. Therefore any ions that are detected by the MCP are strictly from ionization during the reaction. Nanothermite samples Al/Bi_2O_3, Al/CuO, and Al/Fe_2O_3 were also tested in a constant volume pressure cell that has its experimental details described elsewhere [71]. A heating holder (Protochips, Inc.) was also used to visually investigate the morphological changes of Bi_2O_3 inside a scanning electron microscope (SEM). This holder provides *in situ* heating from room temperature to a maximum of 1473 K, at a rate of 10^6 K/s. Images from before and after the heating event can be compared to draw some conclusions about how the reaction occurred. In the context of the mass-spectrometry results we consider this as "T-Jump microscopy "

4.3. Results

4.3.1 T-Jump Mass Spectrometry

To gain a better understanding of each material's role in a nanocomposite reaction, the Al/Bi_2O_3 and C/Bi_2O_3 samples as well as neat carbon, aluminum, and bismuth trioxide samples were each tested with the T-Jump/TOFMS. Our primary interest is in the Al/Bi_2O_3 nanothermite for energetic applications, but the C/Bi_2O_3 system offers a valuable mechanistic perspective as aluminum and carbon are very different with respect to their phase changes at the temperature regime of this experiment. We begin our analysis with the time resolved mass spectra of the reaction products from rapid heating of Al/Bi_2O_3 and neat Bi_2O_3 nanopowders. For each case the heating rate was set to ~$3x10^5$ K/s producing a final temperature of ~1320 K. It should be noted that our

TOFMS has a background signal at m/z 18, (H_2O^+) and minor peaks at m/z 17, 28, and 32, representing OH^+, N_2^+, and O_2^+, respectively. A typical spectrum obtained during Bi_2O_3 heating is shown in Figure 4.1.

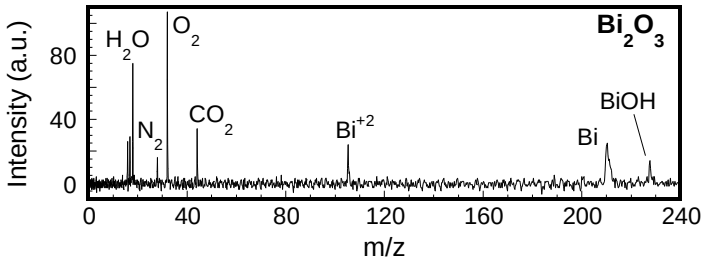

Figure 4.1: Time-of-flight mass spectrum for Bi_2O_3 sample.

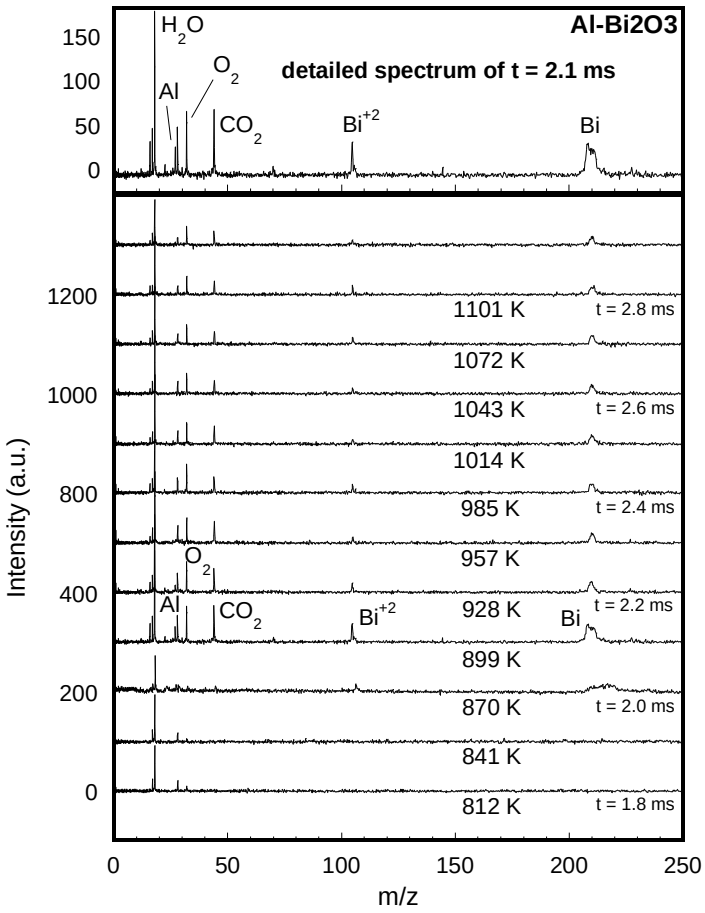

Figure 4.2: Full spectrum for Al-Bi_2O_3 nanothermite reaction. Each spectrum is separated in time by 100 µs.

Decomposition products include m/z 32 (O_2^+), m/z 44 (CO_2^+), m/z 104.5 (Bi^{+2}), m/z 209 (Bi^+), and m/z 216 (BiOH). A full time-resolved set of spectra of the Al/Bi_2O_3 reaction is shown in Figure 4.2 where the initiation of the reaction occurs at 870 ± 40 K. The detailed Al/Bi_2O_3 spectrum in Figure 4.2 shows reaction products of Al^+, Bi^+, Bi^{+2}, O_2^+, and CO_2^+. CO_2 production is an unexpected byproduct of our sonication procedure, as residual carbon remains after drying of the nanothermite. The carbon and metal oxide undergo a low temperature reaction producing CO_2 gas as in reaction (2).

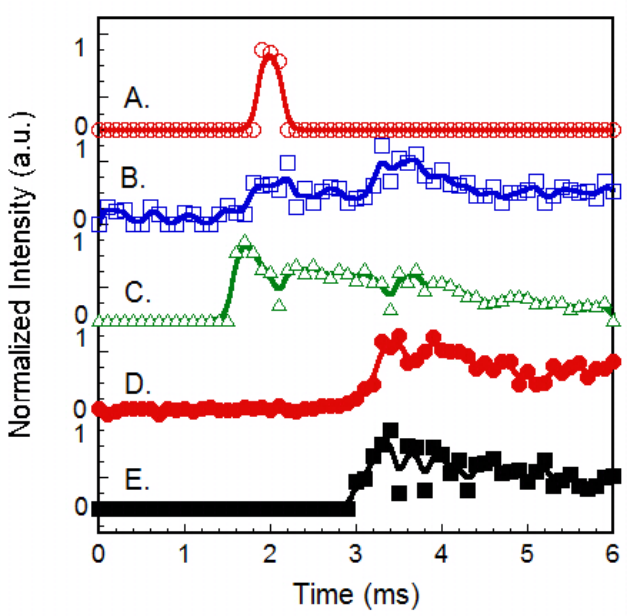

Figure 4.3: (A-C) Products from rapid heating of Al/Bi_2O_3. (D-E) Products from rapid heating of neat Bi_2O_3. (A) Al, (B) O_2, (C) Bi, (D) O_2, (E) Bi.

The temporal nature of the T-Jump mass-spectrometer experiment allows us to draw some conclusions about the initiation steps that may be involved with the bismuth nanothermite, and how it differs from other systems. In our previous work, we studied the nanothermite reaction of Al/CuO, Al/Fe_2O_3, and Al/ZnO [41]. For each of these materials we investigated the decomposition of the thermite, as well as decomposition of

the metal oxide and aluminum nanopowders. We found from comparing neat metal oxide spectra with respective nanothermite spectra that the thermite reaction initiates at a time and temperature in close proximity to the point of gaseous O_2 release from the neat oxidizer. In comparison, Al/Bi_2O_3 shows significantly different reaction characteristics. Figure 4.3 shows the reaction product concentrations as detected by the mass spectrometer for Al/Bi_2O_3 and Bi_2O_3 in the current study. If we compare the reaction products in Figure 4.3 for heating of the thermite (parts A-C) and the neat oxide (parts D-E), we see that unlike other nanothermites, there is a significant difference in times between thermite ignition, and gas phase O_2 release from the oxide. Although these two samples were tested in separate heating runs, the experimental conditions were replicated in a similar fashion so that qualitative conclusions can be confidently made. We see that during oxide heating, Bi and O_2 are released very late at ~3.1 ms. For nanothermite heating, combustion starts at ~1.6 ms, as signified by the appearance of Bi, O_2, and shortly after, Al. Clearly, unlike the iron oxide and copper oxide thermite reaction systems where ignition occurs close to the point of O_2 release, the initiation of the Al/Bi_2O_3 occurs well before the Bi_2O_3 decomposes to release a gaseous oxidizer. This evidence indicates that the initiation of the Al/Bi_2O_3 reaction occurs in the condensed phase, although volatilization of the aluminum remains a concern.

To further investigate the possibility of a condensed phase reaction we consider a fuel which will not change phase (i.e. melt or vaporize) at the temperatures relevant to this experiment. For this purpose we employ a C/Bi_2O_3 thermite using nanometer scale carbon particles. Figure 4.4 displays the CO_2 release and Figure 4.5 shows O_2 release

from the carbon, Bi_2O_3 and C/Bi_2O_3 heating experiments. From reaction (2) we expect the C/Bi_2O_3 composite to produce carbon dioxide gas, which is observed in Figure 4.4.

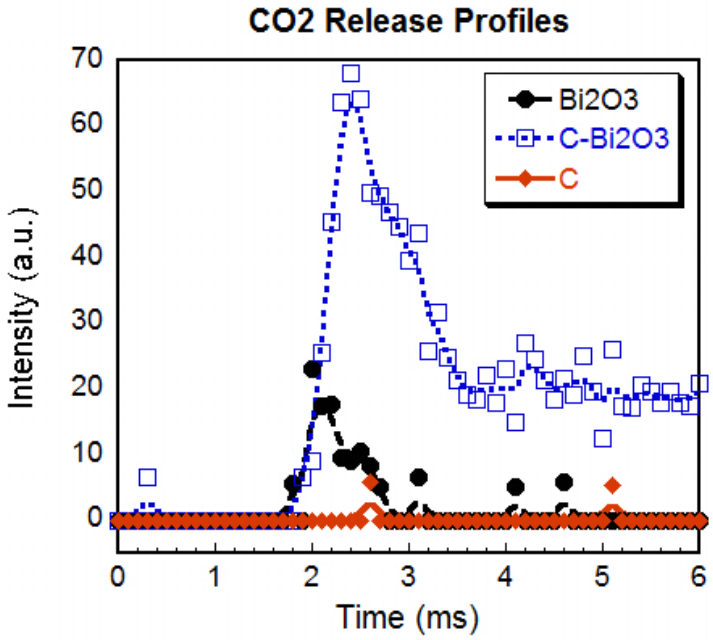

Figure 4.4: Carbon dioxide release from T-Jump/TOFMS experiments on Bi_2O_3 and C powders, and the C/Bi_2O_3 thermite.

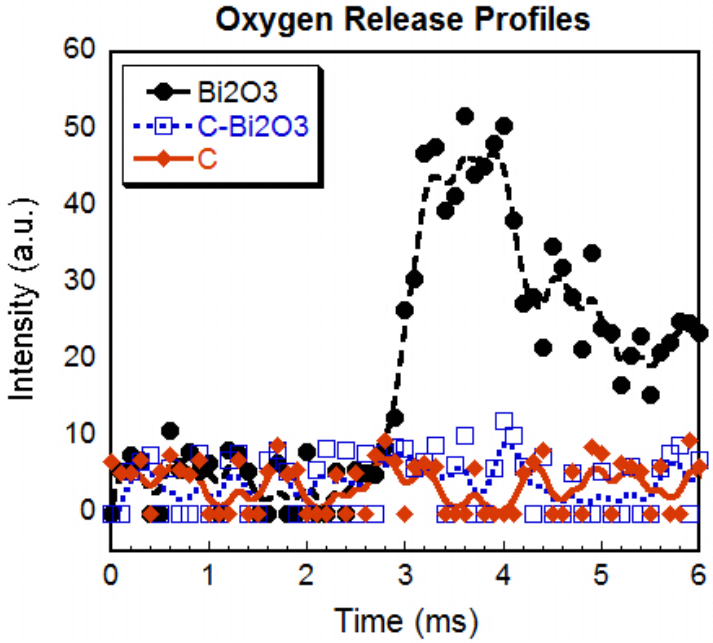

Figure 4.5: Oxygen release from T-Jump/TOFMS experiments on Bi_2O_3 and C powders, and the C/Bi_2O_3 thermite.

Interestingly this occurs at the same temperature as the initiation of the Al/Bi_2O_3 reaction, ~870 K. Furthermore, time for initiation of combustion (point of CO_2 release in Figure 4.4) is nearly a millisecond earlier than the point of oxygen release from the bismuth oxide powder seen in Figure 4.5. There is also essentially no oxygen seen during the C/Bi_2O_3 reaction, suggesting that it is completely consumed in the reaction. This result is, in our opinion, fairly convincing proof of condensed phase initiation in C/Bi_2O_3 and by inference, also Al/Bi_2O_3. The use of carbon as the fuel, and the similar reaction temperature of the two composites, shows that the initiation of the reaction is largely dependent on how the oxide transports its oxidizer in its condensed state.

4.3.2. T-Jump Electron Microscopy

To further explore the idea of a condensed phase combustion mechanism, we investigate the morphological changes of $Al/C/Bi_2O_3$, using *in situ* rapid heating within a scanning electron microscope (SEM, Hitachi SU-70). The initial study was designed to investigate the reaction between clusters of Al and Bi_2O_3 particles. To approach this problem a very sparse coating was applied to the SEM grid resulting in isolation of the two components as seen in Figure 4.6. As a result of this sparse coating, the sample grids, which have a few nanometers thick holey carbon film deposited over a silicon carbide substrate, offer the opportunity to study the heating of Al and Bi_2O_3 as well as reactions with the underlying carbon substrate. Figure 4.6 shows an SEM image of the sample on the grid before heating. The dark background is the thin carbon film and the light, grainy surfaces are holes in the carbon film which expose the underlying silicon carbide.

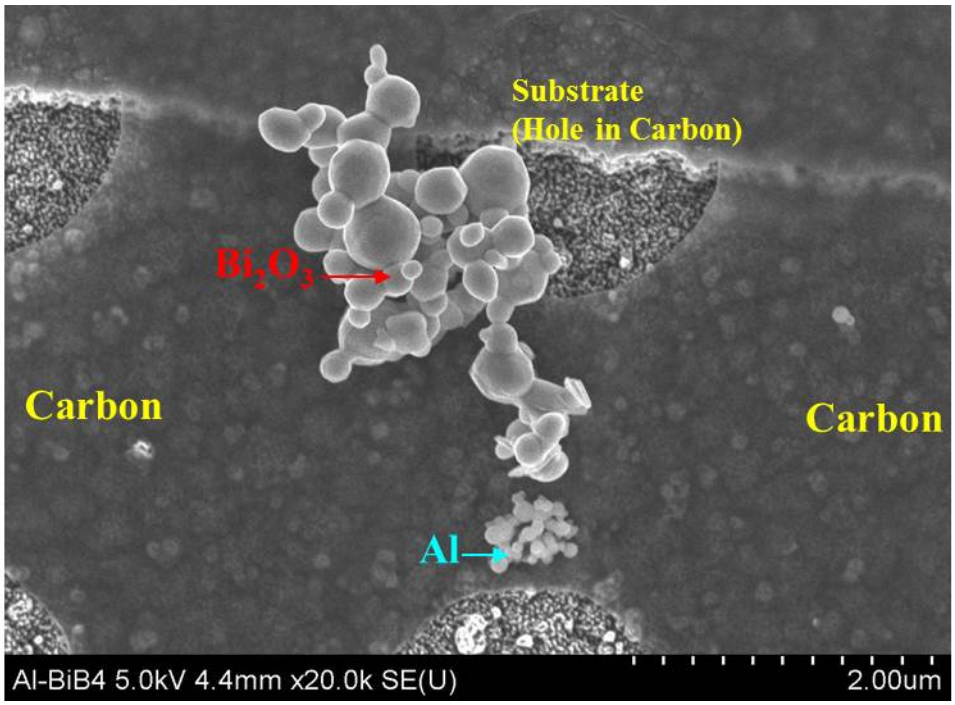

Figure 4.6: TEM image of bismuth trioxide and aluminum nanoparticles before heating.

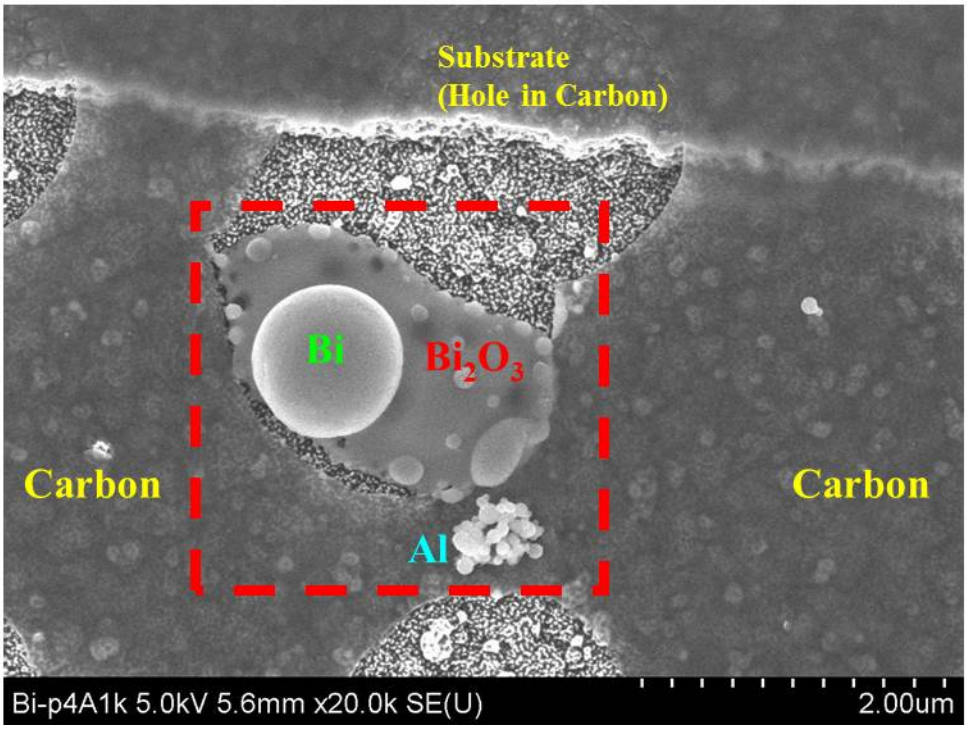

Figure 4.7: SEM image of Bi_2O_3 and Al particles after heating with high heating rate TEM grid. Dotted box represents area sampled by EDS shown in Figure 4.8.

The sample was given a heating pulse from room temperature to 1273 K at a rate of 10^6 K/s and then held for 1 ms; the results of which are shown in Figure 4.7. Elemental analysis of the sample after heating using energy dispersive x-ray spectroscopy (EDS) is shown in Figure 4.8.

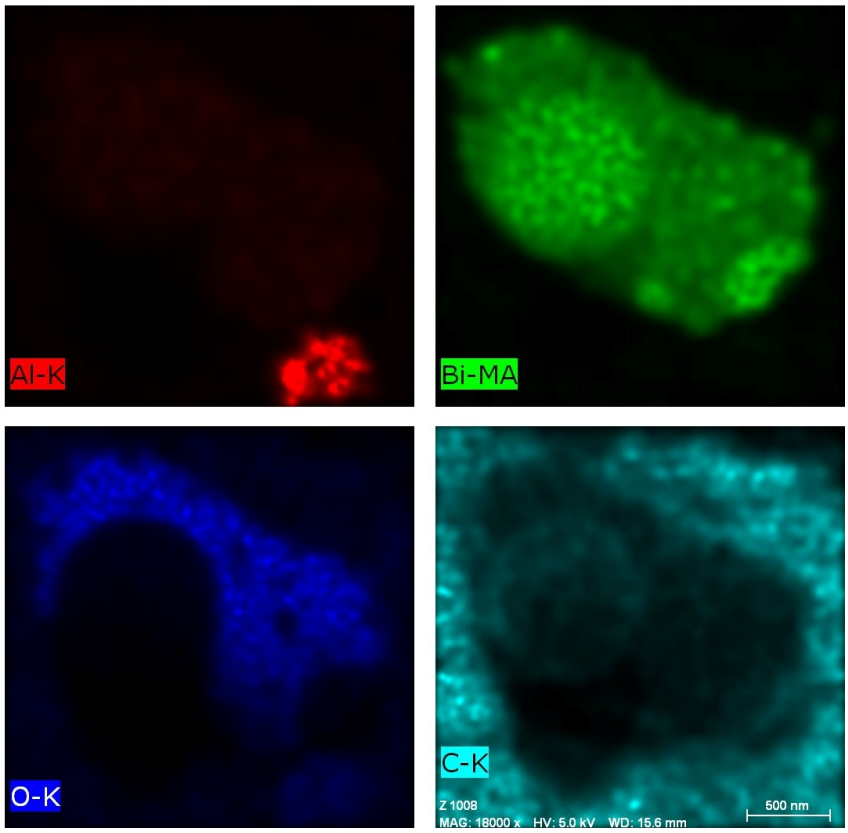

Figure 4.8: Elemental analysis of boxed region in Figure 4.7.

Due to the isolation of Al and Bi_2O_3 no reaction was observed between these two components. Despite the fact that we were well above the melting point of aluminum, it is clear that the aluminum aggregate did not undergo any sintering. However, the Bi_2O_3 showed significant changes within the 1 ms timescale of the heating pulse. It should be noted that with a longer heating pulse the aluminum will also show significant

morphological change [67]. One would expect that since aluminum melts at 933 K and bismuth trioxide melts at 1097 K that we would see some changes in aluminum before Bi_2O_3. These results suggest that either the timescale of heat conduction is significantly lower in Al than in Bi_2O_3, or that the alumina shell is robust enough to withstand the overpressure created by melting of the aluminum core. Using conductivity and heat capacity values from the literature [72-74] the thermal diffusivities at room temperature were determined to be 0.9 $cm^2 \cdot s^{-1}$, 0.08 $cm^2 \cdot s^{-1}$, and 0.02 $cm^2 \cdot s^{-1}$ for Al, Al_2O_3, and Bi_2O_3, respectively. Since the heat transfer in aluminum and alumina are both much faster than that of bismuth oxide, we assume that the aluminum core is melting but not rupturing the Al_2O_3 shell. Prior work using molecular dynamics simulation supports the idea that the alumina shell remains intact under rapid heating conditions with a diffusion of the core aluminum through the shell [44].

EDS analysis in Figure 4.8 confirms that during heating of the Bi_2O_3 nanoparticles, a film of Bi_2O_3 is formed, over which spheres of Bi reside on its surface. In this case liquid Bi_2O_3 is reacting with the underlying carbon substrate, which can be seen by the recession of the hole in the carbon film from Figure 4.6 to Figure 4.7. The C/Bi_2O_3 reaction occurs via condensed-phase reactions producing CO_2 gas and liquid Bi (MP 545 K). The liquid bismuth is immiscible in liquid Bi_2O_3, which promotes phase separation and the formation of large spherical particles of bismuth. This result is highly consistent with the condensed phase reaction model deduced from the T-Jump/TOFMS experiments. The fact that the liquid Bi_2O_3 wets and reacts with the carbon surface further suggests that there is a transfer of oxygen through the liquid Bi_2O_3 phase.

We also note that the reaction has proceeded to completion within the timescale of the heating pulse, <1 ms. The reaction may have occurred faster, however, 1 ms was the minimum pulse which could be applied. This may imply that very thin carbon is a viable fuel to use in a thermite formulation, so long as the length scales are sufficiently small. If carbon could be utilized as a fuel, then much higher overpressures could be realized via the formation of a gaseous CO_2 product, thus greatly improving the performance. Carbon is also unique in that it does not have a passivating oxide shell like that of metal surfaces. The presence of an oxide shell adds a relatively inert element to nanothermite compositions and can result in ignition delay caused by diffusion of species through the shell as previously reported for aluminum nanothermites [25].

4.3.3. High Speed Imaging

For select Al/Bi_2O_3 combustion experiments high speed imaging was used to capture the nanothermite reaction while simultaneously sampling with the T-Jump/MS. Figures 4.9 and 4.10 show selected images of the T-Jump experiments under vacuum for Al/Bi_2O_3 and Al/CuO respectively at a framing rate of ~33,000 fps. Ignition temperatures are observed at ~870 K for Al/Bi_2O_3 and ~1040 K for Al/CuO, and from images in Figures 4.10 and 4.11 we conclude that Al/Bi_2O_3 burns about twice as fast as Al/CuO with burn times of ~0.09 ms and ~0.18 ms, respectively.

Previous burn tube and open tray experiments have given mixed results as to whether Al/CuO or Al/Bi_2O_3 exhibits a higher burn rate because of the difficulty in controlling experimental parameters. Packing density, particle size, tube diameter, and pressure are just a few critical experimental parameters that greatly influence burn rate

results. If we consider the work by Sanders and co-workers with aluminum nanothermites of CuO, Bi_2O_3, MoO_3, and WO_3 in both open tray and burn tube setups [57].

Figure 4.9: High speed images of Al/Bi_2O_3 during heating in the TOFMS.

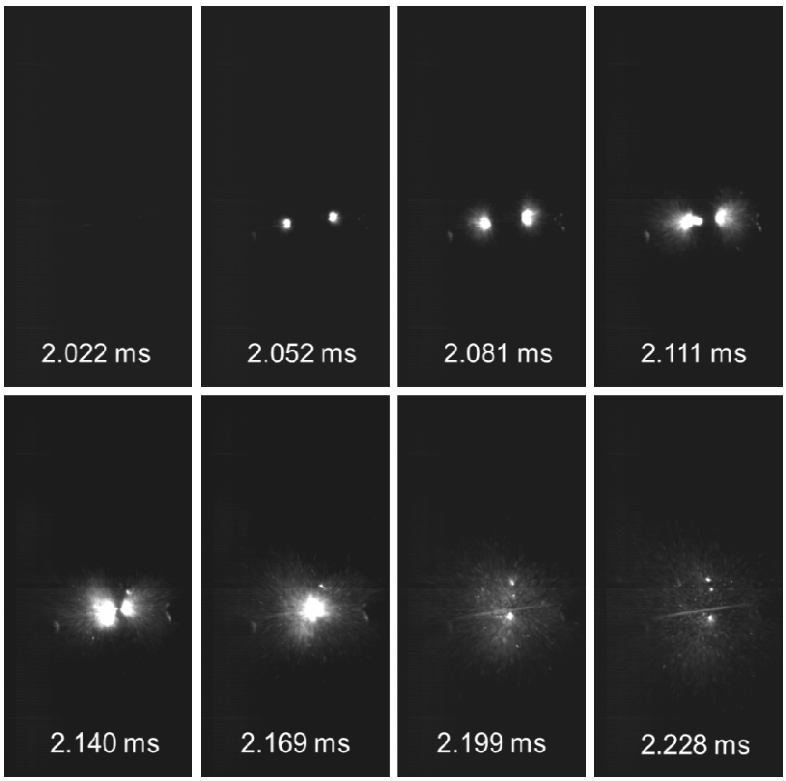

Figure 4.10: High speed images of Al/CuO during heating in the TOFMS.

Their results show that Al/CuO has the fastest burn rate in open tray experiments followed by Al/Bi_2O_3, while in the burn tube, Al/Bi_2O_3 was the poorest performer followed by Al/CuO. In both the burn tube and open tray experiment Al/CuO outperformed Al/Bi_2O_3, however, in our filament tests it is clear that the opposite is true. The primary differences between previous experiments and the current study is that we investigate very small samples under high vacuum conditions, as opposed to bulk samples at atmospheric pressure. The current method allows for analysis of the initial nanothermite reaction with far less dependence on the bulk properties. Due to these sampling conditions we predict that the observed reactions are largely dependent on the condensed phase initiation events. We also conclude that Al/Bi_2O_3 has a much more rapid initial reaction than other nanothermites investigated with this system.

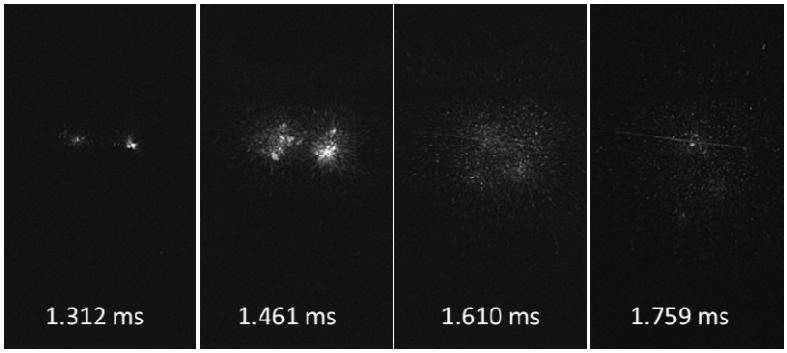

Figure 4.11: High speed images of Al/CuO/Bi_2O_3 during heating in the TOFMS.

A composite of Al/CuO/Bi_2O_3 was also tested with the high-speed imaging T-Jump/TOFMS setup. This sample was mixed stoichiometrically following

$$8Al + 3CuO + 3Bi_2O_3 \rightarrow 4Al_2O_3 + 3Cu + 6Bi \quad (3)$$

where CuO and Bi_2O_3 are given equal molar quantities. Intuition leads us to predict that this system would ignite at the same temperature as Al/Bi_2O_3, as Al/Bi_2O_3 ignites at a lower temperature than Al/CuO. We also expect a rapid initial reaction similar to that of Al/Bi_2O_3. This system does begin decomposition at the same point as Al/Bi_2O_3 however, the reaction lacks the intensity and reaction speed of either Al/CuO or Al/Bi_2O_3 as seen in Figure 4.11. In separate experiments we have noted that Al/Bi_2O_3 does not have a significant drop off in performance for fuel rich cases. In Figure 4.7 we observe wetting of the carbon surface by the Bi_2O_3, and in experiments with other metal oxides we have seen similar sintering events [70]. We attribute the lack of performance to Bi_2O_3 particles wetting both the Al and CuO surfaces. To confirm this we heated a CuO/Bi_2O_3 sample with the T-Jump/TOFMS and saw a spectral pattern similar to that of neat Bi_2O_3. In this case the Bi_2O_3 wets the surface of the CuO and prevents the oxygen release from the CuO particles. Therefore, in the Al/CuO/Bi_2O_3, Bi_2O_3 will wet both Al and CuO which will prevent oxygen delivery by CuO to Al and reduce the contact area between Bi_2O_3 and Al, resulting in a less intense reaction. CuO and Bi_2O_3 also form an intermetallic, $CuBi_2O_4$, well below the melting point of either material [75]. Formation of this intermetallic can further detract from the oxygen delivery from either CuO or Bi_2O_3.

4.4. Discussion

Thus far we have argued that the Bi_2O_3 oxidizer melts and wets the surface of potential fuels to initiate reaction. Despite the low ignition temperature of Al/Bi_2O_3 at 870 K, below the melting point of both bismuth trioxide (1097 K) and aluminum (933 K),

we believe that this mechanism holds. In a recent work, we used in-situ rapid heating experiments within an SEM, and observed that particle melting is not a necessary prerequisite to initiate a condensed-phase reaction for the Al/WO_3 system [67]. It was seen that WO_3 particles isolated from Al did not undergo any morphological changes. However, in regions where the fuel and oxidizer were intermixed, significant morphological changes indicative of WO_3 melting were observed. This observation led us to speculate that the reaction initiated below the melting temperature of WO_3, and the liberated energy further promoted melting of neighboring WO_3 particles to induce reactive sintering. In the context of this work, a similar mechanism may be occurring, and would serve to explain why the Al/Bi_2O_3 reaction initiates below the melting point of either constituent.

One potentially useful material property is the Tammann temperature, which for Bi_2O_3 is ~549 K, or half of its melting point. At temperatures approximately that of the Tammann temperature nanoparticles begin to sinter as surface atoms gain a significant amount of mobility [76]. We assume that a similar event will occur for the Al core of the aluminum nanoparticles, and that both the Al and Bi_2O_3 are in a liquid-like state at the point of ignition. A similar effect was predicted by Wang *et al.* for combustion of aluminum in their Al/Bi_2O_3 nanothermites. They note that due to the small size of nanoaluminum, it will not only melt rapidly, but do so at a depressed temperature [65]. We expand this to consider that both Al and Bi_2O_3 are able to melt, and that once sintering occurs between the aluminum nanoparticle and Bi_2O_3, a junction is created between the two materials, and the mobility of each allows for diffusion through the Al_2O_3 shell.

This does not completely explain why the Bi_2O_3 thermite reacts so much faster than the CuO thermite in the T-Jump/TOFMS. Of the three proposed aluminum transport methods mentioned in the introduction, recent T-Jump experiments at atmospheric pressure have shown evidence to support a diffusion limited reaction. That work reports the observance of an ignition delay for the nanothermite samples which increases with increasing thickness of the aluminum particle's oxide shell [25]. From the measured ignition delay as a function of shell thickness, a self-consistent effective diffusion coefficient was extracted which supports a transport limited mechanism. Molecular dynamics simulations were also performed showing that electric fields within the aluminum nanoparticle could play a significant role in aiding aluminum diffusion through the oxide shell [77]. This work demonstrates how an electric field across the oxide shell could drive positive Al ions through the oxide shell to the outer surface of the particle. This study along with work by Zhdanov and Kasemo [78] suggest that in Al nanoparticles, the diffusion rate for Al cations through the oxide shell is greatly enhanced by this local electric field.

For bismuth trioxide, there is also significant evidence that at temperatures slightly higher than that of the ignition point of Al/Bi_2O_3, the oxide can promptly produce and transport negatively charged oxide species [59]. We have already assumed that nanoscale bismuth oxide and the aluminum core will begin phase change processes at temperatures below that of the bulk materials. If this is the case, then transport processes associated with these phase changes will also occur at lower temperatures. Therefore it is highly likely that at the ignition point of Al/Bi_2O_3 we have a rapid transport of fuel and oxidizer through the alumina shell which is aided by an electric field and ions with

opposing electric charges. We have experimentally shown an enhanced rate of ion production in the Al/Bi_2O_3 compared to other common nanothermites [29]. Furthermore we have shown that the ion production for Al/Bi_2O_3 occurs at the onset of combustion, implying that the ion production is related to the thermite ignition whether it be as a precursor to ignition or as a player in the mass transport process. The large presence of ionic species and the timing of ion formation combined with the inherent electric field of aluminum particles further support the idea that electric fields have a role in nanothermite initiation. Furthermore, the suggested superiority of the Bi_2O_3 ion transport could help to explain why the initiation of this thermite occurs faster than other nanothermite samples.

A final remark relating to the transport of aluminum through the Al_2O_3 shell and the Al/Bi_2O_3 initiation event, can be gathered from further analysis of Figure 4.7. If we consider several pieces of evidence, this image gains significant meaning:

1. Al/Bi_2O_3 and C/Bi_2O_3 react at the same temperature
2. In Figure 4.7 reaction is observed for C/Bi_2O_3
3. No changes are observed for Al, despite temperatures being greater than that of $AlBi_2O_3$ initiation.

This information shows that despite being above the ignition point of Al/Bi_2O_3, the aluminum nanoparticles appear to be completely intact, and no aluminum appears to leak out. A closer comparison of the aluminum particles from Figures 6 and 7 are shown in Figures 4.12 (before heating) and 4.13 (after heating) showing little to no morphological change. This suggests that during rapid heating events contact between the metal oxide and aluminum plays a significant role in drawing the aluminum through the Al_2O_3 shell at a high rate. We have noted the possible role electric fields and charged species above,

and the phenomenon observed in Figure 4.7 may be evidence that the added electric field gradient created by negative species in the metal oxide may in fact play a large role in the initiation. We also note the gradient of chemical species created by contact of the oxide and aluminum may in itself be the driving force behind the diffusion process.

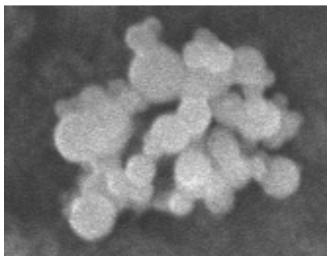

Figure 4.12: Al particles from Figure 4.6 before rapid heating.

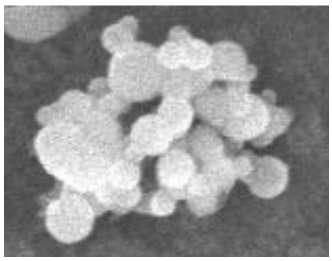

Figure 4.13: Al particles from Figure 4.7 after rapid heating.

4.5. Conclusions

This study provides an intuitive look into the initial reaction events of the nanothermite reaction. In the aforementioned 'reactive sintering' study, significant evidence was provided for a condensed state reaction playing an important role in nanothermites. The current study is not only a complement to 'reactive sintering' but it also provides definitive evidence that the condensed phase reaction is responsible for ignition and is not a result of the bulk reaction. Observation of this event in both Al/Bi_2O_3 and C/Bi_2O_3 further demonstrates that the ability of the oxide to transport its oxidizer is a key feature when considering nanothermite formulations. Although the

current study only examines Bi_2O_3 containing systems, the evidence for condensed phase reaction demonstrated here, along with the results of the reactive sintering study, suggest that this mechanism is at play for other systems as well. Significant evidence also points to electric fields and charged particles having a hand in the rapid speed of the initial nanothermite reaction, and could be the focus of future nanothermite studies.

Chapter 5: Evidence for the Predominance of Condensed Phase Reaction in Chemical Looping Reactions between Carbon and Oxygen Carriers

Following the demonstration of a condensed phase reaction for Al/Bi_2O_3, and C/Bi_2O_3 it is necessary to show that this mechanism is valid for other systems. For Al/CuO and Al/Fe_2O_3, ignition occurs at the same point as gaseous O_2 release, but condensed phase reactions cannot be ruled out. We have shown Bi_2O_3 to be a unique oxidizer, but it is important to see if other oxidizers can also undergo a condensed phase initial reaction. In nanothermites, aluminum melts at a relatively low temperature (933 K), close to the point of ignition, making it difficult to determine the role of each reactant. To simplify the problem, we investigate carbon/metal oxide mixtures as carbon will not undergo phase change in the temperature regime of these experiments. Aside from having interest from a mechanistic standpoint, carbon/metal oxide systems are also relevant to chemical looping combustion (CLC) applications.

Chapter 5 Overview

This study investigates the use of metal oxides as an oxygen carrier in chemical looping combustion applications. The initiation and decomposition of C/CuO and C/Fe_2O_3 are investigated using a time-resolved T-Jump/Time-of-Flight Mass Spectrometer (T-Jump/TOFMS). Heating of the metal oxide nanopowders produces gaseous O_2, but when mixed with the fuel (carbon) this is formed temporally after the primary combustion product of CO_2. This latter result points to condensed phase reaction between the metal oxide and carbon as the predominant reaction mechanism rather than

gas phase release of O_2 and subsequent burning of carbon, at least in the initiation phase. High speed imaging, in-situ heating SEM, and TEM are also used to further investigate the reaction. The oxidation rate of carbon in the present experiment is estimated to be 3 to 5 orders of magnitude greater than that predicted using the Nagle Strickland-Constable model. The activation energy of C/CuO, C/Fe_2O_3, and C/Bi_2O_3 are determined using the Ozawa isoconversion method, and are found to be 97 kJ/mol, 180 kJ/mol, and 170 kJ/mol, respectively. The condensed phase nature of this reaction is compared to our previous studies on aluminum nanothermites, and is considered to be further evidence towards a reactive sintering initiation mechanism.

5.1. Introduction

Carbon combustion remains a primary energy source for meeting the world's current and future energy demands. However, CO_2 production during combustion remains a critical issue. Carbon sequestration is one method to prevent CO_2 release, but this process generally has significant monetary and energy use concerns. Chemical looping combustion (CLC) was originally conceived as a method to increase the thermal efficiency of power generation stations, but it was later recognized as having potential for CO_2 sequestration with coal and other heavy hydrocarbon sources with minimal energy penalty [79]. By using metal oxides as the oxygen carrier there is potential for CO_2 as the only gas phase reaction product (with air as the oxidizer N_2 gas and other nitrogen containing species are prominent), enabling easier sequestration.

The majority of CLC studies use a fluidized bed reactor, which flows syngas over an oxidizing agent made up of neat metal oxide particles or a metal oxide/inert support

system [80-83]. These experiments tend to focus on implementation of a CLC system and reproducibility of the oxygenation and reduction processes. A few studies also examine direct oxygenation of the fuel by the metal oxides [84, 85]. Siriwardane and co-workers investigated the reaction mechanism of CuO and carbon particles, and found significant differences in the reaction when the two materials are in contact, compared to when they are separated by a small gap. When the materials are in contact, a low temperature mechanism is observed, where C and CuO react through a condensed phase reaction between 673 and 873 K. They suggest that the surface of the CuO, which has a Tammann temperature of ~678 K, melts and provides a pathway for oxygen distribution to the solid coal [85]. The use of this low temperature reaction may result in a more efficient process if a lower energy input is required to sustain combustion. To improve this method even further, more must be known about the mechanism of reaction between the fuel and oxidizer.

A mixture of carbon and metal oxide particles is physically similar to an aluminum thermite [70] and may share mechanistic properties, which we take into account when considering the carbon reaction. However, as with the chemical looping process, most thermite studies fail to probe the oxygen delivery mechanism to the aluminum fuel, and this process remains unclear. We have previously highlighted the correlation of nanothermite ignition with gaseous oxygen release from the metal oxide [41]. While there is a clear trend between these two events it is still not conclusive that the mechanism is a heterogeneous reaction between the condensed phase aluminum and gaseous oxidizer.

Several previous experiments within our group have suggested a possible condensed phase reaction mechanism for aluminum nanothermites. Our recent study on Al/Bi_2O_3 has shown that this nanothermite ignites at a temperature well below that where gas phase O_2 is released from Bi_2O_3 [86]. Since the system is reacting without the presence of a gas phase oxidizer, this suggests that there is condensed phase chemistry occurring. We have also performed a high heating rate SEM study, which allowed for in-situ heating of aluminum nanothermites, and imaging before and after heating [67]. The system was used with an Al/WO_3 nanothermite that demonstrated significant morphological changes between fuel and oxidizer particles that were in contact. Particles that were not in contact demonstrated little to no morphological changes. From this study we proposed a 'reactive sintering' model to explain the initiation of nanothermite reactions. This model predicts that when the fuel and oxidizer are in intimate contact, a reactive sintering event occurs that increases the effective surface area and further promotes reaction. However, due to the relatively low melting point of aluminum in each of these studies, the mechanism becomes complex and it is not clear whether this reaction requires aluminum to be in the liquid phase.

With carbon as a fuel, the reaction will be governed by oxide transport to the carbon, since carbon will remain in the solid phase within the temperature regime of T-Jump heating experiments (unlike an aluminum fuel). The concern is whether the oxygen carrier liberates the oxygen to the gas phase or alternatively transports the oxygen to the fuel in the condensed phase. During our study of Al/Bi_2O_3 with high heating rate SEM, further evidence for condensed phase reaction was observed as sparsely coated Al and Bi_2O_3 nanoparticles on a carbon film showed that bismuth oxide reacted with the

underlying carbon film, rather than the nearby aluminum [86]. This was further investigated using the T-Jump/TOFMS and a C/Bi_2O_3 mixture, for which a condensed phase reaction was also observed. However, Bi_2O_3 is a unique oxidizer in that it changes crystalline phase to δ-Bi_2O_3 shortly before melting and becomes a very efficient oxide ion conductor [59]. This means that Bi_2O_3 effectively transports and produces oxygen ions throughout its condensed lattice, making it an oxide producer and conductor in the condensed phase [59]. While Bi_2O_3 is clearly a unique material, there are limited studies that suggest other metal oxides such as CuO and Fe_2O_3 possess similar properties [70, 85].

Again, most work on soot oxidation or CLC assumes a gaseous oxidizing environment, but some of these studies have contributed significantly to the understanding of the kinetics of carbon oxidation. Previous soot oxidation experiments include, but are not limited to shock tube studies on soot aerosols,[87, 88] thermogravimetric analysis of soot nanoparticles [89], optical analysis of heated carbon rods [90], and flow reactors paired with non-dispersive infrared detection [91] or a tandem differential mobility analyzer [92]. The Nagle and Strickland-Constable (NSC) model, which is outlined by Walls and Strickland-Constable [90], is frequently used to predict the rate of oxidation for carbon and soot particles. When compared with experimental results, this model provides varying degrees of correlation. At high temperatures, Park and co-workers observed oxidation rates that were a factor of two greater than predicted by the NSC model [88], Gilot *et al.* observed slower oxidation rates [89], while Higgins *et al.* obtained a good correlation with the NSC model [92].

The focus of the present study is on characterizing the reaction in a carbon/metal oxide mixture. The concentration profiles of gas phase products are analyzed to

investigate the initiation events. Varied heating rate experiments are also performed to determine the activation energy for the carbon/metal oxide reaction.

5.2. Experimental

The main experimental tool is the T-Jump/TOFMS. All samples are mixed in-house to be stoichiometric following the reaction,

$$C + MO \rightarrow CO_2 + M \quad (1)$$

where the carbon and metal oxides are commercially available nanopowders. The carbon used in this study is "regal 300" from Cabot Corporation (< 50nm), while the metal oxides, CuO (< 50 nm), Fe_2O_3 (< 50 nm), and Bi_2O_3 (90-210 nm), are from Sigma Aldrich with primary particle sizes listed by the supplier. Samples are placed in hexane and ultra-sonicated for ~20 min in order to ensure intimate mixing of the particles. A micropipette is used to apply the sample solution to the platinum filament. After application of the sample and prior to application of the heating voltage, the filament is placed in vacuum and allowed to dry for ~5 minutes.

Varied heating rate experiments were also used to determine the activation energy of the carbon/metal oxide reaction. The C/CuO, C/Fe_2O_3, and C/Bi_2O_3 composites were heated at four separate heating rates ranging from 45,000 to 550,000 K/s, and four data points were recorded at each heating rate. The Ozawa isoconversion method [93]

$$ln(\beta_i) = Const. - \frac{1.05E_\alpha}{RT_{\alpha,i}} \quad (2)$$

was used to determine the activation energy, where β is the heating rate, E_α is the activation energy, T_α is the temperature at a given point of the reaction, and R is the universal gas constant [94]. For each data point, the reported temperature is that of the

filament at 20% of the peak concentration of CO_2 as detected by our mass spectrometer. This value was used as the peak concentration occasionally occurs after the end of the heating pulse, and the initial point of decomposition is sometimes difficult to accurately determine. Since we are probing gas release from the material rather than thermal events, we assume that unlike a differential scanning calorimetry trace [95], the peak concentration represents a constant point of conversion at different heating rates.

The procedure for rapid-heating transmission and scanning electron microscopy (TEM and SEM) is detailed elsewhere [70]. These experiments were performed with a novel sample holder (Aduro holder, Protochips, Inc.) capable of in situ heating at rates of 10^6 K/s.

5.3. Results and Discussion

To investigate the reaction products from rapid heating of carbon/metal oxide mixtures, the neat metal oxides and mixtures were individually heated in separate experimental runs. Preliminary investigation of C/Bi_2O_3 has been performed [86], but further examination is provided below. Figures 5.1a-5.1d show individual detailed spectra for C/CuO and C/Fe_2O_3, and the neat oxide nanopowders CuO and Fe_2O_3, respectively. A typical background spectrum for our mass spectrometer consists of a large peak at mass to charge ratio (m/z) 18 (H_2O) and smaller peaks at m/z 28 (N_2), m/z 32 (O_2) and m/z 17 (OH), which results from fragmentation of the H_2O during ionization. The main reaction product for the carbon/metal oxide combustion in vacuum is CO_2 (m/z 44) as can be seen in both Figures 5.1a and 5.1b, which corresponds to previous studies on C/Bi_2O_3 [86]. There are several smaller peaks observed at m/z 12 (C) and 16 (O) as

well as an increase in m/z 28 (CO), which are all considered to be due to fragmentation of the CO_2 molecule during ionization. This corresponds well to what is reported for the CO_2 mass spectrum in the NIST spectral library [96].

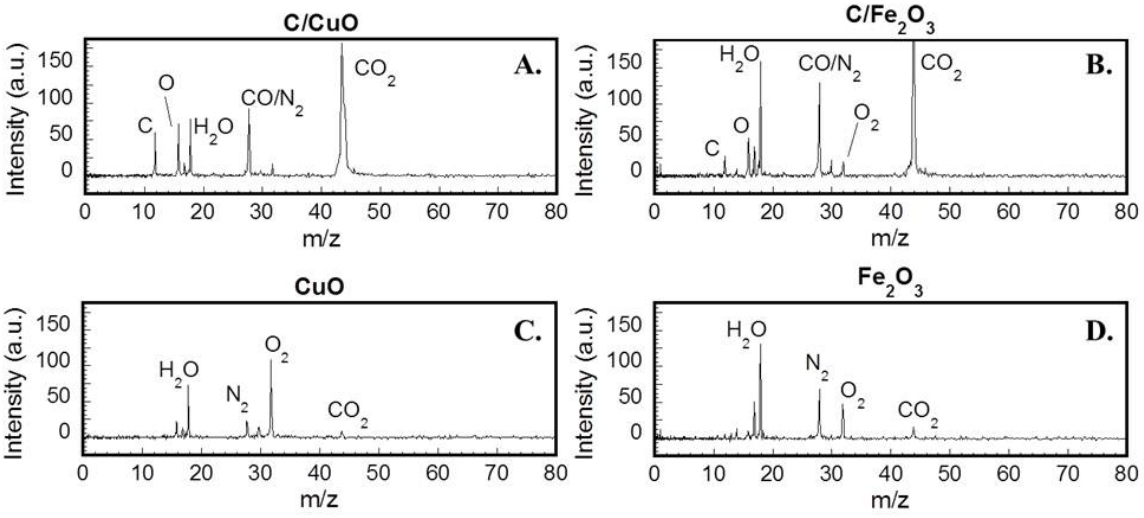

Figure 5.1: Individual mass spectra during rapid heating in T-Jump/TOF experiments of; a) C/CuO, b) C/Fe_2O_3, c) CuO, and d) Fe_2O_3.

The small peak at m/z 32 (O_2) is due to a small amount of oxygen not consumed in the reaction that is released to the gas phase. For the neat nanopowders, there is a significant difference in the amount of CO_2 and O_2 as compared to the fuel/oxide mixtures. In both Figures 5.1c and 5.1d the intensity of O_2 is greater than that in the mixtures, and the CO_2 is substantially decreased. Comparison of the fuel/oxide vs. neat oxide nanopowders shows that the O_2 formed by the metal oxides is almost entirely consumed to form CO_2. Although we have not added any carbon to the neat oxide nanopowders, we do observe some CO_2 production. We expect that this CO_2 production is due to a reaction between the metal oxide and a small amount of residual carbon leftover from the hexane solvent.

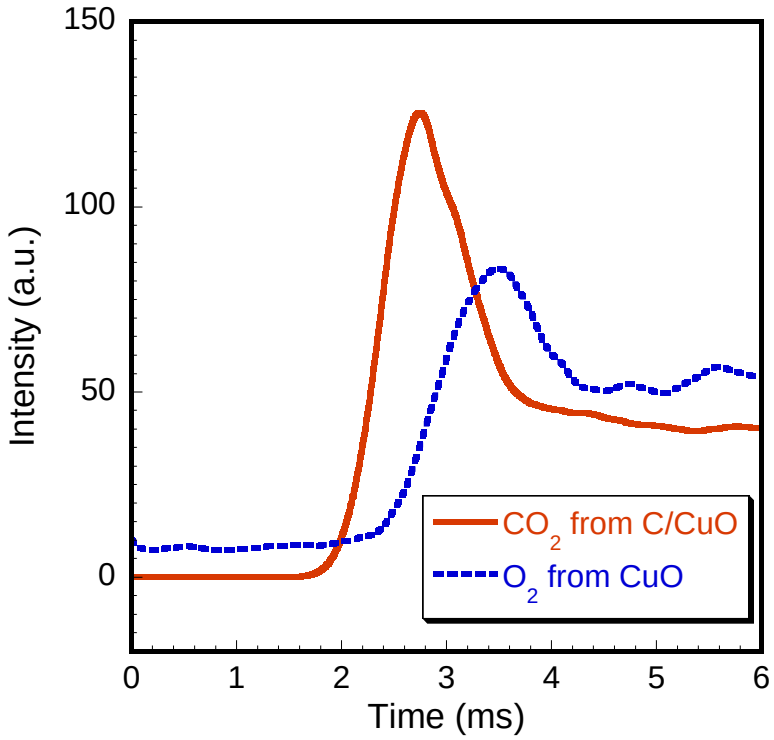

Figure 5.2: Detected product concentrations for CO_2 from C/CuO and O_2 from CuO.

Although carbon dioxide is identified as the prominent gaseous product species, the sequence of the reaction processes is still unclear. To further investigate the reaction pathway, comparison is made between time-resolved profiles of the detected product species for the neat metal oxide nanopowders and the fuel/oxide mixtures. The molecular oxygen release profile from the neat CuO is compared with the carbon dioxide release from C/CuO in Figure 5.2. This gives a correlation between the time that the O_2 is released from the oxide, and when the reaction starts to progress in C/CuO. Although the two traces in Figure 5.2 are from different exper3imental runs, similar heating pulses and wire lengths were used so that comparison between runs can be confidently made. From Figure 5.2 it can be seen that the onset of CO_2 as produced from the C/CuO, occurs at a

lower temperature than O_2 release from CuO. This strongly implies that there is a condensed phase reaction mechanism driving the CO_2 producing reaction. Figure 5.3 plots the CO_2 production from C/Fe_2O_3 along with the O_2 release from Fe_2O_3. This Figure shows the same trend as that for C/CuO; i.e. carbon dioxide is produced well before a gaseous oxidizer is available, therefore the initiation of this reaction must also be in the condensed phase.

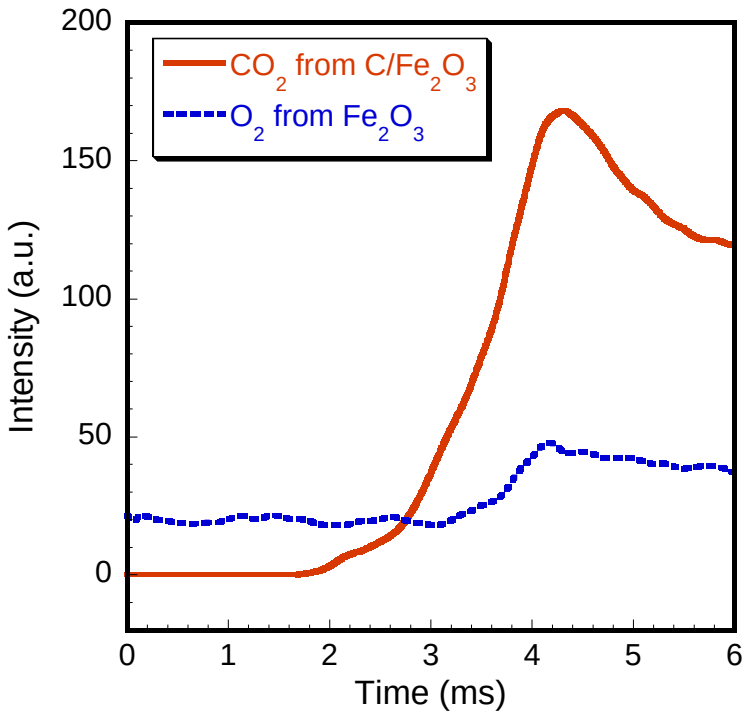

Figure 5.3: Detected product concentrations for CO_2 from C/Fe_2O_3 and O_2 from Fe_2O_3.

To quantify the rate of carbon oxidation a calculation was performed using parameters obtained from the T-Jump/TOFMS experiments. In predicting the reaction rate from the experiments, parameters that require estimation, such as mass and reaction time, conservative estimates were used to avoid bias towards the results. To determine

the reaction rate from our experiment, we consider the oxidation of one carbon nanoparticle within the time scale of the experiment. Assuming a 50 nm carbon particle (mass of ~1.3 x 10^{-16} g) where the reaction occurs at the surface in a time of ~.9 ms (average rise time for CO_2 production from C/Fe_2O_3) we obtain a reaction rate estimation of ~0.007 g·cm^{-2}·s^{-1} for C/Fe_2O_3, ~0.01 g·cm^{-2}·s^{-1} for C/CuO (reaction time of ~.6 ms), and ~0.02 g·cm^{-2}·s^{-1} for C/Bi_2O_3 (reaction time of ~.4 ms).

To compare these predicted reaction rates with traditional carbon oxidation studies, the NSC model is used as applied by Park and Appleton [88], for which the equations are listed below.

$$\frac{w}{12} = \left(\frac{k_A P_{O_2}}{1+k_z P_{O_2}}\right)\chi + k_B P_{O_2}(1-\chi) \quad (3)$$

$$\chi = \left[1 + \frac{k_T}{k_B P_{O_2}}\right]^{-1} \quad (4)$$

$$k_A = 20exp\left(\frac{-15{,}100}{T}\right) \quad (5)$$

$$k_B = 4.46 \times 10^{-3} exp\left(\frac{-7{,}640}{T}\right) \quad (6)$$

$$k_T = 1.51 \times 10^{5} exp\left(\frac{-48{,}800}{T}\right) \quad (7)$$

$$k_z = 21.3exp\left(\frac{2{,}060}{T}\right) \quad (8)$$

where w is the specific reaction rate (kg/(m^2·s)), P_{O2} is the partial pressure of O_2, and T is the temperature at the onset of reaction. The parameter values for a sample calculation for C/Fe_2O_3 are given in Table 5.1. These calculations were performed for C/CuO, C/Fe_2O_3, and C/Bi_2O_3 at the respective initiation temperature from T-Jump/TOFMS at the highest heating rate. The values for the reaction rate and initiation temperature for each fuel/oxide system are given in Table 5.2. For each system, the reaction rate

predicted by the NSC model is at least four orders of magnitude slower than the experimentally predicted reaction rates. The higher reaction rate as determined from the experiment implies that the metal oxide proximity and nature of contact with the fuel will play a significant role. The condensed phase transport processes may also serve to enhance the diffusion of the oxidizer to increase the overall reaction rate.

Parameter for NSC model	**Value**
T	1020 K
P_{O2}	.21 atm
k_A	7.4×10^{-6} g·cm^{-2}·s^{-1}·atm^{-1}
k_B	2.5×10^{-6} g·cm^{-2}·s^{-1}·atm^{-1}
k_T	2.5×10^{-16} g·cm^{-2}·s^{-1}
k_z	161 atm^{-1}
χ	1
w	5.4×10^{-7} g·cm^{-2}·s^{-1}

Table 5.1: Sample parameters for the C/Fe_2O_3 system used to determine the reaction rate of carbon at 1020 K.

It is possible that some error exists in the NSC calculation as the two input parameters, temperature and pressure represent sources of uncertainty. For the C/Fe_2O_3, which undergoes an endothermic reaction if reaction (1) is followed, the temperature of

the wire is likely the highest possible temperature that oxidation takes place within this experiment. However, there is the possibility of self-heating during the exothermic C/CuO reaction. An estimated reaction temperature from CHEETAH 4.0 [97] equilibrium code (at constant volume) for stoichiometric C/CuO, yields a temperature of 1210 K. This value is ~200 K higher than the initiation temperature of C/CuO of 1010 K. The estimate from the NSC model for this elevated temperature is listed in Table 1 and is an order of magnitude higher at 1209 K, but is still ~3 orders of magnitude lower than the experimentally predicted reaction rate.

Sample	Temperature	NSC Estimated Reaction Rate	Estimated Reaction Rate from Experiments
C/Fe_2O_3	1020 K	5.6×10^{-7} g·cm^{-2}·s^{-1}	7×10^{-3} g·cm^{-2}·s^{-1}
C/Bi_2O_3	930 K	1.1×10^{-7} g·cm^{-2}·s^{-1}	2×10^{-2} g·cm^{-2}·s^{-1}
C/CuO	950 K	1.6×10^{-7} g·cm^{-2}·s^{-1}	1×10^{-2} g·cm^{-2}·s^{-1}
C/CuO	1209 K	7.7×10^{-6} g·cm^{-2}·s^{-1}	

Table 5.2: Estimated reaction rates using the NSC model and experimentally determined parameters.

The pressure for this system is difficult to assess. The experiments are performed under high vacuum conditions at 10^{-9} atm, but the reactions are also shown to proceed without the presence of a gas phase oxidizer. Due to the condensed nature of the reaction

it is challenging to predict an effective partial pressure for use in the model. Fortunately, the reaction rate is only lightly dependent on pressure. We have previously estimated the concentration of O_2 within a sample volume of fuel/metal oxide nanoparticles to be ~55 kg/m^3 [41] after complete release of the O_2 by the metal oxide. This value was used to determine the partial pressure of O_2 for each mixture at the temperatures given in Table 5.2.

A variable heating rate experiment was also performed to determine the apparent activation energy of the carbon oxidation process in each system. The temperature for the onset of CO_2 release for each system at several heating rates is given in Figure 5.4.

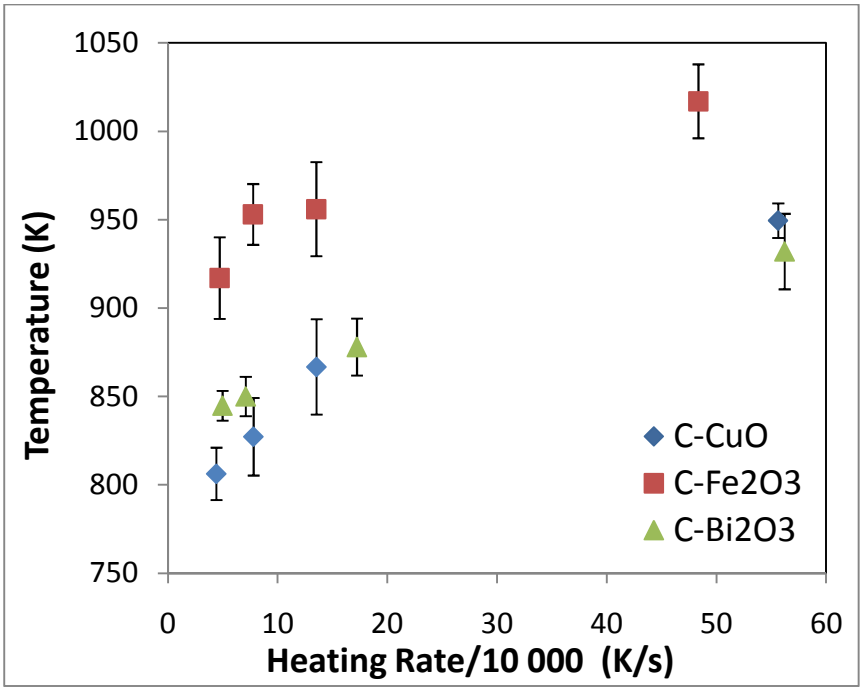

Figure 5.4: Decomposition temperatures taken from the onset of CO_2 production at various heating rates Each point is an averaged value from 4 experimental runs. Error bars represent the standard deviation.

Each point is an average of four experimental runs, and the error bars represent the standard deviation. The Osawa method [93, 94] can be used to determine the activation

energy from the slope of the Arrhenius plots in Figure 5.5. Initiation temperatures are in the range of 950 K to 810 K for C/CuO, 1020 K to 920 K for C/Fe_2O_3, and 930 K to 850 K for C/Bi_2O_3 producing activation energies of 97 ± 9 kJ/mol, 180 ± 21 kJ/mol, and 170 ± 15 kJ/mol, respectively. The error was determined using the standard error from similar un-averaged plots. These results are significantly lower than the activation energy at slow heating rates for CuO decomposition to produce a gaseous oxidizer,

$$CuO(s) \leftrightarrow Cu_2O(s) + O_2(g) \quad (9)$$

of 322.2 kJ/mol [98], but are consistent with O_2 release from CuO in recent high heating rate experiments [99]. Although the activation energy for the initiation of the fuel/metal oxide reaction is consistent with the gaseous O_2 release process, it does not necessarily mean that gas phase O_2 is required for initiation.

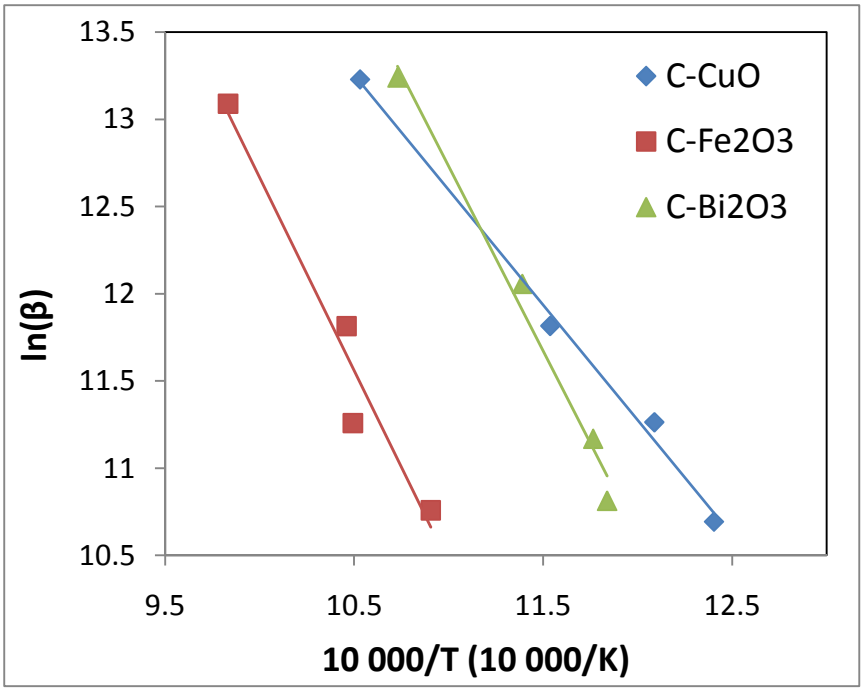

Figure 5.5: Arrhenius plots for the Ozawa isoconversion method. Each point is an averaged value from four experimental runs.

The presence of a condensed phase reaction in the C/CuO and C/Fe_2O_3 systems clearly demonstrates the ability of these metal oxides to oxidize a fuel through the condensed state. These results are consistent with those from Siriwardane *et al*. [85] who demonstrated a low temperature condensed state reaction with C/CuO. With respect to the aluminum/metal oxide reaction, T-Jump/TOFMS data showed that the ignition occurred for Al/CuO and Al/Fe_2O_3 at the point of gaseous O_2 release from the oxidizer [41]. At the point of gaseous oxidizer release, there are also other chemical changes occurring. As CuO releases O_2 we expect the formation of liquid Cu_2O, which may also serve as an oxidizing agent. A similar reaction is expected for Fe_2O_3 as liquid FeO may form upon O_2 release. The formation of these secondary metal oxides may help to promote condensed reaction, by enabling the metal oxide to flow around the carbon particle.

A slow heating-rate TEM study was also performed on C/CuO to observe the effect of low temperatures on the system. Figures 5.6 and 5.7 are the before and after images for heating at 500 K/min to 723 K. At this low temperature the extent of reaction is inconclusive, but it is clear that the CuO undergoes significant morphological changes despite the temperature being well below the bulk melting point of CuO at 1473 K. Siriwardane *et al.* observed similar changes for microscale C/CuO at 873 K [85]. These studies clearly show the mobility of metal oxides at temperatures well below their bulk melting points, and more in line with their Tammann[1] temperatures. The ability of the

[1] The Tammann temperature is usually considered as half of the bulk melting point of a material. This is the temperature at which surface atoms begin to gain a significant amount of mobility.76. Satterfield CN. *Heterogeneous catalysis in industrial practice. 2nd edition*; 1991.

metal oxide to become mobile and increase the effective surface area between fuel and oxidizer at low temperatures could be a key component of the initiation mechanism.

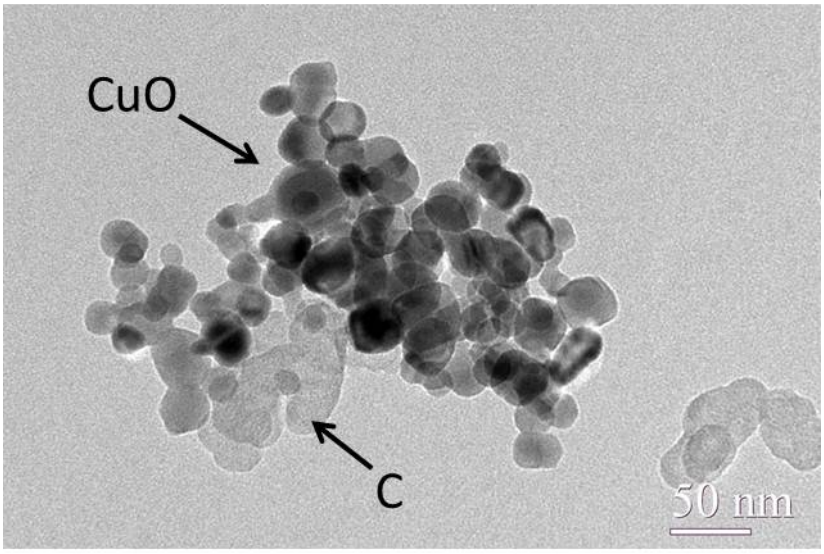

Figure 5.6: Before image for a heated TEM study for C/CuO. Samples were heated at ~500 K/min up to 723 K.

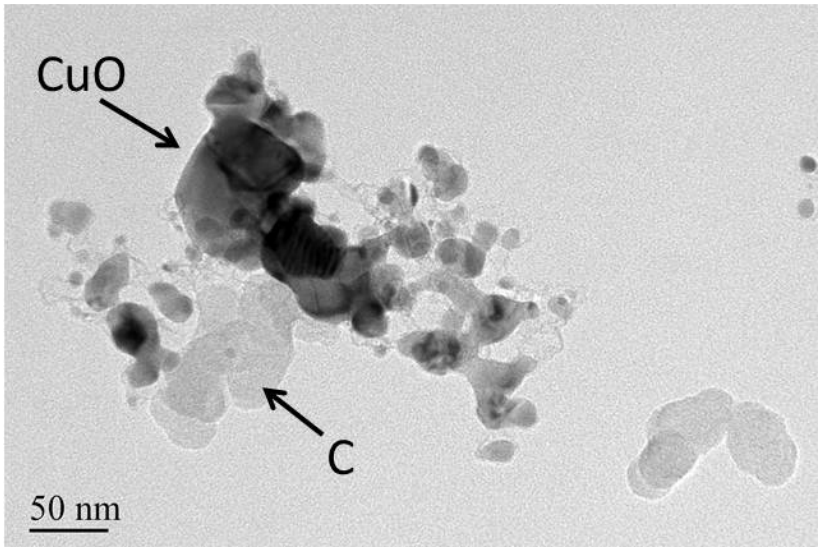

Figure 5.7: After image for a heated TEM study for C/CuO. Samples were heated at ~500 K/min, up to 723 K.

Thus far we have argued that in the current study, the initiation of carbon oxidation is largely dependent on the ability of the metal oxide to oxidize the fuel in the condensed state. Therefore the choice of metal oxide will affect many aspects of the reaction including the initiation temperature. We have noted the mechanistic similarities of a mixture of carbon and metal oxide nanoparticles with a nanothermite, but there is still an issue regarding the temperature of these reactions. If these systems are so alike mechanistically, then one would expect that the temperature which the carbon is oxidized in the present study would correspond to the aluminum/metal oxide ignition, but results show that they ignite at higher temperatures. This can be explained by the difference in the two fuels. Aluminum is surrounded by the relatively inert Al_2O_3 shell while carbon does not have such a protective shell. Once there is an oxidizing agent present for carbon, the fuel and oxidizer readily react. However for an aluminum fuel, once the oxidizer is present it is likely still separated from the aluminum metal by the Al_2O_3. Therefore, there will be some delay before the oxidizer and fuel come into contact. In a previous study we have seen the presence of ignition delays in nanothermites due to longer diffusion times from increased Al_2O_3 shell thickness [25]. These delays were as large as ~2 ms for a 4 nm Al_2O_3 shell. In the present study we predict the delay between the carbon combustion and that of the nanothermites to be ~.5 ms for CuO and ~1.25 ms for Fe_2O_3 based on the time difference from CO_2 release in the carbon/metal oxide and the release of O_2 from the neat metal oxide. This difference in delay for CuO and Fe_2O_3 further stresses that the ability of the oxide to transport O_2 in the condensed phase may play a large role in the speed of diffusion and hence the initiation process.

5.4. Conclusions

We have investigated the reaction of carbon/metal oxide mixtures using our T-Jump/TOFMS. To determine the order of reaction events we separately sampled the fuel/oxidizer as well as the neat nanopowders. Through the use of similar heating pulses for each experimental run we were able to determine the order that gaseous oxidizers were released from the metal oxides in comparison to when the carbon/metal oxide reacts. During initiation of both C/CuO and C/Fe_2O_3, CO_2 was the first gaseous reaction product that appeared. This initiation event clearly occurred before the gaseous O_2 production by neat metal oxides. Without the presence of a gaseous oxidizer at the point of initiation, we conclude that the initiation of the carbon combustion is due to a condensed phase reaction. Comparison with the NSC model suggests that the condensed phase reaction occurs at a much faster rate than traditional gas/solid heterogeneous reactions. We have compared this finding for carbon oxidation with that of our previous work with aluminum nanothermites, and have found some significant similarities. In both the Al/WO_3 high heating rate SEM, and the T-Jump x-ray imaging studies, there was significant evidence for a reactive sintering mechanism. The findings in the present study provide further evidence for this mechanism. There is one significant difference in the temperature of the oxidation between the aluminum and carbon in that the aluminum nanothermites react at a higher temperature. We attribute this apparent higher temperature, to a diffusion delay in aluminum combustion that is not present for carbon due to coating differences of the two fuels.

Chapter 6: Decomposition of Aminotetrazole Based Energetic Materials under High Heating Rate Conditions

As new energetic materials are being introduced, it is necessary to characterize and understand their reactions. The goal of this study is to investigate several different materials that have a common tetrazole substructure. Through this process it may be possible to obtain general information on how the tetrazole substructure breaks down based on the slight variations in molecular structure. Ideally this information could be considered during design of future energetic materials to predict how they would decompose even before formulation.

Chapter 6 Overview

The T-Jump/TOFMS is used to probe the decomposition of several aminotetrazole containing energetic materials under very high heating rates of 10^5-10^6 K/s. The materials investigated are 5-amino-1-methyl-1*H*-tetrazolium dinitramide (MeHAT_DN), 1,5-diamino-4-methyl-1*H*-tetrazolium dinitramide (MeDAT_DN), 1,5-diamino-1*H*-tetrazolium nitrate (DAT_N), 1,5-diamino-4-methyl-1*H*-tetrazolium azide (MeDAT_N3), and 5-aminotetrazolium dinitramide (HAT_DN). Subtle differences between materials in functional group placement and anion composition allow for further understanding of the decomposition pathway of the tetrazole structure and various anions. Two decomposition pathways for the tetrazole ring are observed, which result in the primary formation of HN_3 or N_2. The N_2 formation pathway occurs when functional groups are placed symmetrically around the tetrazole ring, while asymmetric placement

results in HN_3 production. The differing anion compositions also show effects on thermal stability of the salts as is demonstrated by lower decomposition temperature for the azide containing salt compared to the similar dinitramide containing material. For the decomposition of the dinitramide molecule, a high temperature (N_2O forming) and low temperature (NO_2 forming) decomposition pathway is observed as has been previously suggested.

6.1. Introduction

Recently, a shift has been made to create energetic materials (EMs) which are not only efficient performers, but also meet up to date safety and environmental standards. Current EMs such as RDX and HMX meet performance needs, but are sensitive to impact and friction, and possess an unwanted level of toxicity. These materials also produce environmentally harmful product species, which are largely due to carbon containing nitro groups [100]. So called "green energetic materials" (GEMs) are produced with concern towards environmental impact throughout the lifetime of a material. Many of these compounds contain a high-nitrogen content tetrazole sub-structure, which is paired with a functional anionic molecule to form stable energetic salts. These materials are unique in that their energy release comes primarily from the high heats of formation from their many nitrogen containing bonds [28]. The high-nitrogen content materials generally produce more environmentally friendly combustion products due to the diminished carbon containing product species. However, these materials are relatively new and have not been as extensively studied as more traditional

EM's. As such the decomposition products and reaction pathways are for the most part, still unknown.

Several groups have performed experimental and theoretical work to help understand the thermal decomposition of aminotetrazole containing materials [15, 28, 101-107]. Tools ranging from thermogravimetric analysis (TGA), differential scanning calorimetry (DSC), and FTIR/TOF mass spectrometry have been used, but traditionally these experiments are performed under low heating rates (10-100 K/min). Under rapid-heating conditions closer to that of a real-time combustion event, there will typically be a different set of dominant chemical processes. As a common sub-structure of many high-nitrogen content materials, 5-amino-*1H*-tetrazole and the breaking of the tetrazole ring, has been the focus of many studies. A temperature-jump/FTIR Spectroscopy system with a heating rate of 2000 K/s was used by Brill *et al.* to investigate the reaction pathways of aminotetrazole and a few of its related salts [105]. They identify two possible reaction pathways that vary with temperature; one which is dominant at low temperatures and consists of the breakdown of the ionic tetrazole structure, and one which is dominant at high temperatures and treats the aminotetrazole as a neutral. The main identifying products of these two pathways are HN_3 for the high temperature pathway and N_2 for the low temperature pathway. Theoretical work has been performed by Paul *et al.* on unimolecular 5-aminotetrazole decomposition [103]. Their studies also reveal two possible decomposition pathways for the tetrazole structure, which differs for aminotetrazole and its tautomer iminotetrazole. They predict that the main aminotetrazole reaction pathway will be that of N_2 extraction, while the main iminotetrazole pathway will produce HN_3.

Due to an extensive amount of relatively new high-nitrogen content energetic salts, few studies have examined the decomposition of these energetics, especially under rapid heating conditions. Chowdhury *et al.* used a confined rapid thermolysis technique to investigate the reactions of tetrazole based ionic liquids at heating rates of up to 2000 K/s. The main diagnostic tools for this study were FTIR spectroscopy and TOF spectrometry which obtained temporal resolutions of 50 ms and 1 ms, respectively [104]. They showed that positions of functional groups on the tetrazole ring play a significant role on the thermal stability and decomposition pathway of the tetrazole structure. Despite some rapid heating rate studies on tetrazole containing materials, to our knowledge none exist for the materials of this study. Slow heating rate DSC studies and mass spectrometry and IR spectroscopy have been performed by Fischer and co-workers for MeDAT_DN and MeDAT_N3 [107]. Their decomposition analysis for these materials will be used for comparison and breakdown of the reaction products in this investigation.

In a complementary study our group tested several energetic salts in a high heating rate μ-DSC experiment [108]. This study showed a significant decrease in activation energy for energetic materials at rapid heating rates, suggesting that different mechanistic processes are at play. In order to investigate the intermediate processes of a reaction, an experiment with very high heating and sampling rates is required. In this paper we employ a Temperature-Jump/Time-Of-Flight Mass Spectrometer to characterize the decomposition pathways of several aminotetrazole containing energetic salts. The uniqueness of this instrument is its ability to heat samples at very high heating rates of

10^5 - 10^6 K/s while simultaneously sampling the reaction products at a temporal resolution of 100 µs, which can allow for probing of the early stages of reaction.

6.2. Experimental

The primary experimental device is the T-Jump/TOFMS. Samples are received in a solution of ethanol or methanol, and are placed onto the sample probe by manually applying a drop of the solution to the platinum wire. This procedure allows for a quick coating of the sample, but typically results in a sparse, non-uniform coating. We have previously taken scanning electron microscope (SEM) images of filaments coated with nitrocellulose or RDX. These two materials were studied as their coatings under this process are very different from each other. Nitrocellulose can be thickly coated onto the wire, while RDX is sparse and non-uniform, more in-line with a typical sample. After a volume estimation and assuming the density of MeDAT_DN of 1.719 g/cm^3 [107], we predict larger samples to be ~10 µg and a typical sample ~1 µg.

Heating of the samples is performed under high vacuum conditions (10^{-7} torr). This allows for the probing of condensed phase decomposition reactions, as any gas phase reaction products will be ejected into the vacuum region. However, sampling of organic energetic materials under such conditions raises concern about evaporation prior to decomposition. For this reason energetic salts, which have negligible vapor pressures are studied. All samples used in this experiment are provided by T.M. Klapötke of Ludwig-Maximilians University in Munich, Germany, and consist of 5-amino-1-methyl-1*H*-tetrazolium dinitramide (MeHAT_DN), 1,5-diamino-4-methyl-1*H*-tetrazolium

dinitramide (MeDAT_DN), 1,5-diamino-1*H*-tetrazolium nitrate (DAT_N), 1,5-diamino-4-methyl-1*H*-tetrazolium azide (MeDAT_N3), and 5-aminotetrazolium dinitramide (HAT_DN) and the synthesis of each material is documented elsewhere [15, 26-28]. For sampling purposes, the filament is inserted into the high vacuum sampling region of the TOFMS within close proximity (~2 cm) to the ionization source, a 70 eV electron impact beam. This allows for reaction products to reach the MCP detector of the mass spectrometer at a fast time scale well below the characteristic time of the experiment. A typical heating run consists of a ~3 ms heating pulse which heats the filament up to ~1270 K or a rate of ~327,000 K/s. Throughout the heating of the sample, a mass spectrum is taken every 100 µs, and the current and voltage are simultaneously recorded to determine the temperature of the filament. Reported temperatures are that of the filament, determined from the variance of platinum resistivity with temperature [23]. Due to inconsistencies in the sample coating there are likely significant temperature gradients within the sample. However, heat transfer calculations suggest that the near surface portion of the sample follows the temperature of the filament closely.

6.3. Results and Discussion

The investigation of condensed phase reactions is a very difficult task. If we assume that our method of sampling within a vacuum eliminates secondary gas phase reactions, then we have eliminated part of the complexity of the analysis process. However, the condensed phase reactions themselves could be very intricate. Upon the initial breaking of a reactive molecule, the product could undergo thousands of collisions and numerous other reactive processes before exiting the condensed state. There is also

the possibility that the initial products of reaction survive the many collision events and exit the condensed state unscathed. Herein lies a great uncertainty for all experimental studies concerned with the determination of mechanistic information. It is very difficult to consider how to probe individual sub-nanosecond collision events, such as what may be at play for the condensed phase reactions. By eliminating gas phase reactions, this study moves closer to investigation of the initial bond breaking events of energetic materials. We acknowledge the possible complexities within the condensed state, but attempt to identify possible reaction pathways as suggested by our experimental studies.

Decomposition temperatures and reaction times for the six compounds were determined from mass spectrometer results at a heating rate of ~327,000 K/s and are tabulated in Table 6.1. The decomposition temperatures were taken from the onset of product species, and the reaction times were determined from the full-width half-max of the detected product species concentration.

Compound	Onset Decomposition Temperature (^{o}C)	Reaction Time (ms)	Reported Decomposition Temperature (^{o}C)
MeHAT_DN	201 ± 10	0.3	145 [28]
MeDAT_DN	303 ± 7	0.2	150 [107]
DAT_N	193 ± 14	0.5	168* [15]
MeDAT_N3	184 ± 7	0.4	137 [107]
HAT_DN	251 ± 7	0.7	117[26]

Table 6.1: Measured onset decomposition temperature and reaction time.

***** Temperature taken from the peak of a DSC trace

Previously reported temperatures of the onset of decomposition during slow heating rate (~10 ^{o}C/min) DSC experiments are also reported in Table 6.1. When subjected to very high heating rates, each material exhibits a higher decomposition temperature. This may be indicative of different reaction processes under these high heating rate conditions. In the following we explore the decomposition behavior of each compound. For reference, the two predicted reaction pathways for tetrazole ring decomposition are shown in **1→2** and **1→4**. The main reaction products that are representative of these two pathways are NH_2NCNH for **1→2** and HN_3 for **1→4**. Due to complex spectrometric analysis, each material will be discussed separately.

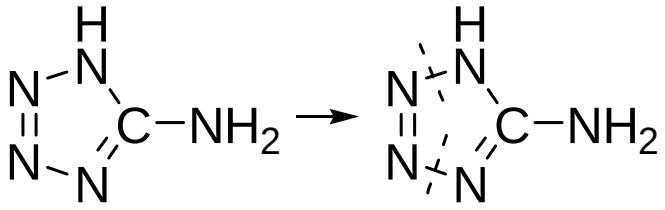

1 **2**

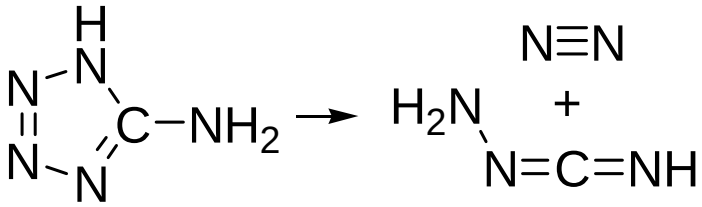

1 **3**

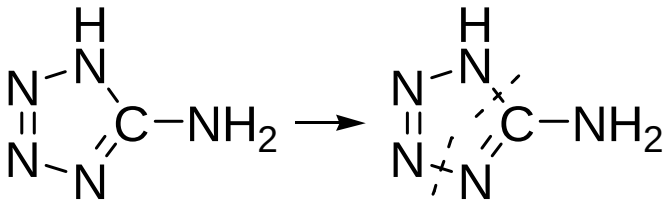

1 **4**

6.3.1. 5-aminotetrazolium dinitramide

The cation of 5-aminotetrazolium dinitramide (HAT_DN), **5**, contains the basic aminotetrazole structure and is paired with the dinitramide ($N_3O_4^-$) anion. Of the materials studied, this has the slowest reaction time (see Table 6.1), which allows for the capture of multiple steps within the reaction that may not be detectable for other materials.

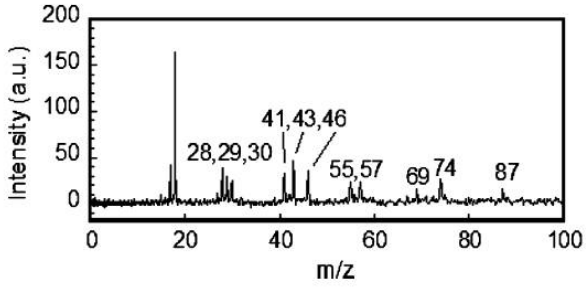

Figure 6.1: Detailed mass spectrum of the reaction products from heating for HAT_DN, 5.

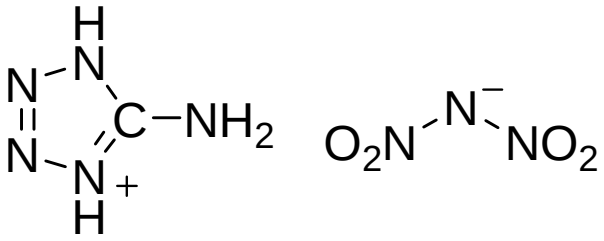

5

Figure 6.1 is a single detailed spectrum of the reaction products for **5.** With the significant amount of reaction products for HAT_DN it would be difficult, even with a complementary species identification study, to accurately identify each species and its origin, whether from fragmentation or decomposition. Therefore, we will only assume the identity of peaks that we can provide ample evidence as to their origin, and will note the uncertainty of other assignments. Table 6.2 lists the detected mass peaks for each

decomposition experiment, and also provides the possible methods of formation for each species.

Name	Abbreviation	Detected Product Species	Species Identification	Species Origin
5-aminotetrazolium dinitramide	HAT_DN	28 29 30 41 43 46 55 57 69 74 87	N_2 HN_2, CH_3N NO CHN_2 HN_3 NO_2 CHN_3 NH_2NCNH *na* N_3O_2 $HN_3HCN_2H_3$	EI EI Dinitramide Decomp./EI (NO_2) EI (m/z 87) Tetrazole Fracture Dinitramide Decomp. EI (m/z 87) Tetrazole Fracture/EI (m/z 87) EI (m/z 87) Dinitramide Decomp Partial Tetrazole Ring Split
5-amino-1-methyl-1*H*-tetrazolium dinitramide	MeHAT_DN	14 15 28 30 42 43 46	N CH_3 N_2 NO N_3 HN_3, $HNCNH_2$ NO_2	EI Methyl Group EI Dinitramide Decomp./EI (NO_2) Tetrazole Fracture Tetrazole Fracture Dinitramide Decomp.
1,5-diamino-4-methyl-1*H*-tetrazolium dinitramide	MeDAT_DN	14 15 16 28 29 30 44 46 55 57	N CH_3 CH_4 N_2 HN_2, CH_3N NO N_2O NO_2 CHN_3 NH_2NCNH	EI Methyl Group Methane Tetrazole Fracture/EI EI Dinitramide Decomp./EI (NO_2) Dinitramide Decomp. Dinitramide Decomp. Tetrazole Decomp/EI Tetrazole Fracture
1,5-diamino-4-methyl-1*H*-tetrazolium azide	MeDAT_N3	15 28 30 43 57	CH_3 N_2 - HN_3 NH_2NCNH	Methyl Group Tetrazole Fracture/EI - Azide Protonation Tetrazole Fracture
1,5-diamino-1*H*-tetrazolium nitrate	DAT_N	28 29 30 43 46	N_2 HN_2, CH_3N NO HN_3, $HNCNH_2$ NO_2	EI EI Dinitramide Decomp./EI (NO_2) Tetrazole Fracture Dinitramide Decomp.

Table 6.2: The detected spectral peaks during decomposition experiments. For each mass peak the origin of formation for the peak is denoted.

During peak assignment, we also assume that since this study is performed at rapid heating rates under high vacuum, that there are not substantial secondary reactions or re-combination within the condensed phase. This thought process, combined with comparison to previous studies in the literature allows for identification of critical reaction products unique to certain mechanisms.

As an example we consider the largest mass observed for HAT_DN, m/z 87, and we note that the cation of **5** has a molecular mass of 86. This m/z was not reported for the decomposition of tetrazole or dinitramide containing materials in the literature. Paul *et al.* suggests that there is an intermediate step in the reaction of the tetrazole structure where the ring first splits before N_2 is released as shown by **6** [103]. This work by Paul is a theoretical unimolecular decomposition study, so it is unable to predict intermolecular hydrogen exchange. We assume that with the ionic nature of this material there is some exchange of hydrogen atoms between molecules.

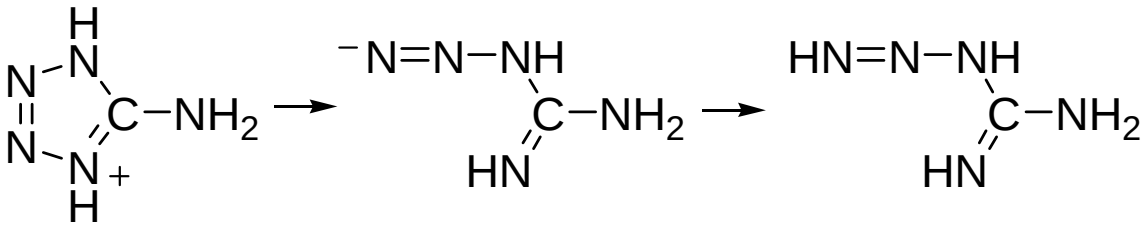

6 **7**

As the tetrazole ring splits apart by breaking an N-N bond, it is reasonable to assume that protonation of the open ring could occur to form a structure similar to **7** with m/z 87, which is consistent with our observation. This large and presumably unstable molecule would undergo significant fragmentation during ionization, which may account for many of the detected spectral peaks. However, there is a significant amount of uncertainty in

assigning ion fragment peaks to this molecule. Therefore focus will be lent to assigning values to peaks which presumably come from other sources. There are other possible molecular structures with m/z 87 such as CHN_3O_2, CH_3N_4O, C_2HNO_3. Each of these structures would require significant decomposition and recombination in the condensed state. We assume m/z 87 is due to the open ring tetrazole structure, shown in **7** due to the simplicity of its formation.

The other large molecule detected by our system, m/z 74, has not been previously reported in the literature as a decomposition product of tetrazole or dinitramide reactions, and may represent an intermediate step in the initial reaction process. This peak is not from fragmentation of **7** as this would require removal of a mass of 13 a.m.u. which is not feasible given the molecular structure. It is difficult to create m/z 74 from the tetrazole containing cation as it again requires significant recombination and intermixing with the anion or the addition of several hydrogen atoms. With a molecular mass of 106 the dinitramide molecule can form m/z 74 through the loss of 2 oxygen atoms. Examining the dinitramide structure **8** proposed by Bottaro *et al.* [109], we predict a loss of $2O^-$ to form N_3O_2. N_3O_2 has been experimentally observed in positive [110, 111] and negative [112] ionic forms, but to our knowledge, not as a neutral molecule.

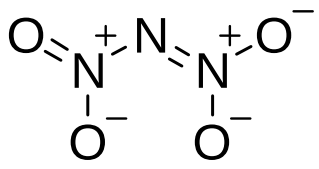

8

Although the neutral molecule has not been experimentally observed, theoretical work has shown that this formation is possible, but thermodynamically unstable [113].

Regardless of overall charge, there is evidence that N_3O_2 will decompose to NO and N_2O [114-116]. Figure 6.2 shows the temporal evolution of select product species pertaining to the decomposition of the dinitramide structure. The earliest species observed are m/z 74 and m/z 46, where m/z 46 represents NO_2, a common decomposition product of N_3O_4 containing compounds [109, 117], and later in the decomposition N_2O is observed. For HAT_DN decomposition, the formation of N_2O consistently forms at a higher temperature and later time than NO_2 and m/z 74. As a measure of consistency, analysis of five experimental runs gives an average time difference from the formation of NO_2 to the formation of N_2O of 0.3 ± 0.1ms.

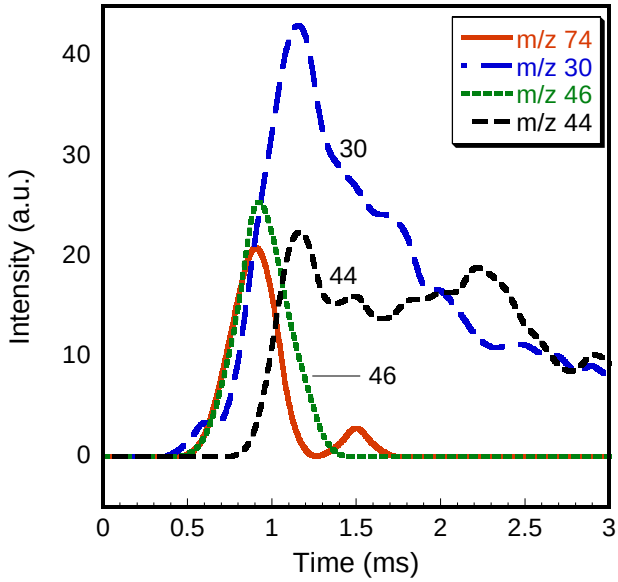

Figure 6.2: Detected product species during heating of HAT_DN, 5.

The presence of these different reaction products suggests that there may be competing mechanisms for decomposition. There have been previous reports of two mechanistic pathways for dinitramide breakdown in an ammonium dinitramide

compound [117-119]. The two pathways consist of a low temperature NO_2 forming pathway, and a high temperature N_2O forming pathway. These two mechanisms are consistent with what we observe, as NO_2 is present at a lower temperature, followed by the appearance of N_2O (m/z = 44) at a higher temperature. Analysis of these two pathways is a much more complex problem. While previous studies attribute N_2O formation as a single step process, we consider that there could be more processes at play. While m/z 46, 44, 30, can all be attributed to the dinitramide breakdown, m/z 30 also has contributions from fragmentation of other species. There are three main contributing sources to the detected NO concentration in HAT_DN decomposition, production of NO from the reaction itself as well as from fragmentation of N_2O and NO_2. There may also be a minor contribution to m/z 30 from fragmentation of m/z 57 via H_2N_2. Based on fragmentation patterns obtained using neat NO_2 and N_2O gas, we conclude that at low temperatures the majority of the NO is produced from NO_2 fragmentation, while at higher temperatures NO is also directly formed from the decomposition process. Since NO and N_2O are both produced at higher temperatures it is possible that this is due to N_3O_2 decomposition. It is also possible that N_2O is not produced directly from the dinitramide, but rather from decomposition of a reaction product from NO_2 production. Since NO_2 is produced early in the reaction process, a condensed state decomposition product of this step could be formed and further decomposed to produce N_2O. In the MeHAT_DN analysis below we observe NO_2 as a primary decomposition product, but only occasionally observe N_2O. This suggests that N_2O is a result of a higher temperature reaction mechanism, or secondary condensed

phase mechanism, rather than the decomposition of a primary reaction product from the NO_2 reaction step.

As with the dinitramide structure, there are multiple reaction pathways for the tetrazole molecule. The m/z ratios 43 and 57 represent the two different tetrazole breakdown mechanisms [102], and are noted as both being present in the spectrum for decomposition. However, due to the presence of larger molecules and fragmentation of these molecules, a decisive conclusion cannot be made as to how the tetrazole ring breaks down during HAT_DN decomposition.

6.3.2. 1,5-diamino-4-methyl-1H-tetrazolium dinitramide

The structure for MeDAT_DN is given in **9**. This structure is similar to HAT_DN in that it is a tetrazole containing cation paired with a dinitramide anion. The cation does have some slight variations as it has two functional groups, an amino and methyl group, symmetrically placed on the tetrazole ring. These small differences have a significant impact on the decomposition of the tetrazole ring as seen in Figure 6.3.

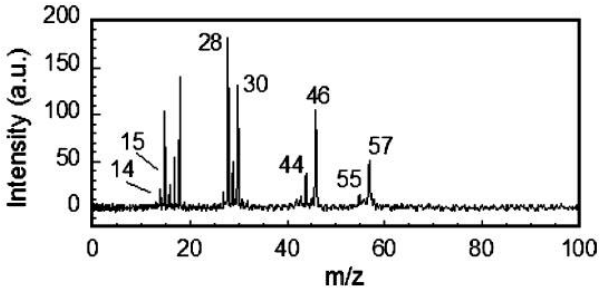

Figure 6.3: Detailed mass spectrum of the reaction products from heating of MeDAT_DN, 9.

This decomposition follows that of the tetrazole ring as demonstrated in **2**, and is consistent with the N_2 extraction mechanism seen in previous studies. As noted, this

mechanism will produce a peak at 57 and an intense peak at 28 and for MeDAT_DN this involves the removal of the functional groups from the tetrazole structure, which can be confirmed from the presence of m/z 15, CH_3, while the amino group may be further protonated to form ammonia (NH_3, m/z 17). With the loss of both functional groups, the remaining structure would have a net negative charge, and would likely undergo protonation before splitting to m/z 28 and 57.

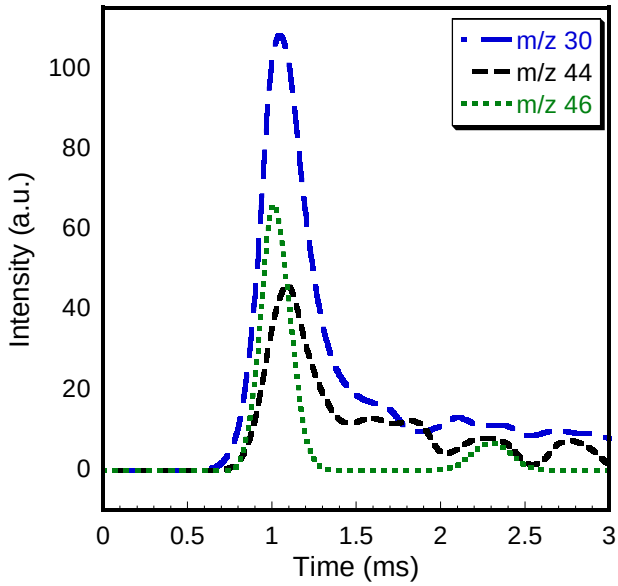

Figure 6.4: Detected product species during heating of MeDAT_DN, 9.

For the dinitramide anion we see the production of both N_2O and NO_2 suggesting a similar decomposition mechanism as that of HAT_DN. . One main difference in the decomposition between this molecule and the HAT_DN molecule is that this reaction occurs much faster. If we take the full-width half max of the detected product species as a representative reaction time for both reactions, **9** reacts 2-3 times faster than **5**. With the decomposition of **5** we were able to observe multiple steps in the reaction where NO_2

appears prior to N_2O. In the decomposition of **9** the reaction happens at a much faster rate and NO_2 and N_2O appear simultaneously and relatively early. However, it can be seen in Figure 6.4 that N_2O production does peak later than NO_2. If we compare the decomposition temperature of the three dinitramide containing materials in Table 6.1 with their reaction products, we observe that N_2O is observed in MeDAT_DN, and HAT_DN, with decomposition temperatures 303 ^oC and 251 ^oC respectively. However, N_2O is not typically observed in the decomposition of MeHAT_DN, which has the lowest decomposition temperature of 201 ^oC. This evidence further confirms the previous assumptions of a high and low temperature decomposition mechanism for the dinitramide molecule.

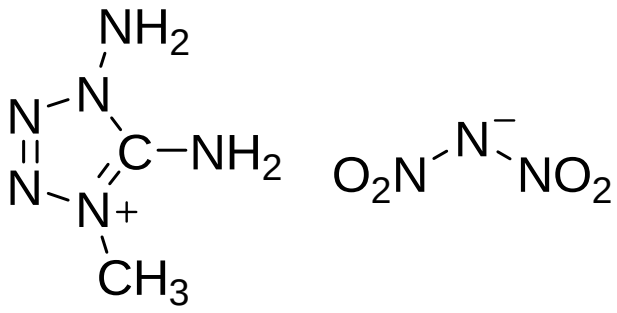

9

Although we have assigned species to each spectral peak, there is still some vagueness as to whether these peaks are directly due to decomposition, or whether they are from fragmentation of a larger molecule. Typically additional experiments are needed for comparison, in this case a slow heating rate experiment using mass spectrometry with 70 eV electron impact source and FT-IR spectroscopy has been previously performed for MeDAT_DN by Fischer and co-workers [107]. The gas phase decomposition products were investigated at a 4 ^oC/min heating rate, and from the

reaction products they predict that the tetrazole ring decomposes to form HN_3 as in **4**, rather than forming N_2 as our results suggest. More importantly this previous experiment allows us to determine whether some of the reaction products of this study are due to fragmentation or decomposition. The Fischer work does observe some larger molecules that undergo significant fragmentation during ionization. The main decomposition products are N_2O (m/z 44), MeN_3 (m/z 57), $MeONO_2$ (m/z 75, mass peak not observed, authors assume fragmentation), $(HCN)_3$ (m/z 81), HCN (m/z 27), NH_3 (m/z 17), and H_2O (m/z 18). Comparing our study to these results, we conclude that m/z 57 is due to NH_2NCNH, not MeN_3. In the Fischer study they confirm the presence of MeN_3 with FT-IR spectroscopy, and observe a m/z 57 peak with their mass spectrometer. However, they do not observe a peak at m/z 15 for the methyl group as we do. Since both studies use a 70 eV electron impact source, this confirms that our CH_3 peak is not due to fragmentation of MeN_3, and further suggests that m/z 57 is not due to MeN_3 as the methyl group is occupied elsewhere. The Fischer study also detects $MeONO_2$ with FT-IR spectroscopy, however this does not fragment to produce an NO_2 (m/z 46) peak, which we do detect. This clearly demonstrates that NO_2 is a result from a different breakdown mechanism that does not produce $MeONO_2$. Our study also does not identify any of the larger product species that are detected in the previous study. Due to this evidence it is highly unlikely that the primary reaction products in the current study are due to fragmentation of larger molecules.

6.3.3. 5 -amino-1-methyl-1H-tetrazolium dinitramide

The structure for MeHAT_DN is shown in **10** and a decomposition spectrum is shown in Figure 6.5. This structure is very similar to **5** except one hydrogen atom on the tetrazole ring is replaced with a methyl group.

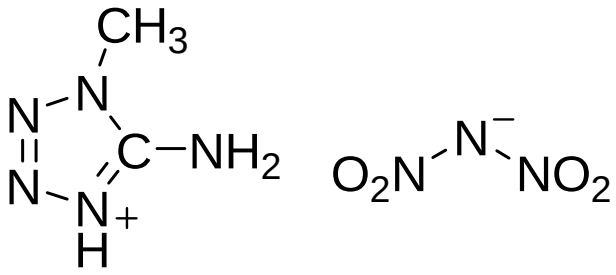

10

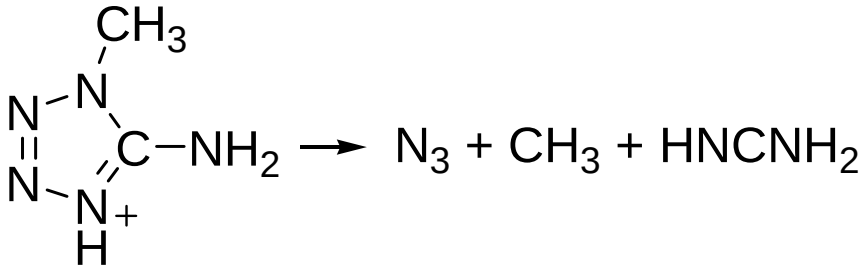

11

Comparison of this decomposition with that of HAT_DN, and MeDAT_DN shows there is no peak at m/z 57. This suggests that the addition of the methyl group has a significant impact on the decomposition of the tetrazole ring and implies some other reaction pathway. With the presence of m/z 43 we consider the pathway in **4**, which should lead to $HNCNH_2$ and CH_3N_3. CH_3N_3 has a m/z of 57, however we have already demonstrated the tendency of the methyl group to break off during decomposition, which leaves a

remaining N_3 molecule with a net negative charge that can be further protonated to form HN_3. We again observe m/z 15 corresponding to CH_3, but there is no study on MeHAT_DN for direct comparison. However from the above discussion on MeDAT_DN, it can safely be concluded that the CH_3 molecule is a direct result of the reaction.

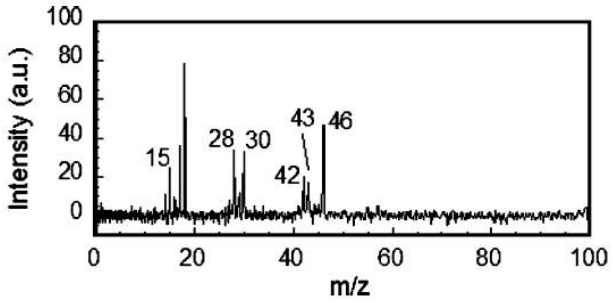

Figure 6.5: Detailed mass spectrum of the reaction products from heating of MeHAT_DN, 10.

The products due to the reaction of the tetrazole structure following this mechanism are given in **11**. As mentioned previously, for both the dinitramide and tetrazole structures there are at least two possible breakdown mechanisms. The addition of the methyl group to the tetrazole ring changes the breakdown mechanism to form HN_3 rather than the N_2 and NH_2NCNH as is seen for MeDAT_DN. For the dinitramide decomposition in HAT_DN and MeDAT_DN we assumed a high temperature N_2O forming route, and a low temperature NO_2 forming route. In a typical experimental run, N_2O is not observed as a decomposition product as MeHAT_DN starts to decompose at a lower temperature than either HAT_DN or MeDAT_DN, and likely completes reaction before the high temperature reaction begins. In a few instances N_2O was observed late in the reaction of MeHAT_DN. These cases were of larger sample sizes, which either

allows for longer residence times on the wire, allowing for heating at higher temperatures, or secondary condensed phase reactions. We attribute the presence of N_2O to the longer residence time on the wire which allows for the sample to remain on the wire at higher temperatures. This evidence should eliminate the theory that N_2O is the result of decomposition of a secondary product of NO_2 production as previously suggested. Since we are able to observe NO_2 in all cases, if a product of this reaction yields N_2O, it would happen in all cases.

6.3.4. 1,5-diamino-4-methyl-1H-tetrazolium azide

Aside from dinitramide containing salts, we also investigated the tetrazole containing cations with various other anions. The spectrum for MeDAT_N3, **12**, is shown in Figure 6.6.

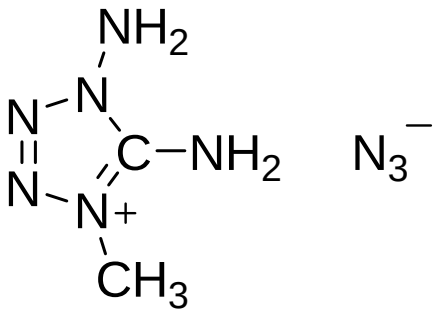

12

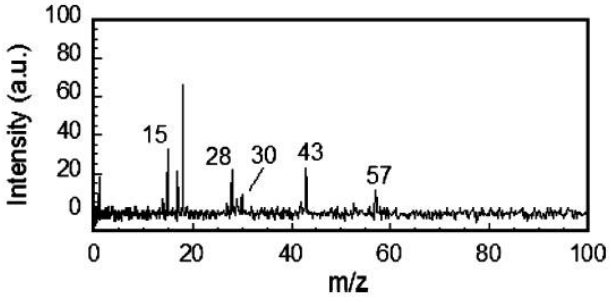

Figure 6.6: Detailed mass spectrum of the reaction products from heating of MeDAT_N3, 12.

The decomposition for this material is similar to what was seen for **9**. We see the evidence of the nitrogen expulsion mechanism with peaks at m/z 57 and 28. Peak 43 in this case can be attributed to the protonated azide structure HN_3. When comparing this material with MeDAT_DN we would expect MeDAT_N3 to show a lower thermal stability [15]. This appears to be the case as we see decomposition temperatures of 303 ^oC and 184 ^oC for MeDAT_DN and MeDAT_N3, respectively. The work by Fischer also examined the gas phase decomposition products of MeDAT_N3. The main reaction products detected in their study are HN_3 (m/z 43), HCN (m/z 27), CH_3N_3 (m/z 57), NH_4N_3 (m/z 60) and N_2 (m/z 28) [107]. While we observe most of these m/z's in our spectra, we attribute the products to different processes. They believe that HN_3 is produced from the breaking of the tetrazole ring as in **4** rather than from the azide anion. As is the case for MeDAT_DN, we do not believe that CH_3N_3 is present for MeDAT_N3 due to the large presence of CH_3 in our spectra. It appears that CH_3 breaks off of the tetrazole ring easily and relatively early. We attribute the peak at m/z 57 to NH_2NCNH following the mechanisms for other materials in this study. Fischer also notes the presence of some larger molecules, $(H_2NCN)_3$ (m/z 126), and 1,2,4 Triazole (m/z 69), neither of which are present in our study.

6.3.5. 1,5-diamino-1H-tetrazolium nitrate

The structure for DAT_N is shown in **13**. This material is slightly different from the other tetrazoles examined as it is a diaminotetrazolium cation without a methyl group and is also paired with a nitrate anion. From examination of the breakdown mechanisms

of each of the other materials, there appears to be a trend in how the tetrazole molecule will break apart based on the placement of the functional groups around the outside of the tetrazole ring. Molecules **9** and **12** both have functional groups symmetrically placed around the tetrazole structure, whereas **10** has the methyl group on one side of the ring. The decomposition of the tetrazole ring for **9** and **12** follow the same pattern of N_2 expulsion, and molecule **10** produces HN_3. Following this logic, DAT_N will decompose in a similar fashion as structure **10** to produce HN_3. From Figure 6.7 this mechanism is confirmed as there is a large peak at m/z 43 representing HN_3, and the absence of species representative of the N_2 expulsion mechanism, mainly peak 57.

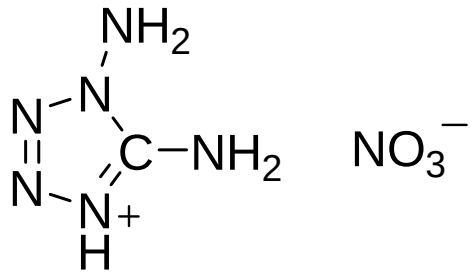

13

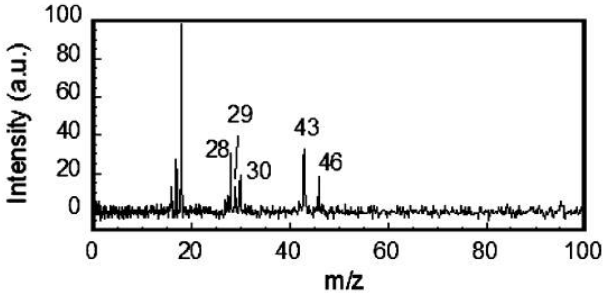

Figure 6.7: Detailed mass spectrum of the reaction products from heating of DAT_N, 13.

We also observe peaks at m/z 46 and 30 which can be attributed to NO_2 formation from the nitrate anion. A slow heating rate DSC study was previously performed on a similar

material 5-aminotetrazolium nitrate [101]. Using FT-IR spectroscopy the authors suggest that the material protonizes the NO_3 anion to form HNO_3 and this decomposes to form H_2O and NO_2 gas, while the tetrazole decomposes via the HN_3 mechanism. This is very consistent with our results for DAT_N at high heating rates. The correlation of these two experiments suggests that protonation of the anion may occur before decomposition. This, combined with other instances of protonation for the previous materials, strongly suggests that proton transfer readily occurs during heating of ionic salts.

6.4. Conclusions

Using a T-Jump/TOFMS we have studied the thermal decomposition of several tetrazole containing energetic salts under conditions that minimize secondary gas phase reaction. By examining several different variations to the cation structure, we were able to draw some conclusions about the decomposition pathways of the tetrazole ring. Despite some uncertainty in the origin of every detected spectral peak, whether it comes from fragmentation or decomposition, we were able to identify reaction products that are representative of different mechanistic pathways of tetrazole decomposition. It is clear that there are two different reaction pathways demonstrated for the tetrazole ring in this work. Both pathways decompose through a breaking of the tetrazole ring, one with the expulsion of molecular nitrogen, the other producing HN_3. There is not significant evidence in this study to suggest that the reaction pathways played a major role in the decomposition temperature of the materials, however there is correlation between the placement and composition of functional groups and the breakdown of the tetrazole ring. Symmetrically placed functional groups such as the MeDAT containing salts

decomposed via the N_2 decomposition, while the others showed characteristics of the HN_3 mode. A high and low temperature decomposition pathway is observed for the dinitramide anion, as dinitramide containing materials that exhibited higher decomposition temperatures, produced N_2O at these high temperatures. Although there are limited studies on these energetic salts available for direct comparison, we did observe differences from previous work on MeDAT_DN and MeDAT_N3. These differences, mainly the presence of larger molecules in the reaction products, are likely due to the presence of secondary reactions in previous studies.

Chapter 7: Rapid-Heating of Energetic Materials Using a Micro-Differential Scanning Calorimeter

The work on GEMs with the T-Jump/TOFMS suggests that there may be different reactive processes occurring under rapid heating conditions. To further support this, a complementary study is required. This μ-DSC offers a separate experimental study capable of heating rates that are comparable to that of the T-Jump/TOFMS. Traditional DSC is commonly used to investigate the thermal stability of energetic materials, so the basic concepts are well understood. The μ-DSC does offer a very unique opportunity to perform multiple high heating rate experiments and extract activation energies for each material. Comparison of these values with those from the literature can provide more information on the reactions at high heating rates.

Chapter 7 Overview

A micro-Differential Scanning Calorimeter (μ-DSC) was employed to study the thermal decomposition of organic energetic materials. Heating rates from 1900 to 65,000 K/s were explored, which are many orders of magnitude higher than traditional DSC, but much closer to the conditions these materials would experience in their application. Temperature calibration was done by heating Sn, KNO_3, and $KClO_4$ at the desired heating rates to determine the temperature profile at each rate. The samples studied were 5-amino-1*H*-tetrazole, 5-amino-1-methyl-1*H*-tetrazolium dinitramide, 1,5-diamino-4-methyl-1*H*-tetrazolium dinitramide, and 1,5-diamino-4-methyl-1*H*-tetrazolium azide, which comprise a new class of high-nitrogen containing energetic materials. Activation energies determined through the Kissinger method are much lower than those reported

for the same materials under low heating rates. This indicates that other decomposition mechanisms may be at play under high heating rates.

7.1. Introduction

Differential scanning calorimetry (DSC) is often used as a characterization technique to determine the thermal behavior of energetic materials (EMs). As new organic EMs are formulated, this is an important test to determine thermal stability and ignition temperature. Recently, new organic energetic materials are being created to not only improve performance and stability, but also to reduce their environmental impact. These "green" energetics are generally high-nitrogen content ionic salts which have N_2 gas as a primary reaction product and create the majority of their energy from high heats of formation. Conversely, classic organic explosives (TNT, RDX, etc.) create energy through oxidation of a carbon backbone [120], which often results in gaseous carbon containing reaction products.. Many ionic salts have a tetrazole-containing cation, which is primarily responsible for the high-nitrogen content of the material. Two common cation structures are 5-amino-1H-tetrazole, and 1,5-diaminotetrazole which have 82.3 wt.% and 84 wt.% nitrogen respectively [102], while the anion can be composed of a variety of different structures.

Several groups have characterized high-nitrogen energetics via DSC and related experiments. 5-aminotetrazolium nitrate [101], 1,5-diamino-4-methyl-1*H*-tetrazolium nitrate [107], 1,5-diamino-4-methyl-1*H*-tetrazolium dinitramide [107], 1,5-diamino-4-methyl-1*H*-tetrazolium azide [107], and 5-aminotetrazolium dinitramide [26], are just a few examples of ionic salts that have been characterized by standard DSC methods. In

addition to decomposition temperature, activation energy can be calculated using varied heating rate experiments and either an isoconversion technique like that by Ozawa [93] or the Kissinger method [121]. Ma *et al.* performed this experiment for 5-aminotetrazolium nitrate from (2 to 25) K/min and obtained an activation energy of 303.2 kJ/mol using the Ozawa method and 311.0 kJ/mol using the Kissinger method [101]. In a similar DSC experiment at heating rates of (2 to 40) K/min, Fischer *et al.* determined the activation energy of several ionic salts and found them to be in the range of ~(101 to 138) kJ/mol using both the Ozawa and Kissinger methods [107]. Relative to heating rates commonly experienced during combustion of energetic materials, traditional DSC heating rates are many orders of magnitude lower. This is relevant as higher heating rates may lead to different mechanistic steps in the reaction. For example, it is established that as the heating rate increases, the activation energy tends to decrease. Heating experiments for $Ge_2Sb_2Te_5$ films showed the activation energy for film crystallization decreased by more than a factor of four over a heating rate range of (3 to 500) K/min.

To achieve very high heating rates that approach those that are relevant to energetic materials, new classes of DSC devices are necessary. These new devices based on MEMS fabrication methods offer very fast response due to the small thermal mass of both the heaters sample [122-125]. A μ-DSC device previously developed at the National Institute of Standards and Technology (NIST) is capable of heating rates up to $1x10^7$ K/s [125], and was previously used to explore phase changes in Ni/Si thin films [126]. This device is used to investigate the decomposition temperature and activation energy of several high-nitrogen energetic salts and results are compared with that of traditional DSC.

7.2. Experimental

The main diagnostic tool in this study is a silicon based µ-DSC device [125] (66 x 240 x 3.3 µm) shown in Figure 7.1, where the center rectangular section is the heated platform. The heated platform can be split through the vertical axis into two halves; one holds the sample and the other serves as a reference during heating. Each section has a poly-silicon heater, which is driven by a function generator (Tabor Electronics WS8102) [127] that supplies a linear voltage ramp. An aluminum poly-silicon thermopile consisting of a series of twelve junctions, located sequentially on opposite ends of the device, produces a voltage proportional to the temperature difference between the two sections. Heating rates are varied by adjusting the frequency of the function generator, and for these experiments the heating rates range from ~(1900 to 64,000) K/s.

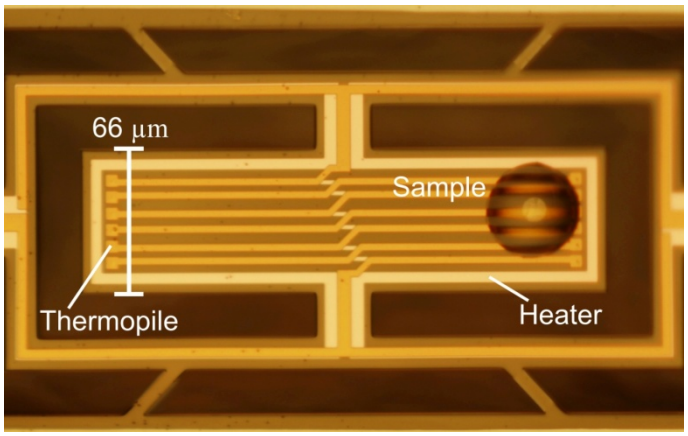

Figure 7.1: Image of the µ-DSC with a droplet of an organic energetic sample.

Samples are placed onto the surface of the µ-DSC using a PV820 Pneumatic Pico-pump system (World Precision Instruments) capable of producing picoliter sized drops. Droplet size is typically on the order of 10's of micrometers in diameter. The picopump

works by applying a short (5 ms) pressure burst to the liquid in the micropipette, ejecting a droplet from the tip. Drop sizes are determined optically from images such as Figure 7.1, and ranged from ~10 µm to 60 µm in diameter. Each sample is initially placed in either ethanol or methanol at a concentration of ~100mg/ml to maintain stability of the material. Samples are then diluted with H_2O to a concentration of ~10 mg/ml to prevent drying in the micropipette. The volume of the drop is estimated by assuming that wetting of the surface occurs in a similar fashion to a drop of water on a silicon surface. The contact angle of the drop is taken to be 30^o [128] and the curvature of the drop is assumed to be similar to a spherical cap [129]. Assuming the diameter of the drop as viewed in Figure 7.1 to be 60 µm the mass of sample is estimated to be 0.1 ng.

All organic energetic materials used in this experiment were provided by T.M. Klapötke of Ludwig-Maximilians University in Munich, Germany. The materials are 5-amino-1*H*-tetrazole (5-AT), 5-amino-1-methyl-1*H*-tetrazolium dinitramide (MeHAT_DN), 1,5-diamino-4-methyl-1*H*-tetrazolium dinitramide (MeDAT_DN), and 1,5-diamino-4-methyl-1*H*-tetrazolium azide (MeDAT_N3). The synthesis of each material has been documented elsewhere with the exception of 5-aminotetrazole which was acquired from Sigma-Aldrich [15, 26-28]. Aside from 5-AT, these materials are novel energetics and have been recently formulated, therefore a limited amount of diagnostic information is available.

Linear voltage ramps are used to drive the heaters and approximate a linear temperature ramp for the sample. Calibration was performed to confirm the temperature of the heating surface using three samples with well documented phase change points, tin (Sn), potassium perchlorate ($KClO_4$), and potassium nitrate (KNO_3), which has two

calibration points. The known calibration points are the melting point of tin at 505.1 K [130], a solid-solid phase transition for $KClO_4$ at 572 K [131], a KNO_3 solid-solid phase transition at 401 K [131, 132], and melting at 607 K [133]. With the known thermal properties of each material, four heating rates are applied, ~1900 K/s, ~6500 K/s, ~33,000 K/s, and ~64,000 K/s. For each material the voltage point at the onset of melting was measured and plotted in Figure 7.2. A linear function was created to convert voltage to temperature for each heating rate, the results of which are also shown in Figure 7.2. To achieve a desired temperature and ramp rate, the voltage and ramp duration are determined and applied for each heating rate. Due to the method of calibration, and very small sample sizes, we do not expect thermal lag or sample self-heating to be an issue with this system.

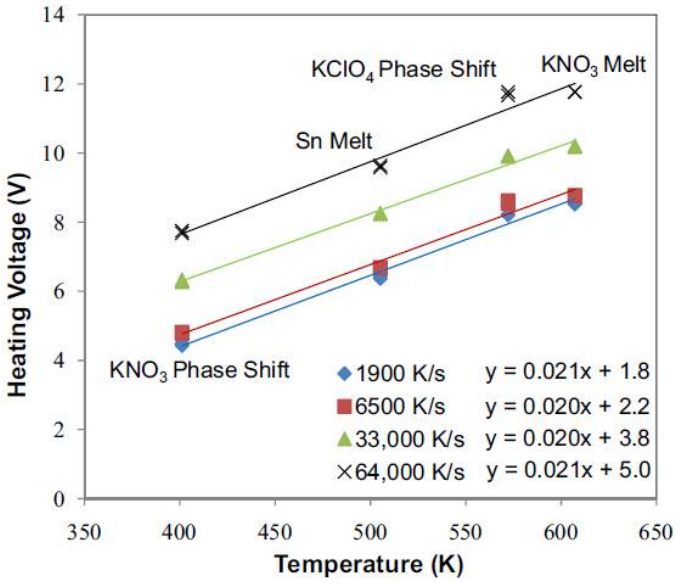

Figure 7.2: Voltage to temperature calibration for reference thermal signatures, melting point of tin, 505 K, solid-solid phase transition of $KClO_4$, 572.2 K, solid-solid phase transition of KNO_3, 401.2 K, and melting point of KNO_3, 607.1 K.

7.3. Results and Discussion

The decomposition temperature of each material at four different heating rates is shown in Figure 7.3. The error bars in this figure represent the standard deviation of each temperature point. We expect that the primary error in this experiment is due to either inconsistencies in drop size and placement, or non-uniformities in the heating surface's temperature profile. Either of these issues would cause slight variations in sample temperature throughout the experiment. Another minor source of error is due to assignment of decomposition temperature due to the breadth of the peaks.

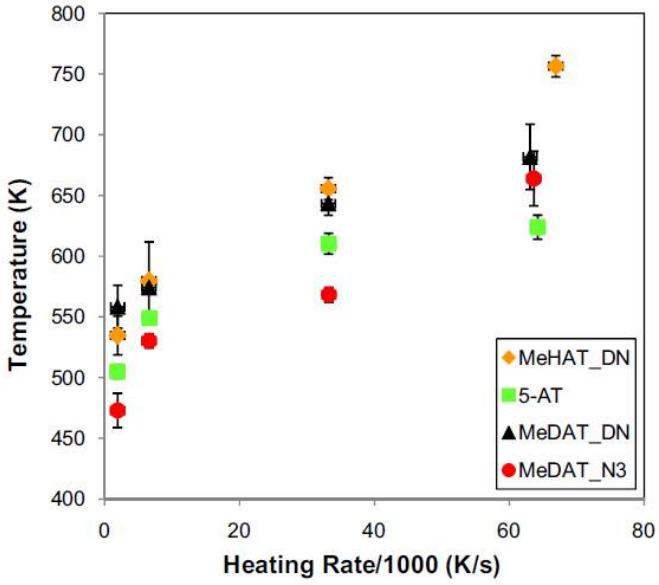

Figure 7.3: Decomposition temperature of various materials at four different heating rates.

In varied heating rate experiments it is possible to extract kinetic parameters using the Kissinger method [121],

$$\ln\left(\frac{\beta_i}{T_{p,i}^2}\right) = \text{constant} - \frac{\mathrm{E_a}}{\mathrm{R}T_{p,i}} \qquad (1)$$

where β is the heating rate, T_p is the temperature where the calorimetric trace peaks, and R is the gas constant. Figure 7.4 plots the left side of equation (1) versus the inverse of the decomposition temperature for each material so that the slope of the data is proportional to the activation energy. Following the Kissinger method, the decomposition temperature is taken from the peak of the calorimetric trace. For each data point in this figure, the average peak temperature and heating rate from several experimental runs is used for the Kissinger method. The materials in Figure 7.4 demonstrate an acceptable degree of linearity, as each sample has a correlation coefficient of 0.95 or greater. Table 1 lists the calculated activation energy with respective error for each material. To calculate the activation energy uncertainty we used Kissinger plots containing each individual data point per sample. Assuming a 95% confidence interval, the uncertainty in the slope of these plots was determined, and then multiplied by R to determine the maximum and minimum activation energy.

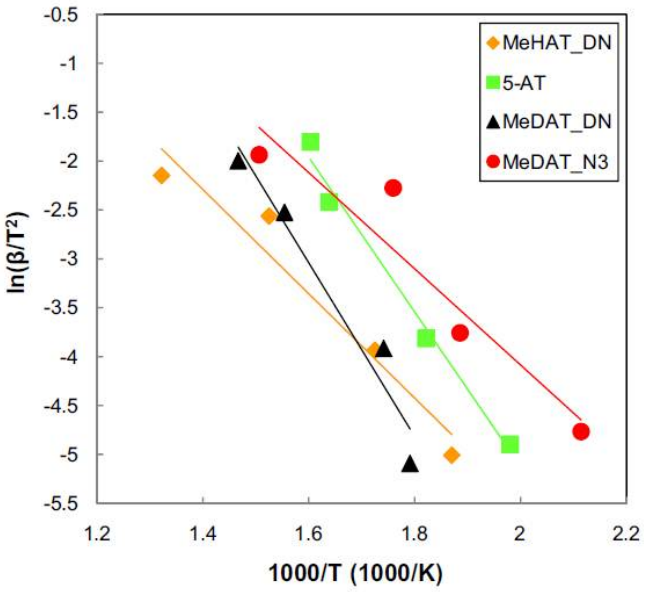

Figure 7.4: Kissinger plots for each sample.

As previously mentioned, most of these materials are synthesized by the Klapötke group at Ludwig-Maximilian University of Munich. Aside from synthesis, this group executes a variety of performance tests on these materials; therefore much of the work presented here is compared with their slow heating experiments. Since these materials show differences in their dependence on heating rate, each will be discussed separately.

Material	**E_a (kJ mol^{-1})**
MeDAT_DN	74 ± 14
MeDAT_N3	41 ± 13
5-AT	66 ± 10
MeHAT_DN	44 ± 6.1

Table 7.1: Activation energies for each material calculated using the Kissinger Method.

7.3.1. MeDAT_DN

A sample DSC trace for MeDAT_DN displaying a strong exothermic peak is shown in Figure 7.5a. This is consistent with traditional DSC experiments, which also show a strong exotherm. In this low heating rate study by Fischer, the decomposition peak shifted from (450 to 488) K for a (2 to 40) K/min heating rate range [107]. Figure 7.3 shows the variance in temperature of the exothermic peak for MeDAT_DN in the high heating rate µ-DSC experiments, which occurs in the range of (558 to 682) K. The elevated decomposition temperature in our experiments is a result of the use of high heating rates. Traditional DSC experiments also indicate a melting point at 358 K. While a sharp endotherm is not observed with the µ-DSC, a shallow broad endotherm is

present, and likely represents melting. Through the Kissinger method we calculate the activation energy to be ~74 kJ/mol, close to half of the ~138 kJ/mol calculated by Fischer *et al*. through both the Ozawa and Kissinger methods [107]. The uncertainty in activation energy of 14 kJ mol^{-1} for MeDAT_DN is relatively high compared to traditional DSC experiments. Even with this uncertainty, it is still clear that the activation energy is much lower than previous values, indicating the probing of different mechanistic events.

7.3.2. MeDAT_N3

MeDAT_N3 is reported to show an endothermic peak in the range of (458 to 484) K for various low heating rates, and has a reported melting point of 408 K [107]. In Figure 7.5b a large endothermic peak is observed for this material, which is consistent with the low heating rate work [107]. In the μ-DSC experiment the peak of the decomposition ranges from (473 to 664) K, and the activation energy is calculated to be ~41 kJ/mol, compared to 107 kJ/mol in the Fischer study. The main difference between the high and low heating-rate calorimetric traces is that the high heating rate study displays a very broad endotherm, compared to a sharp peak for the low heating rate Fischer study. We believe this endotherm is a result of both sublimation and decomposition, which at lower heating rates is observed as two endothermic peaks. Aside from heating rate, the main experimental variation between the Fischer work and the present study is that their experiment was performed in a semi-enclosed container with a 1 μm hole in the top, and the present work was done in an open environment. Fischer and co-workers mention that if a completely closed container is used then the two

endotherms become one. In our μ-DSC experiment, the heating rate may be at a point that the sublimation and decomposition also occur as one process.

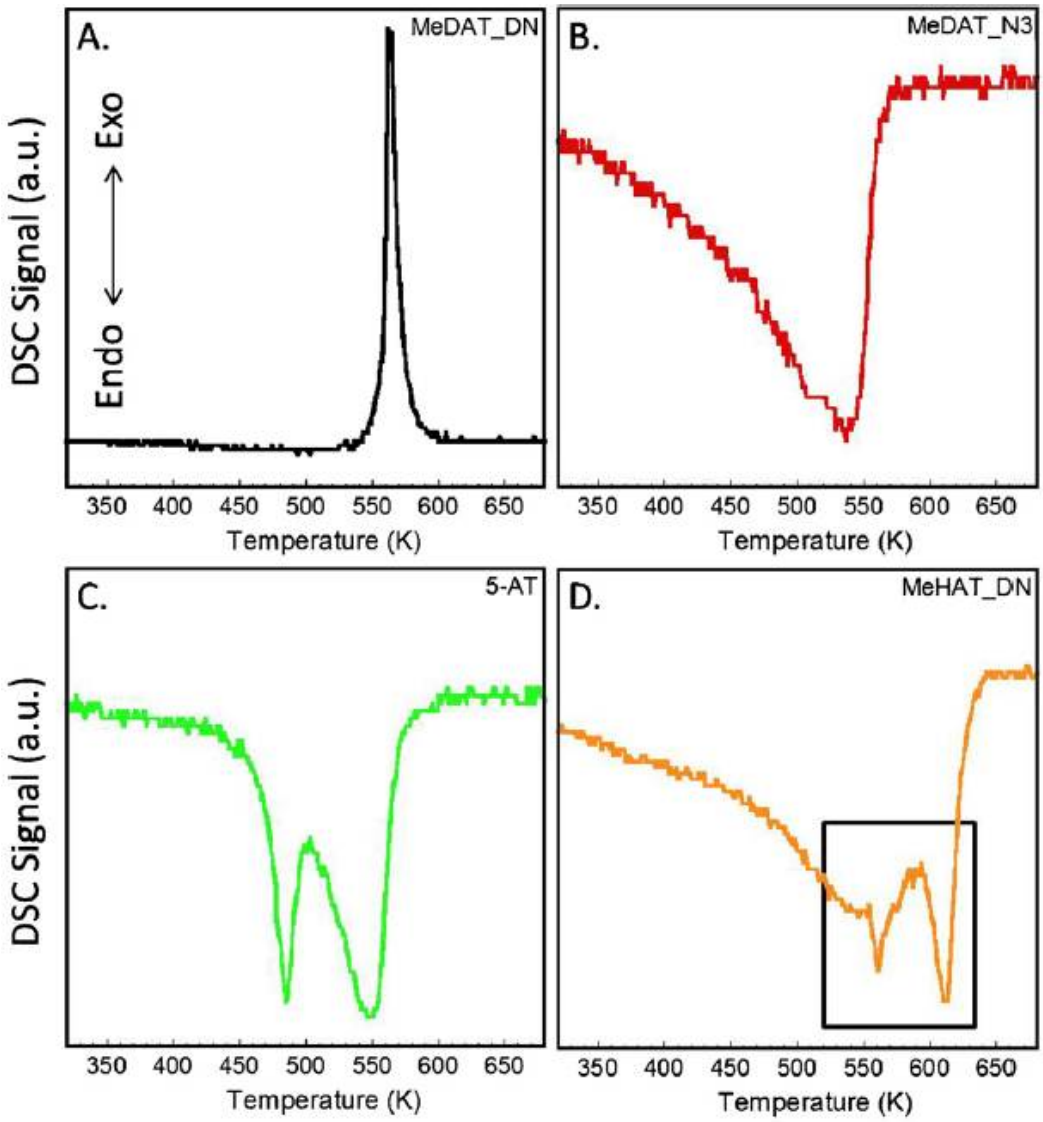

Figure 7.5: μ-DSC traces with a 6500 K/s sec heating rate for A) MeDAT_DN, B) MeDAT_N3, C) 5-AT, D) MeHAT_DN.

In Fischer's previous work the sample showed mass loss at a fairly low temperature of 378 K, however there was no DSC signal at this temperature. The broad endothermic nature of the MeDAT_N3 under high heating rates may be explained if this early mass

loss is due to an endothermic event that can be better detected with the sensitivity of the μ-DSC. Another explanation is evaporation of the sample solution before the energetic material reacts. For this to occur the energetic material would need to dissociate and form a solution with a relatively high vapor pressure. However, we do not expect this to happen as these ionic salts are stable in H_2O and ethanol, and are known to have low vapor pressures.

7.3.3. 5-AT

5-AT is the one material of this set that is a neutral rather than an ionic material. It is tested here as it is the backbone of the cation species in each of the other EMs. This sample at 10 K/min displays a decomposition temperature of 480 K and has a melting point of 478 K [102]. The activation energy was also reported to be (136 to 153) kJ/mol using several different isoconversion methods at heating rates of (0.63 to 40) K/min. Figure 7.5c shows a sample μ-DSC trace for 5-AT showing two endotherms, the first of which peaks at just over 473 K that we attribute to melting, and the second we consider to be the decomposition. The melting of 5-AT occurs from (478 to 493) K consistently for all heating rates, but the decomposition peak increases with heating rate in the range of (505 to 624) K. In the Lesnikovich study [102] only one major endotherm is observed during DSC experiments, as at slow heating rates these two processes likely happen rapidly and cannot be distinguished separately. From Figure 7.4, the activation energy was calculated to be ~66 kJ/mol. This activation energy is more than half of that previously reported, but is reasonable considering the significant difference in heating rates in the two experiments.

7.3.4. MeHAT_DN

Traditional DSC traces for MeHAT_DN at 5 K/min show an endotherm due to melting starting at 363 K and an exotherm starting at 418 K [28]. In the μ-DSC studies the thermal trace of MeHAT_DN in Figure 7.5d can be broken down into multiple reaction steps. First, a slow endotherm starts shortly after the heating and is similar in nature to the endotherm in MeDAT_N3 in Figure 7.5b. Secondly, we observed a sharp endotherm, shown in the boxed region of Figure 7.5d, which is typically followed by a second endotherm. The calorimetric trace does vary as at the slowest heating rates the two endotherms may appear as one. At times, the gap between the two endotherms is very sharp and appears to be similar to an exothermic event. For use in the Kissinger method the decomposition temperature is taken from the final endothermic peak. It is assumed that if the calorimetric trace only shows one endothermic peak at slow heating rates, that both mechanistic events are present but indistinguishable. This endothermic peak occurs in the range of (535 to 757) K and the activation energy for MeHAT_DN is ~44 kJ/mol. No value for the activation energy was found in the literature, but this value is consistent with the other materials in this study.

7.4. Conclusion

This work has successfully demonstrated the ability of the previously designed μ-DSC to study the thermal decomposition of organic energetic materials. For certain materials this system allowed for the probing of different mechanistic steps than is capable with traditional calorimetry experiments. Due to heating rates that are orders of magnitude higher than those that are typically used for DSC experiments we report

activation energies that are considerably lower than those previously reported. Despite relatively high amounts of uncertainty in the activation energy, the reported values fall well below those previously reported and demonstrate the study of different mechanistic events. With the use of the broad heating rate range that this system is capable of, future studies using this technique could provide further insight into the thermal decomposition mechanisms of organic EMs. Possible studies on one material ranging from very slow heating rates, which are typically used, up to very fast heating rates at the high end of this system's capabilities, could be very insightful into the decomposition mechanisms of these materials.

Chapter 8: Summary

8.1. Conclusions

This work was devoted to furthering the knowledge on the ultra-fast reactions in energetic materials. Using a T-Jump/TOFMS and various complementary tools, several contributions were made to the reaction mechanisms of both nanothermites and green organic energetics.

In Chapter 4, Al/Bi_2O_3 was examined following a previous study that correlated the ignition of nanothermites to oxygen release. Al/Bi_2O_3 demonstrated unique properties in an experiment investigating the formation of ionic species during the nanothermite reaction. Through comparison of time-resolved mass spectra of the nanothermite reaction, and that of decomposition of Bi_2O_3 nanoparticles, it was determined that Al/Bi_2O_3 underwent a condensed phase initiation event. This conclusion was based on the fact that the nanothermite ignited prior to the production of any gas phase oxidizer by the bismuth oxide. A high heating rate SEM study was employed to further investigate a sparse mixture of Al/Bi_2O_3 on a carbon-coated SEM grid. This experiment yielded a unique outcome as Bi_2O_3 reacted with the underlying carbon film, rather than the nearby aluminum nanoparticles. In this case the Bi_2O_3 was not in contact with the aluminum, but was resting atop the carbon film, which is further evidence that a condensed phase reaction is the method of initiation for Al/Bi_2O_3. To further demonstrate that the condensed phase mechanism was not dependent on the aluminum fuel, a mixture of carbon and Bi_2O_3 was sampled with the T-Jump/TOFMS and showed a similar condensed phase reaction as Al/Bi_2O_3. The initial Al/Bi_2O_3 reaction was also

demonstrated to be much faster than a comparable Al/CuO reaction, contrary to bulk nanothermite studies. It is expected that this is due to the ability of Bi_2O_3 to rapidly transport its oxidizer through the condensed phase. The presence of charged species within the condensed state may also significantly aid this process. The evidence of condensed phase reactions also supports the recently proposed reactive sintering mechanism for initiation of nanothermites.

Following the demonstration of condensed phase reactions in Al/Bi_2O_3 and C/Bi_2O_3, the next logical step was to investigate this event for other oxidizers. This led to the investigation of C/CuO and C/Fe_2O_3, which aside from having mechanistic importance, are also relative to the field of chemical looping combustion. This study showed that the metal oxides CuO and Fe_2O_3 are also capable of condensed phase reactions. The results of the carbon oxidation experiments in the T-Jump/TOFMS were compared with that from previous soot and carbon oxidation studies. The main difference in TOFMS studies and previous studies is the use of a gaseous oxidizer in nearly all other studies. The Nagle and Strickland-Constable model was used to compare the typical oxidation rate of carbon with that of an estimated reaction rate from the experiment. The experimentally determined reaction rate of carbon oxidation through the condensed phase reaction is orders of magnitude faster than previous gas phase oxidation studies.

The study in Chapter 6 examines the decomposition of novel green energetic materials using the T-Jump/TOFMS. The goal of this study is to compare several similar GEMs with a common tetrazole containing cation, and determine how minor molecular differences affect the breakdown of the material. The results suggest that the

decomposition of the tetrazole ring is highly dependent on the location of functional groups along the outside of the ring. No correlation was observed for the breakdown of the tetrazole ring with the composition of either the functional groups or the anion. However, thermal dependence was impacted by anion composition. Two separate decomposition pathways were determined for the tetrazole structure, one that produced N_2, and the other HN_3. Both of these pathways had been previously reported for different experimental conditions. Several of the materials in this study were previously subjected to product species identification experiments under slow heating rates in other works. Significant differences were observed for the current study and the previous slow heating rate studies suggesting that different mechanistic events are at play during rapid heating.

To complement the T-Jump/TOFMS study on GEMs of chapter 6 it was necessary to have another instrument to probe the reactivity of energetic materials at high heating rates. Chapter 7 covers the use of a NIST developed micro-differential scanning calorimeter to investigate several of the materials from Chapter 6. This system was calibrated at different heating rates using materials with known thermal signatures, and the GEMs were tested at the same heating rates. A varied heating rate experiment was performed to probe the change in decomposition temperature. Using this information, the activation energy of each material was determined using the Kissinger method. Each material demonstrated an activation energy of nearly half of the previously reported value at slow heating rates. The presence of lower activation energies further support the T-Jump/TOFMS results that different mechanistic processes are at play during fast heating.

The findings of this work have produced several notable results, specifically the observance of condensed phase initiation event for Al/Bi_2O_3 and carbon metal/oxide

mixtures. Prior to this work there was little experimental evidence to suggest such a reaction. This is also further evidence for the recently proposed reactive sintering mechanism for nanothermite initiation. The condensed phase initiation event is a very interesting finding, and future work should be devoted to further understanding this process.

8.2. Recommendations for Future Work

8.2.1. Negative Ion Detection

It is of considerable interest to determine the negative ionic species that are formed during the thermite reaction. The positive ionic species were previously reported [29], and in order to obtain a more complete mechanistic understanding, the negative ions must also be confirmed. It is expected that the negative ions consist of an oxygen species, possibly O^{2-} as this ion has been reported as present in the Bi_2O_3 lattice.

In the previous ion experiments the negative ionic species could not be detected by simply adjusting the voltages of the normal setup. In our self-ionization paper [29] several different voltage configurations were tried, but without success in negative ion detection. It should be noted that the total negative ion production was monitored successfully, but not the species identification. It was not initially evident whether the pulsing system was capable of handling an initial bias of -1300 V to satisfy the voltage configuration for negative ion detection in Table 8.1 (Negative Ion Species Detection Proposed (1)). Experiments have since shown that this configuration is possible. Sample experimental runs with this configuration for Al/CuO have been performed, and no arcing was observed. Therefore the voltage configuration for 'Negative Ion Species

Detection Proposed (1)' should be suitable for negative ion detection. However, after several experimental runs there was no detection of negative ionic species.

The cause of this is likely a negative voltage on the plates of the MCP, which repel the negative ions. Figure 8.1 is an electrical schematic for the applied voltages for the MCP detector.

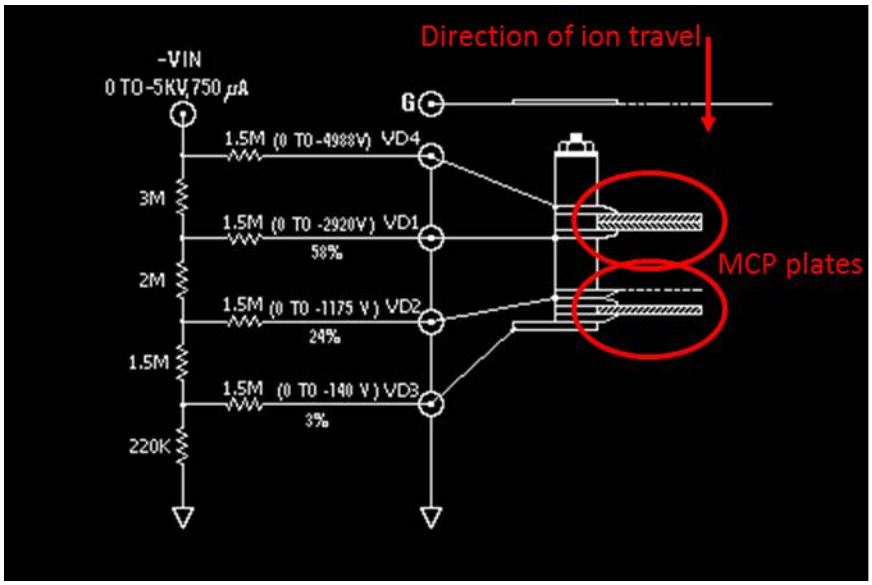

Figure 8.1: An electrical schematic for the voltages applied to the MCP detector. Image is taken from Jordan TOF Products, Inc. [134].

The points labeled VD4, VD1, VD2, and VD3 represent the points of voltage application to the 3 MCP plates. The MCP plates are circled in red; the section between VD4 and VD1 has 2 MCP plates, and the section between VD2 and VD3 has 1 MCP plate. The area marked 'G' is connected to the liner of the TOF tube. For the typical spectrometer setup, positive ions enter the MCP region through the plate marked 'G', and then are accelerated by the negative voltage at VD4 (-4988 V) into the MCP plate at VD4. Impact of an ion with the MCP plates creates up to 10^8 electrons [135], which is why the electric field after VD4 is designed to further accelerate negative species. However, if a negative

ion enters the region through ‘G’, it may be repelled by the negative voltage of VD4 and never reach the MCP plates. This was the same setup used previously for negative ion detection, but during that study the placement of the filament was directly in the ionization region of the mass spectrometer. This likely allowed for more ions to reach the MCP region, and probably allowed ions with much greater kinetic energy to reach the region as there is a direct line of sight from the ionization region to the MCP. Therefore many ions may have had the energy to overcome the repulsive electric field.

Experiment / Extraction Plates	**Negative Ion Species Detection Proposed (1)**	**Negative Ion Species Detection Proposed (2)**
Filament Placement	Edge	Edge
A1	-1500	Pulsed (Ground to -200V)
A2	Pulsed (-1500 to -1300V)	Ground
A3/Liner	Ground	Ground

Table 8.1: Proposed experimental setup for negative ion species detection experiments.

For negative ion detection, the ion signal will be diminished from that of the previous experiment as the filament is placed 1-2 cm outside of the ionization region. Therefore, the voltages of the MCP will need to be adjusted to allow easier detection of negative species. The voltages for each plate are listed in Figure 8.1 and are for the maximum recommended input of voltage of -5000 V, however this schematic is an edited image taken from Jordan TOF Products, Inc. [134] so it is not entirely clear how the voltage values were obtained, but we assume that they are measured values. To simplify

the problem, sample voltages are given in Table 8.2. The important factor with re-configuring the voltages for the MCP is to ensure that the voltage *drop* remains the same across each set of plates. Each MCP plate has a recommended maximum applied voltage of 1000 V. In other words, the voltage drop over VD4 – VD1 can be no larger than 2000 V (2 plates, 1000 V per plate), and V3- V2 can be no greater than 1000 V.

	Present Voltage (sample)	Required Voltage (sample)
VD4	-5000	+200
VD1	-3000	+2200
VD2	-1200	+4000
VD3	-200	+5000

Table 8.2: Sample applied voltages for the MCP plates.

Due to the circuitry of the voltage divider box, it is not possible to obtain the desired positive voltages in Table 8.2 by simply using a positive voltage supply. This will require the building of a new voltage divider box to meet the required voltage settings. This box could be built in-house (examination of the current divider box, which is attached to the TOF tube shows that the connections are relatively basic), or by Jordan TOF. If a new divider box is built in house (I think this is very feasible), I recommend first finding an accurate way to measure or calculate the voltages for each point in Figure 8.1, so that the circuit is fully understood (several unsuccessful attempts were made to obtain the values in Figure 8.1 with basic circuit analysis calculations). A new circuit will then need to be designed to obtain voltages similar to those shown in Table 8.2 (assuming a +5000 V input). It is necessary to ensure that the voltage drop over each

MCP plate is not greater than 1000 V. It should also be noted that the 5000 V input used in this example is the maximum allowed voltage input and is far greater than the typical MCP voltage input of ~3000 V.

If arcing occurs for nanothermites that produce more intense ion pulses (i.e. Al/Bi_2O_3), then the setup 'Negative Ion Species Detection Proposed (2)' in Table 8.1 can be tried. This setup has little to no voltage drop between the filament and plates, and should not result in arcing. This produces a relatively weak electric field compared to previous experiments, and requires calibration of the mass spectrometer to determine the product species. The major downfall of this method is a significant decrease in spectrum resolution. It is possible that without an acceleration potential between plates 2 and 3, signal may be too poor to identify the product species. However, as the main goal of this experiment is to determine the negative ionic species, it may be possible to do this at the cost of greatly reducing resolution and intensity of the spectrum.

8.2.2. Activation Energy Investigation Over a Broad Heating Rate Range

Lower activation energies have been demonstrated for both nanothermites and organic energetics when submitted to high heating rate conditions. It would be interesting to investigate the change in activation energy under a complete range of heating rates, preferably with a single instrument to avoid any experimental deviations. Variable heating rate experiments for the metal oxides and carbon/metal oxide mixtures were performed for heating rates from 10^4 – 10^5 K/s. The T-Jump/TOFMS may be capable of heating rates as low as 10^3 K/s without modification, however there is still a large gap between the rapid rates in this experiment and the ~10 K/s heating rates of

traditional DSC experiments. The μ-DSC system could potentially be used for this study, although the current maximum temperature of the system is ~600 ^{o}C, which may be too low for nanothermite studies. If one system can be used for detection of reactive events over a very broad range of heating rates then it may be possible to track multiple reactive processes for a single system. An example of this type of study has been demonstrated by Choi *et al.* (Figure 8.2) for the crystallization of a $Ge_2Sb_2Te_5$ thin film. Where heating rates ranging from 3-30 ^{o}C/min, they have an activation energy of ~226 kJ/mol, but for faster heating rates of 50-500 ^{o}C/min the activation energy is reduced to ~47 kJ/mol [19]. This study is still over a relatively small range of heating rates, and yet observes a significant change in activation energy. A heating study over a much broader range of rates could uncover more mechanistic transitions, and potentially give a much better understanding on how different heating regimes affect the reaction of a material.

On the surface, the T-Jump/TOFMS setup requires little alteration to perform these experiments. The mass spectrometer is easily adaptable to function at slower heating rates, however, our current power supply used for heating the filament is primarily designed to heat from 2 to 100 ms. To heat at much lower rates this power supply would need to be adjusted or replaced. The only remaining concerns are whether the small amount of samples required for use in the T-Jump/TOFMS can put out enough signal to consistently be detected at slow heating rates. Also, under slow heating rates we can observe a clear temperature gradient throughout the heating filament. This would require some further heat transfer calculations to ensure the temperature profile throughout the filament.

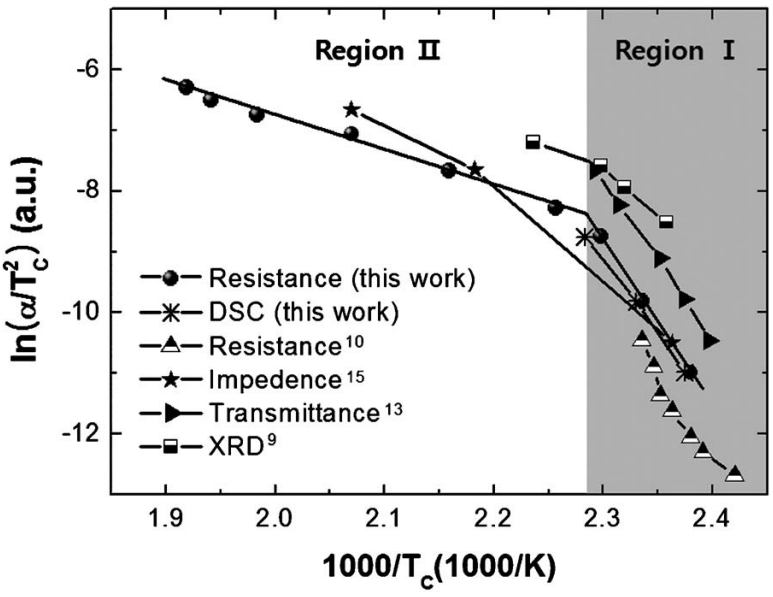

Figure 8.2: Demonstration of the shift in activation energy by Choi *et al.* [19] using the Kissinger Method.

8.2.3. Inorganic/Organic Energetic Materials

Both inorganic and organic EMs have positive attributes that make them attractive for energetic applications. In particular organic energetics react very quickly, and therefore have a high rate of energy release. On the other hand, the amount of stored energy within an organic energetic is typically lower than that in an inorganic nanothermite. Also, due to the way that nanothermites are mixed via a top down method, it is relatively easy to tune these materials for different stoichiometries, affecting performance and sensitivity. One way that nanothermites could be improved is to increase their rate of reaction. It is thought that decreased particle sizes, which further decreases diffusion lengths and increases the surface to volume ratio will further enhance the reaction rate. However, once aluminum nanoparticles get to a certain diameter their

alumina shell becomes the dominant species of the composition, resulting in a sample that is primarily relatively inert Al_2O_3.

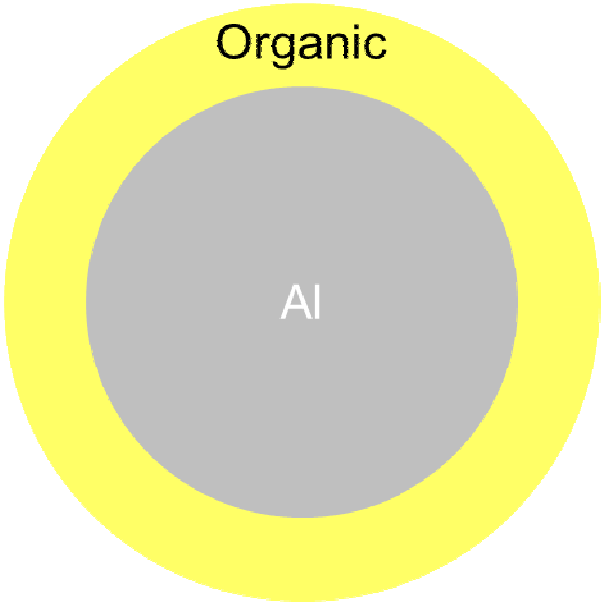

Figure 8.3: Illustration of possible coating option for replacement of alumina shell.

One interesting solution to this problem is to the replace the Al_2O_3 coating with a material that is not inert. This tends to be a difficult task as once aluminum is exposed to air it will quickly form an oxide shell. In order to coat a bare aluminum particle it is necessary to have an on the fly method that can create aluminum nanoparticles, and subsequently coat them in one process. Our group has a lot of experience with aerosol techniques that are capable of this very process, and we have previously coated Al with a carbon nanolayer via this method [136]. Aluminum nanoparticles have been shown to enhance burning in propellants when used as an additive, but the question remains of what would happen if these materials were mixed at the nanoscale? If a bare aluminum was coated with an organic energetic material, as depicted in Figure 8.3, and mixed with

an oxidizer as a nanothermite, some unusual outcomes could occur. Ideally, this formulation would act like a material with the energy storage of nanothermites, but with the energy release rate of an organic energetic.

There are a few mechanistic changes that are possible if nanoparticles of this fashion were used. First off replacing the Al_2O_3 with an energetic material will surely have an effect on the release of the aluminum to the oxide. Assuming that the organic will decompose off to expose the Al core at a much lower temperature than Al_2O_3, which judging just from the organic examples given here, should be a reasonable assumption, bare Al could be completely exposed rather than just a partial exposure, as can be the case with a typical Al_2O_3 covered Al nanoparticle. The other possibility is that not only will be the aluminum be exposed if the organic EM decomposes, but the heat of combustion from the organic EM could enhance the reactivity of Al and the metal oxide in the thermite. Imagine an organic coating that has a flame temperature greater than the boiling point of Al at 2519 ^{o}C. This could vaporize the Al and completely decompose the oxide, causing a significant enhancement of the nanothermite reaction. It is unclear exactly what the mechanistic differences might be in this type of situation, but with our abilities to characterize the initiation of both organics and inorganics, it should be possible to study this mechanism and possibly tune the coatings to maximize performance.

8.2.4. Effect of Charge in the Nanothermite Reaction

For the nanothermite reaction we have provided evidence to suggest that ionic species may have an important role in ignition. Recently, work has been done to model

the exothermic reaction of Al/CuO [137, 138] using the Cabrera-Mott oxidation mechanism [45]. The Cabrera-Mott method is typically used for a heterogeneous gas-solid reaction (O_2 reacting with a metal surface), but this recent work demonstrates its use for condensed phase reactions. These studies are designed to probe the low-temperature reactions of Al-CuO prepared through arrested reactive milling (ARM). The exothermic reaction for Al-CuO is observed at very low temperatures of 350 – 450 K, but also is a very slow reaction lasting for hours. The Cabrera-Mott kinetics are used to model the heat release as measured during a DSC experiment, and can provide a decent prediction of the point of initial reaction for heating rates ranging from 5 – 40 K/min. The authors predict that this model could further be used to accurately predict the thermal ignition of nanothermites under rapid heating conditions [138].

The evidence of condensed phase initiation, particularly with Al/Bi_2O_3, strongly suggests that the ionic species within the condensed state play a significant role in the initial nanothermite reactions. This evidence includes:

1. Al/Bi_2O_3 undergoes a condensed state ignition event
2. In ion production experiments, Al/Bi_2O_3 produced the most ions, and did so at the greatest rate.
3. In ion production experiments, a measure of negative ions was not attainable from the Al/Bi_2O_3 nanothermite due to shut down of the TOFMS. For all other samples, negative ions were successfully detected. This suggests that the production of negative species is much more intense in Al/Bi_2O_3 compared other nanothermites that were tested.

4. The initial reaction for Al/Bi_2O_3 is faster than the other thermites tested, contrary to some previous experiments with bulk nanothermites.
5. The production of ionic species either coincides with the start of reaction, or occurs just before reaction (this seems to depend on the system), indicating that they are somehow associated with the initial reaction.

Of particular interest is the fact that, of the systems examined, Al/Bi_2O_3 has the highest rate of ion production and the fastest initial reaction. It is my belief that these two events are related, and that the ignition of Al/Bi_2O_3 benefits from its ability to rapidly transport ions through the condensed state. The use of Cabrera-Mott kinetics to model this reaction could provide some more insight into these rapid reactions and could further justify the importance of charged species during ignition.

Appendix

SIMION 8 Tutorial

The SIMION 8 program can be used to create basic models of TOFMS components and predict ion trajectories. In this tutorial a basic setup of the extraction plates of the TOFMS will be made.

Startup:

1. After starting SIMION 8 you will come to the SIMION welcome screen, select **OK** to get to the main menu.
2. There are three main sections of the main menu:
    a. Potential Arrays (PA)

        - The basis of the SIMION program is the potential array. This section is used to design the desired electrode structures.

    b. Ion Optics Workbench

        - This section allows you to view and manipulate your previously created arrays

    c. Settings and Utilities

        - This section can be used to adjust various settings within the SIMION program. The most pertinent settings in this section are the 'Max PA Size' and 'Max Ions'. These will typically not need adjustment, but if creating a large detailed system then it may be necessary to increase the maximum number of points.

Designing a Potential Array (PA):

We will design the extraction region of the mass spectrometer with the filament nearby to observe how the placement of the filament affects the ion trajectory.

1. In the section 'Potential Arrays (PA)' select **new**.
2. In this part we define the size of the potential field. It is important to consider your problem carefully before defining the field. The size of the field and the number of points within the field will affect the accuracy of the ion trajectory and the shape of the objects (electrodes). The dimensions of the TOF extraction region are shown in Figures 1 and 2.
    a. We will make a grid that has units of 1 grid point per millimeter. If we have a field of dimension 60x50x30 mm (x, y, z), then it should give plenty of space to create the extraction region with filament. Before we input the dimensions we will note that we can use the symmetry about the x-axis to reduce the number points needed. The inputs will be:
        i. Symmetry: **planar**.
        ii. Mirroring: check 'y' (this mirrors about y=0).
        iii. x: 60 points.
            y: 25 points.
            z: 30 points.
        iv. Max PA size: this will automatically update.
        v. Field Type: **electric**.
    b. Select **OK**.

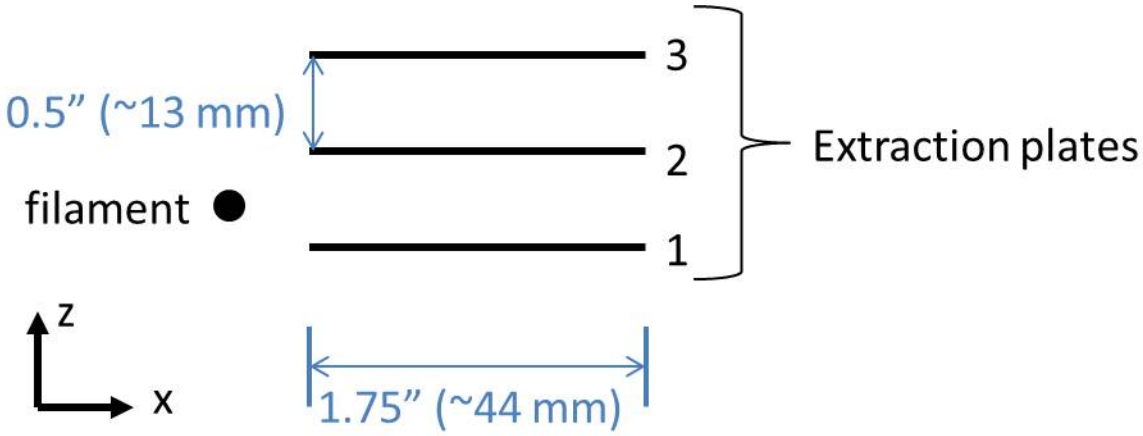

Figure 1: Profile view of the extraction region. The filament extends into the page.

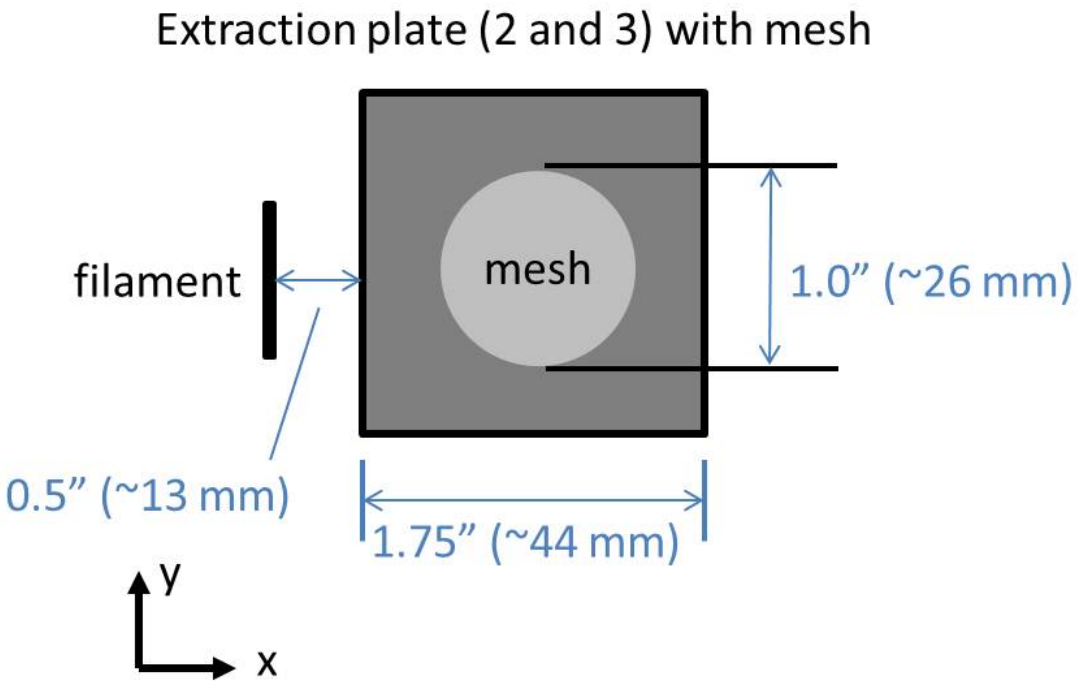

Figure 2: Top view of extraction region. Extraction plates 2 and 3 have a wire mesh, and extraction plate 1 is solid.

3. AT THIS POINT SAVE THE FILE, call it ‘extraction region.pa#’.
    a. IT IS IMPORTANT THAT YOU NAME THE FILE ‘.pa#’. If this is not done then the setup will be unable to refine.

4. After saving, make sure that ‘extraction region.pa#’ is highlighted and select, **modify**.

Modifying the PA:

Once in the modify section we can begin to build the desired array. In the center of the screen you should see a series of green diamonds; these are the nodes of the array. Near the top of the screen the box ‘1 XY’ should be selected, and your screen should look similar to that in Figure 3. Remember that we are going to use symmetry across the x-axis (y=0) so we will have to plan accordingly. Note that the following process is just one of many ways to build this array.

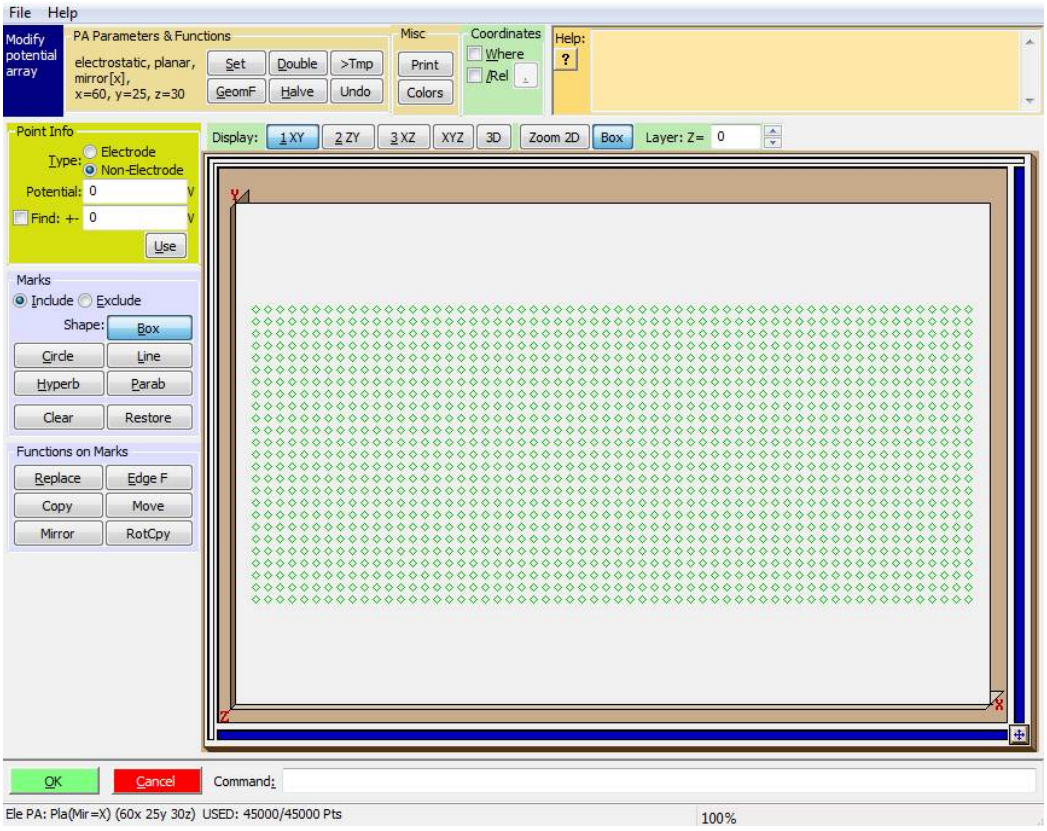

Figure 3: screenshot of initial setup for the potential array.

1. Near the top of the screen choose '3 XZ' to get to the X-Z plane. Note that the origin of the axis is at the top of the screen.
2. We will start by creating the extraction plates. Start by making plate 1 at the origin of the Z and X axis. Move the cursor to the top left corner (x=0, z=0) and click the left mouse button, hold and drag to x=43, z=1. This will select a 2x44 array, and at 1mm/grid point, you have a 44mm (~1.75") long array.
3. After you have selected these grid points, go the 'point info' section on the left side of the screen. There is a choice between 'electrode' and 'non-electrode', choose 'electrode' and make sure that the 'potential' box reads **1**. At this stage the electrode potential is essentially a ranking or naming system. So for the first electrode you start with **1**, next electrode will be **2**, and so on.
4. At the left of the screen in the 'Functions on Marks' section, select **Replace**. This should create the electrode in the previously selected squares and should look like Figure 4.

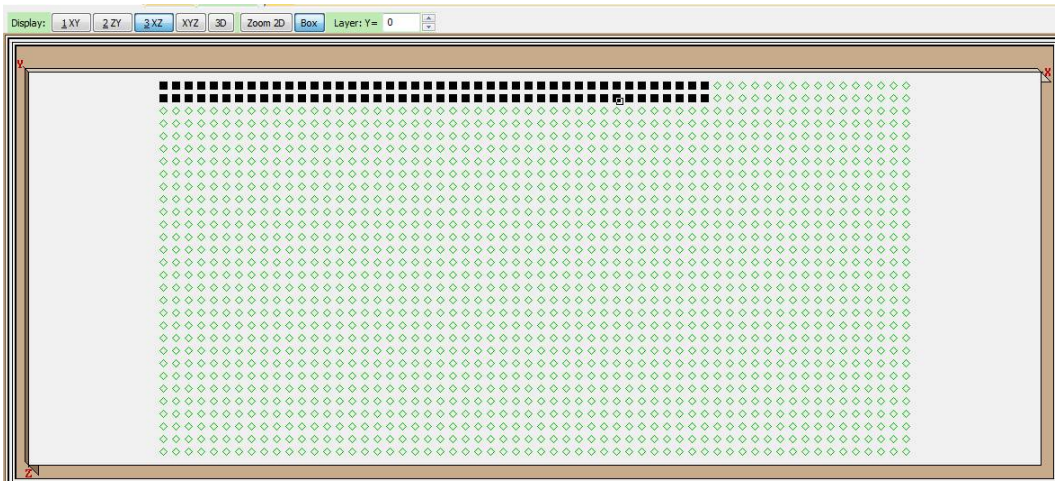

Figure 4: screenshot of initial created electrode for extraction plate 1.

5. At the top of the screen choose ‘1 XY’. You should see a rectangle that is 44x25 grid points. If you choose ‘3D’ at the top of the screen you will see a 3D view of the electrodes. This view shows the symmetry about the x-axis. If you right click on the image and drag the mouse you can rotate the image.
6. At the top of the screen again choose ‘1 XY’. This rectangle is 44x25, but we want it to be 44x22, so that when mirrored through the x-axis it will form a 44x44 square.
7. Select the top 3 across the top of the array. At the ‘point info’ box select ‘non-electrode’, and press **replace** in the ‘Functions on Marks’ section. This should erase the selected points and leave you with a 44x22 rectangle like in Figure 5.

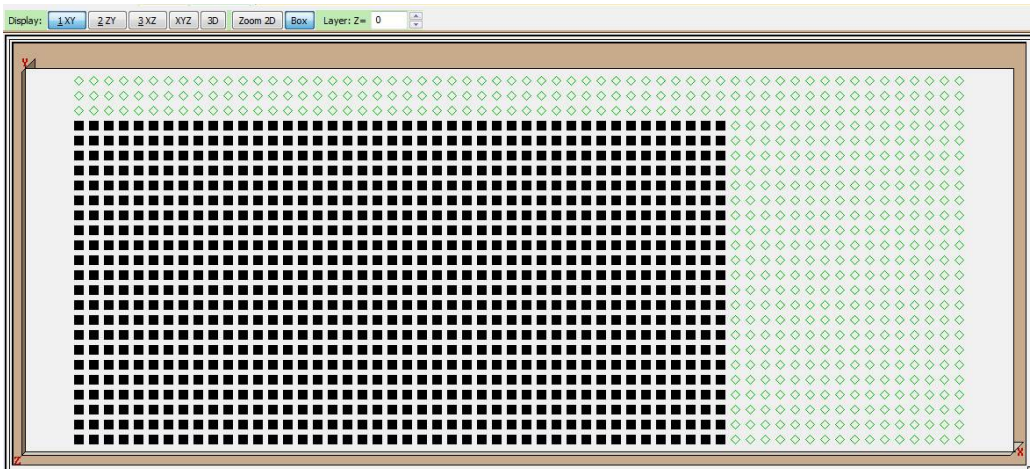

Figure 5: Screenshot of extraction plate 1 array.

8. Now we will build extraction plates 2 and 3. From Figure 2 we see that these two extraction plates have a section composed of wire mesh. This allows ions to travel through the grid while maintaining a uniform electric field (if the circle in

Figure 2 did not have a wire mesh then the field would be distorted). To reduce the difficulty of this model we will assume the entire 2nd and 3rd extraction plates are composed of mesh. If you create an array that is only 1 grid point thick, SIMION will recognize this as a mesh.

9. To start plates 2 and 3 choose '3 XZ' at the top of the screen. From the dimensions in Figure 1, the plates should be ~13mm apart. Highlight the grid points from x=0, z=14 to x=43, z=14. In the 'point info' section choose **electrode** and enter the 'Potential' as **2** for the second extraction plate.
10. Select **Replace**.
11. Repeat step 9 at z=27. Make sure the 'point info' section you enter the 'Potential' as **3** for the third extraction plate.
12. We want the filament in between the 1st and 2nd extraction plates, 13mm from the plates. In the 'Marks' section on the left hand side choose **circle**. Starting at the point x=56, z=7 make a circle that extends out one grid point. In the 'point info' section choose **electrode** and enter the 'Potential' as **4**. Choose **Replace**. You should see a 'filament' that is a 3x3 rectangle. This is a case where using more grid points would have allowed us to create a more accurate filament. We could also make the diameter of the filament a single grid point, but this would allow ions to travel through the filament like a grid. We want to observe if ions hit the filament, so we will leave it as is. Your array should now look like Figure 6.

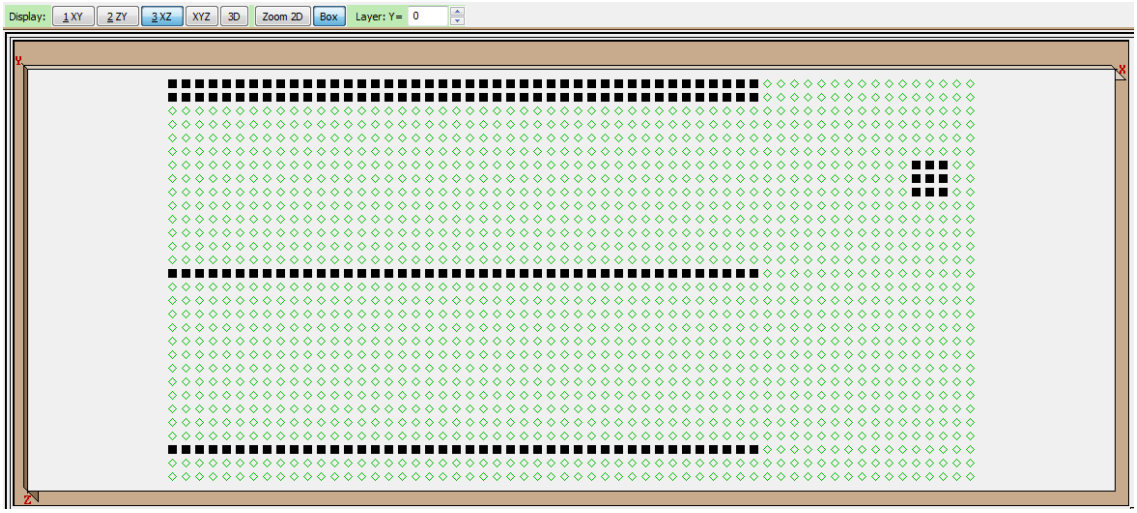

Figure 6: Screenshot of the three extraction plates and filament.

13. Now we have the extraction plates that are slightly too big, 44x25, and we need to decrease the size to 44x22. We also want to decrease the size of the filament to 20mm.

14. At the top of the screen choose '2 ZY'. You can see that the 2nd and 3rd extraction plates are slightly larger than the 1st. In the 'Marks' section choose **Box**, then highlight the tops of the 2nd and 3rd plates to make them even with the 1st, choose **non-electrode**, set potential to **0**, and choose **Replace**.

15. To adjust the size of the filament stay in the '2 ZY' plane and near the top of the screen where it says 'Layer: X = _____' input **56** and press enter. This will bring us to the plane x=56, and we can see the filament. Keep in mind that we are mirroring this across the y=0 plane. We want the final length to be 20mm, so highlight the points above y=9, and erase them using **non-electrode** with the potential set to **0**.

16. Before leaving the '2 ZY' plane, change your 'Layer: X=_____' back to **0**. If this is not done it will affect your views in the other planes as well.
17. To get a better view of the current array, choose '3D' near the top of the screen. Again by right clicking and dragging you can rotate the image. Your array should look like Figure 7.

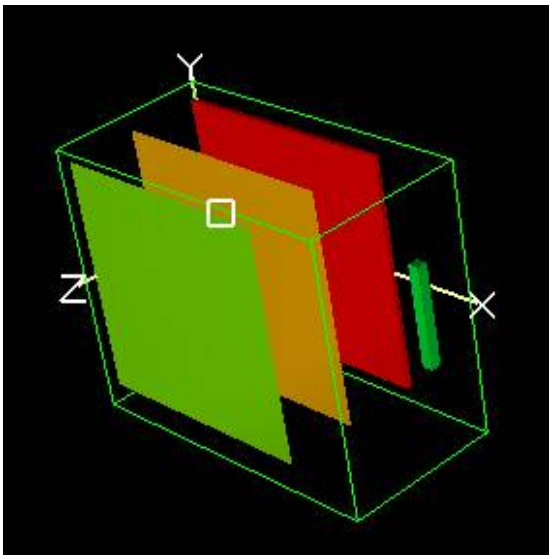

Figure 7: 3D view of the finished potential array.

18. The potential array is now finished. Click **OK** to finish the array.
19. Save the file.

Refine and Fast Adjust the Array:

The refining process solves the Laplace equation to define the potential field within the array.

1. Click **Refine**.
2. Use the default values and select **Refine** at the bottom of the screen. The system is now refined and we can apply the desired voltages to each electrode.

3. Make sure that ‘extraction region.pa0’ is highlighted. If it is not, load that file and select it.
4. Select ‘Fast Adjust’.
5. Select ‘ZY (x)’ at the top of the screen. This will give you a better view of the three extraction plates.
6. We want our voltages to be that of the typical setup for positive ion detection. The input boxes at the top of the screen have the naming convention that we used previously. So box ‘1’ corresponds to the 1st extraction plate. For this box, input **0** V. In box ‘2’ input **-200** V. Box ‘3’ the third extraction plate, put **-1500** V. In box ‘4’, the filament, put **20** V.
7. When your voltages are set, select ‘Fast Adjust’.
8. Once again save your progress.

Ion Optics Workbench (IOB):

In this section you can observe the ion trajectory. You can also choose the makeup and starting position of the ions.

1. Select **View/Load Workbench**.
2. In the ‘Display’ section, you can choose **PE** to observe the potential field. The ‘XZ field gives the best representation of the flow of the ions through the extraction region. This will change depending on the plane you are in. You can adjust the look of the PE field to make it more defined. At the top of the screen select the ‘PE/Contours’, in the ‘PE View’ section you can adjust the

'Gstep' which will change the coarseness of the grid. To make a finer grid change the 'Gstep' down to 1. You can also change the relief to better show the changes in the PE field. I have found that **.75** or **1** is a good value. The field should look similar to that in Figure 9 below.

3. In the 'Display' tab at the top you can also adjust the view of the PE field. Click 'Box' to remove the box around the PE field.
4. To insert and define ions, choose the particles tab at the top of the screen.
5. Choose **Define**. This will open a screen providing many different options to tune the ion group.
6. There are a number of input options. In the 'Selected particle group', input **100** for the 'num particles'.
7. For 'Mass' you can use **27** a.m.u. for the mass of the aluminum ion. 'Charge' is **1**.
8. Typical ion formation occurs in between the 1^{st} and 2^{nd} extraction plates, as this is where the E-gun beam enters the system. Therefore we will start our ion formation in the same plane. In the 'Source Position' section, in the first box select **line sequence**, and in the second box select **first, step**. Following this, in the input boxes for 'First', input x=0, y=0, z=7 (this will start the ions in between the 1^{st} and 2^{nd} plate. Then in the 'Step' boxes input x=.5, y=0, z=0. This will move each progressive ion .5mm in the x-direction. The following inputs should follow that in Figure 8.

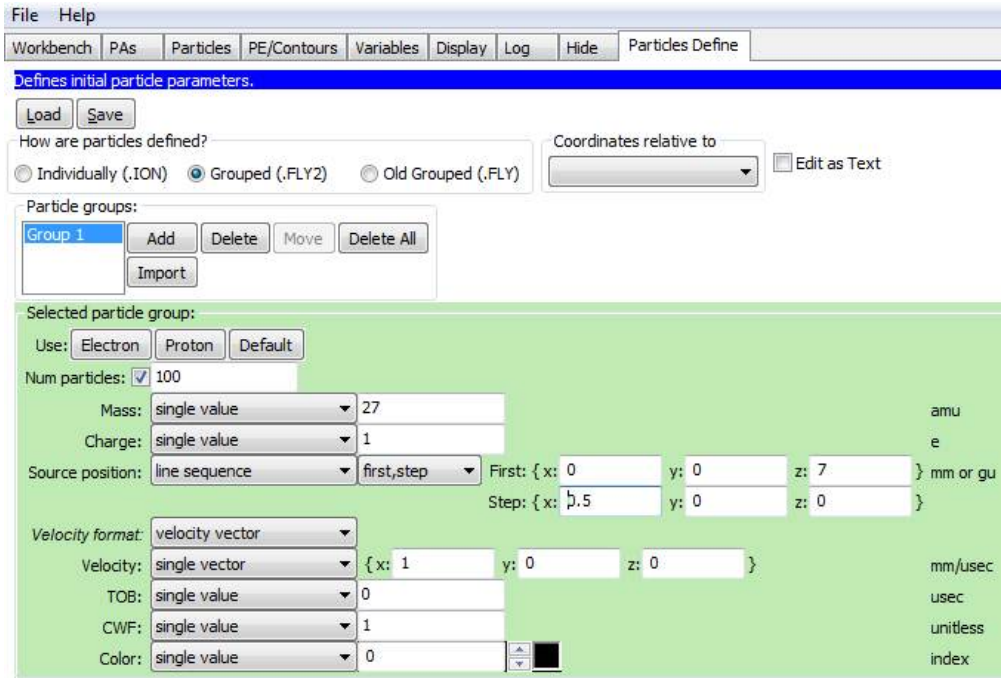

Figure 8: Inputs for ion flight.

9. After the settings are done, click **OK**.

10. At the bottom of the screen choose **Fly'm**. This will input the ions and allow them to follow the potential field. If you choose the **XZ** plane and the **PE** your view should look like Figure 9.

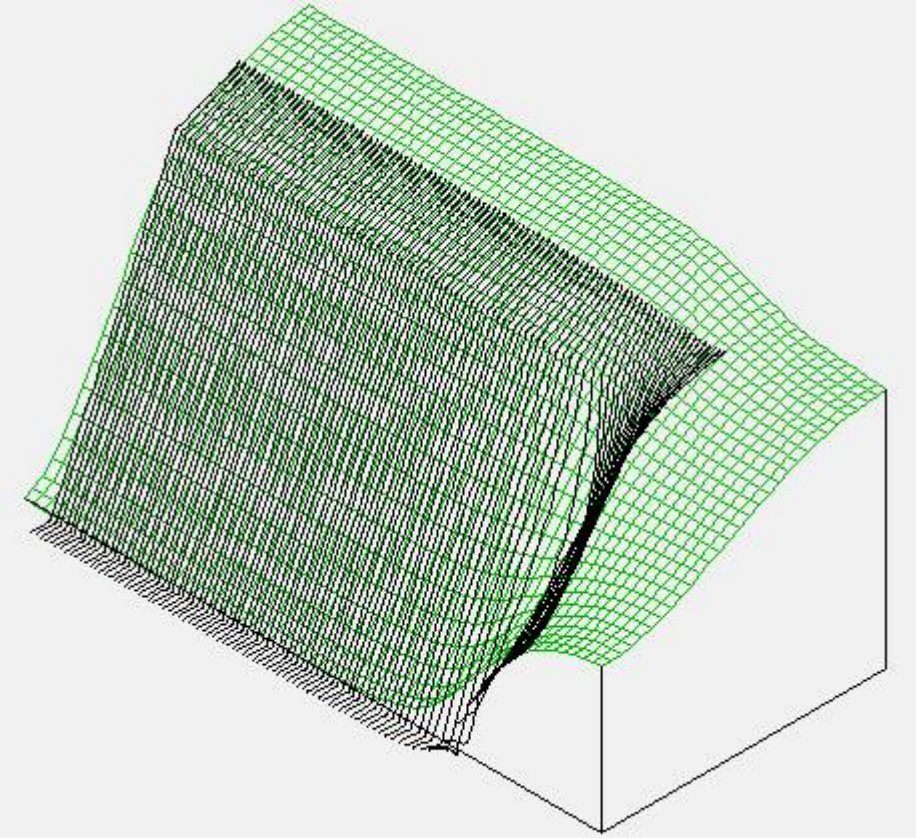

Figure 9: PE view for ion trajectory for typical TOFMS setup.

11. To get an idea of how the applied voltages affect the field, we can change back to a positive voltage system similar to what was previously used for the TOFMS.
12. Select **Quit**.
13. Now that the array is built these changes can be done fairly quickly. Select **Fast Adjust**.
14. Change the voltages to 1: **4500**, 2: **4300**, 3: **3000**, 4: **20**. Select **Fast Adjust**.
15. Select **View/Load Workbench**.
16. In the 'Display' view select the **XZ** plane and **PE**, and **Fly'm**. The resulting ions should look like Figure 10. From this flow of ions to the filament we can

see the change in the gradient of the electric field between the high voltage plates and the filament. It is this steep gradient which caused issues with the combustion of nanothermites within this system.

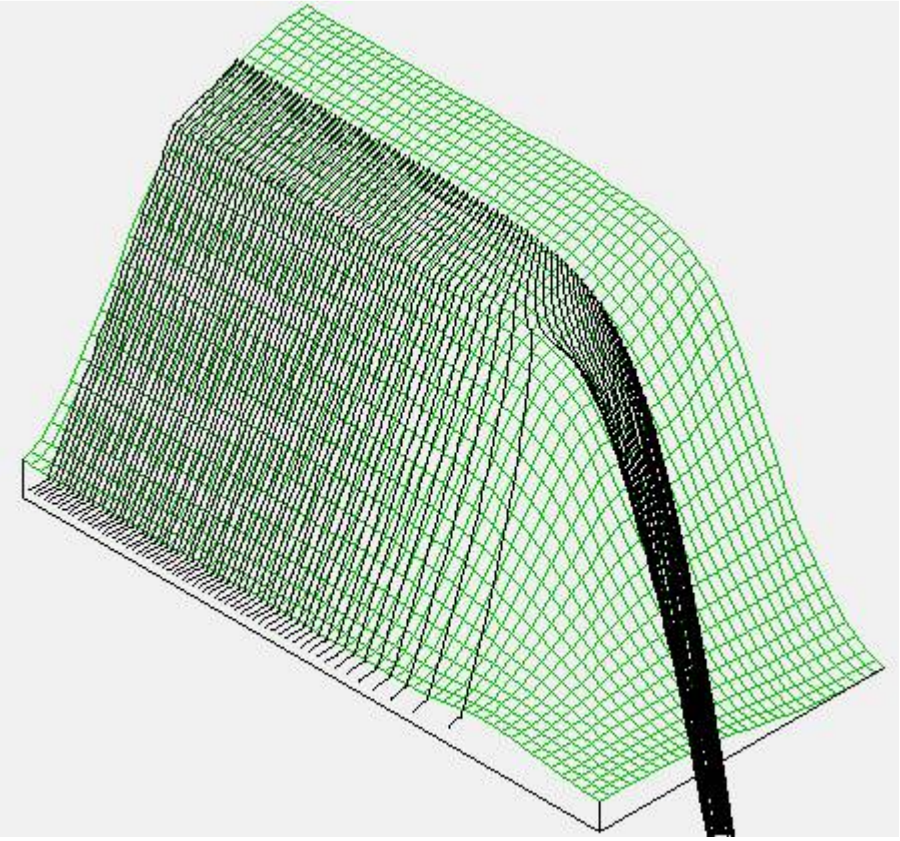

Figure 10: Extraction region with positive high voltage.

Further Analysis:

1. To create a potential array more similar to that in our original T-Jump/TOFMS publication [22] you need to reload ‘extraction region.pa#’ and modify your potential array to include the circular mesh like in Figure 2. (The published array was included slightly larger field of grid points.)

2. From the ‘3 XZ’ plane your final array setup should look like that in Figure 11 and with the applied voltages of a typical from the high voltage TOFMS setup (4500 V, 4300 V, 3000 V) your ion trajectory should look like that in Figure 12.

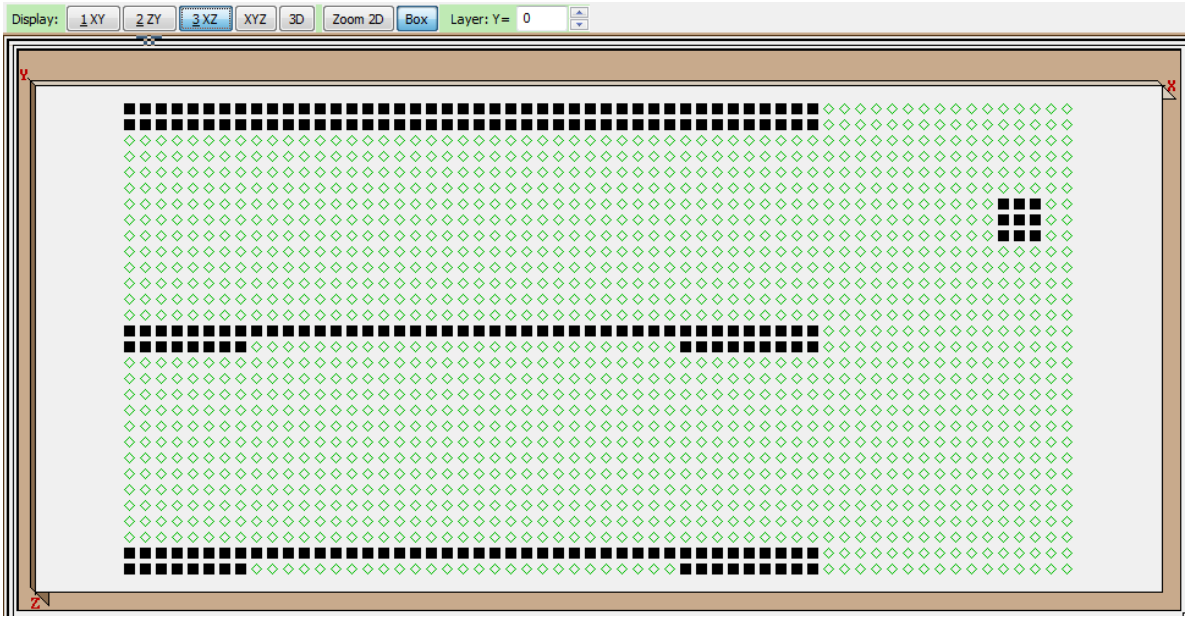

Figure 11: View from the XZ plane of the potential array including the wire mesh.

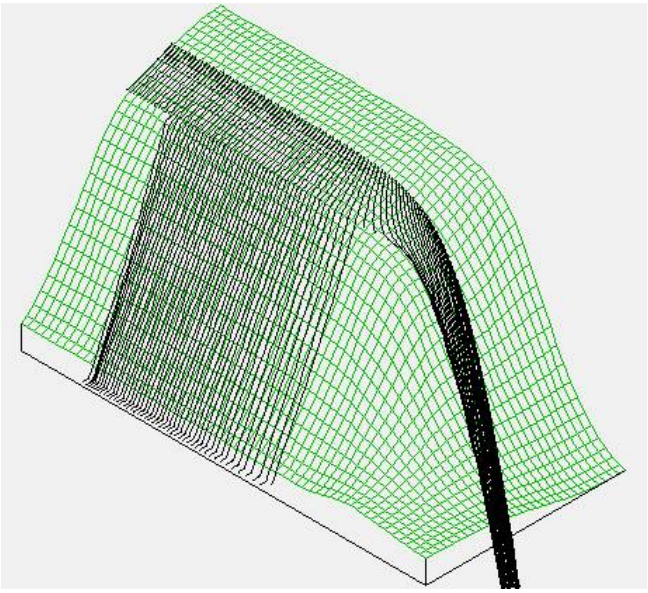

Figure 12: PE view of high voltage ion trajectory with extraction plates including wire mesh.

3. There are other adjustments and analysis capabilities within SIMION:
    a. In the ion workbench under the ‘Pas’ tabs there is a ‘positioning’ section. One useful tool here is the ‘Scale’ adjustment. It is currently set to 1mm/gu (gu=grid unit), which is the conversion we were using. Using this function, your setup does not have to be designed in mm.
    b. Under the ‘workbench’ bench tab you can edit the size of the workbench. Therefore if you were to add an MCP you could adjust the workbench place it 1000mm downstream of the extraction region to see if the ions will hit the MCP.
    c. Under the ‘particles’ tab there is an option on the left hand side for ‘data recording’. This section allows you to create a text file with various ion trajectory details. This can be useful to determine the number of ions that reach a point, such as the MCP.
        i. On the bottom right of the ‘data recording’ screen there is an input for ‘Output File:’. Use this box to name the data file and a text file will be made in the same folder that you have saved your previous PA files the next time you **Fly’m**.
        ii. The output of this text file also appears in the ‘Log’ tab in the workbench.
4. The files from this test and associated manual files are located in the folder ‘simion3d 7.0’ (this was performed using SIMION 8, but the SIMION 8 folder is in the ‘simion3d 7.0’ folder). This folder contains a complete manual from SIMION 7.0 and select manual sections from SIMION 8.0.

References

1. Akhavan J. *The Chemistry of Explosives*. 2nd Edition ed: The Royal Society of Chemistry; 2004.
2. Brown GI. *The Big Bang a History of Explosives*: Sutton Publishing; 2005.
3. Teipel U. *Energetic Materials*. 5th, Completely Revised Edition ed: Wiley-VCH; 2002.
4. Monteil-Rivera F, Paquet L, Deschamps S, Balakrishnan VK, Beaulieu C, Hawari J. Physico-chemical measurements of CL-20 for environmental applications - Comparison with RDX and HMX. *Journal of Chromatography A* 2004,**1025**:125-132.
5. Fischer SH, Grubelich MC. In: *32nd AIAA/ASME/SAE/ASEE Joint Propulsion Conference*. Lake Buena Vista, FL; 1996.
6. Shimojo F, Nakano A, Kalia RK, Vashishta P. Enhanced reactivity of nanoenergetic materials: A first-principles molecular dynamics study based on divide-and-conquer density functional theory. *Applied Physics Letters* 2009,**95**.
7. Levitas VI, Pantoya ML, Dikici B. Melt dispersion versus diffusive oxidation mechanism for aluminum nanoparticles: Critical experiments and controlling parameters. *Applied Physics Letters* 2008,**92**.
8. Dutro GM, Yetter RA, Risha GA, Son SF. The effect of stoichiometry on the combustion behavior of a nanoscale Al/MoO3 thermite. *Proceedings of the Combustion Institute* 2009,**32**:1921-1928.
9. Huang Y, Risha GA, Yang V, Yetter RA. Combustion of bimodal nano/micron-sized aluminum particle dust in air. *Proceedings of the Combustion Institute* 2007,**31**:2001-2009.
10. Huang Y, Risha GA, Yang V, Yetter RA. Effect of particle size on combustion of aluminum particle dust in air. *Combustion and Flame* 2009,**156**:5-13.
11. Sullivan K. Ignition, Combustion and Tuning of Nanocomposite Thermites. College Park: University of Maryland; 2010.
12. Levitas VI, Asay BW, Son SF, Pantoya M. Melt dispersion mechanism for fast reaction of nanothermites. *Applied Physics Letters* 2006,**89**.
13. Rai A, Park K, Zhou L, Zachariah MR. Understanding the mechanism of aluminium nanoparticle oxidation. *Combustion Theory and Modelling* 2006,**10**:843-859.
14. Trunov MA, Schoenitz M, Dreizin EL. Effect of polymorphic phase transformations in alumina layer on ignition of aluminium particles. *Combustion Theory and Modelling* 2006,**10**:603-623.
15. Galvez-Ruiz JC, Holl G, Karaghiosoff K, Klapotke TM, Lohnwitz K, Mayer P, *et al.* Derivatives of 1,5-diamino-1H-tetrazole: A new family of energetic heterocyclic-based salts. *Inorganic Chemistry* 2005,**44**:4237-4253.
16. Brill TB, Beckstead MC, Flanagan JE, Lin MC, Litzinger TA, Waesche RHW, *et al.* Chemical speciation and dynamics in the surface combustion zone of energetic materials. *Journal of Propulsion and Power* 2002,**18**:824-834.

17. Schoenitz M, Umbrajkar S, Dreizin EL. Kinetic analysis of thermite reactions in Al-MoO3 nanocomposites. *Journal of Propulsion and Power* 2007,**23**:683-687.
18. Umbrajkar SM, Schoenitz M, Dreizin EL. Exothermic reactions in Al-CuO nanocomposites. *Thermochimica Acta* 2006,**451**:34-43.
19. Choi Y, Jung M, Lee YK. Effect of Heating Rate on the Activation Energy for Crystallization of Amorphous Ge2Sb2Te5 Thin Film. *Electrochemical and Solid State Letters* 2009,**12**:F17-F19.
20. Park K, Lee D, Rai A, Mukherjee D, Zachariah MR. Size-resolved kinetic measurements of aluminum nanoparticle oxidation with single particle mass spectrometry. *Journal of Physical Chemistry B* 2005,**109**:7290-7299.
21. Bazyn T, Krier H, Glumac N. Combustion of nanoaluminum at elevated pressure and temperature behind reflected shock waves. *Combustion and Flame* 2006,**145**:703-713.
22. Zhou L, Piekiel N, Chowdhury S, Zachariah MR. T-Jump/time-of-flight mass spectrometry for time-resolved analysis of energetic materials. *Rapid Communications in Mass Spectrometry* 2009,**23**:194-202.
23. Van Dusen MS. Platinum Resistance Thermometry at Low Temperatures. *Journal of the American Chemical Society* 1925,**47**:326.
24. Nicholas JV, White DR. *Traceable Temperatures*. 2nd Edition ed: John Wiley and Sons Ltd; 2001.
25. Chowdhury S, Sullivan K, Piekiel N, Zhou L, Zachariah MR. Diffusive vs. Explosive Reaction at the Nanoscale. *J. Phys. Chem. Lett. in press* 2010.
26. Klapotke TM, Stierstorfer J. Azidoformamidinium and 5-aminotetrazolium dinitramide-two highly energetic isomers with a balanced oxygen content. *Dalton Transactions* 2009:643-653.
27. Klapotke TM, Mayer P, Schulz A, Weigand JJ. 1,5-Diamino-4-methyltetrazolium dinitramide. *Journal of the American Chemical Society* 2005,**127**:2032-2033.
28. Klapotke TM, Stierstorfer J. The new energetic compounds 1,5-diaminotetrazolium and 5-amino-1-methyltetrazolium dinitramide - Synthesis, characterization and testing. *European Journal of Inorganic Chemistry* 2008:4055-4062.
29. Zhou L, Piekiel N, Chowdhury S, Lee D, Zachariah MR. Transient ion ejection during nanocomposite thermite reactions. *Journal of Applied Physics* 2009,**106**.
30. Dahl DA. *Simion 8*. Ringoes, NJ: Scientific Instrument Services, Inc.
31. Puszynski JA. Processing and characterization of aluminum-based nanothermites. *Journal of Thermal Analysis and Calorimetry* 2009,**96**:677-685.
32. Son SF, Yetter RA, Yang V. Introduction: Nanoscale composite energetic materials. *Journal of Propulsion and Power* 2007,**23**:643-644.
33. Mei J, Halldearn RD, Xiao P. Mechanisms of the aluminium-iron oxide thermite reaction. *Scripta Materialia* 1999,**41**:541-548.
34. Ostmark H, Roman N. LASER IGNITION OF PYROTECHNIC MIXTURES - IGNITION MECHANISMS. *Journal of Applied Physics* 1993,**73**:1993-2003.
35. Granier JJ, Pantoya ML. Laser ignition of nanocomposite thermites. *Combustion and Flame* 2004,**138**:373-383.

36. Yang Y, Sun Z, Wang S, Dlott DD. Fast Spectroscopy of Laser-Initiated Nanoenergetic Materials. *J. Phys. Chem. B* 2003,**107**:4485-4493.
37. Moore DS, Son SE, Asay BW. Time-resolved spectral emission of deflagrating nano-Al and nano-MoO3 metastable interstitial composites. *Propellants Explosives Pyrotechnics* 2004,**29**:106-111.
38. Trenkle JC, Koerner LJ, Tate MW, Gruner SM, Weihs TP, Hufnagel TC. Phase transformations during rapid heating of Al/Ni multilayer foils. *Applied Physics Letters* 2008,**93**.
39. Brill TB, Arisawa H, Brush PJ, Gongwer PE, Williams GK. Surface Chemistry of Burning Explosives and Propellants. *J. Phys. Chem.* 1995,**99**:1384-1392.
40. Brill TB, Brush PJ, James KJ, Shepherd JE, Pfeiffer KJ. T-Jump/Ft-Ir Spectroscopy - a New Entry into the Rapid, Isothermal Pyrolysis Chemistry of Solids and Liquids. *Applied Spectroscopy* 1992,**46**:900-911.
41. Zhou L, Piekiel N, Chowdhury S, Zachariah MR. Time-Resolved Mass Spectrometry of the Exothermic Reaction between Nanoaluminum and Metal Oxides: The Role of Oxygen Release. *Journal of Physical Chemistry C* 2010,**114**:14269-14275.
42. Fialkov AB. Investigations on ions in flames. *Progress in Energy and Combustion Science* 1997,**23**:399-528.
43. Filimonov IA, Kidin NI. High-temperature combustion synthesis: Generation of electromagnetic radiation and the effect of external electromagnetic fields (review). *Combustion Explosion and Shock Waves* 2005,**41**:639-656.
44. Henz BJ, Hawa T, Zachariah MR. On the role of built-in electric fields on the ignition of oxide coated nanoaluminum: Ion mobility versus Fickian diffusion. *Journal of Applied Physics* 2010,**107**.
45. Cabrera N, Mott NF. THEORY OF THE OXIDATION OF METALS. *Reports on Progress in Physics* 1948,**12**:163-184.
46. Martirosyan KS, Filimonov IA, Nersesyan MD, Luss D. Electric field formation during combustion of single metal particles. *Journal of the Electrochemical Society* 2003,**150**:J9-J16.
47. Martirosyan KS, Claycomb JR, Miller JH, Luss D. Generation of the transient electrical and spontaneous magnetic fields by solid state combustion. *Journal of Applied Physics* 2004,**96**:4632-4636.
48. Filimonov I, Luss D. Formation of electric potential during the oxidation of a metal particle. *Aiche Journal* 2004,**50**:2287-2296.
49. Martirosyan KS, Setoodeh M, Luss D. Electric-field generated by the combustion of titanium in nitrogen. *Journal of Applied Physics* 2005,**98**.
50. Nersesyan MD, Ritchie JT, Filimonov IA, Richardson JT, Luss D. Electric fields produced by high-temperature metal oxidation. *Journal of the Electrochemical Society* 2002,**149**:J11-J17.
51. Setoodeh M, Martirosyan KS, Lussa D. Electrical pulse formation during high temperature reaction between Ni and Al. *Journal of Applied Physics* 2006,**99**.
52. Martirosyan KS, Wang L, Vicent A, Luss D. Synthesis and performance of bismuth trioxide nanoparticles for high energy gas generator use. *Nanotechnology* 2009,**20**.

53. Munir ZA. The effect of external electric fields on the nature and properties of materials synthesized by self-propagating combustion. *Materials Science and Engineering a-Structural Materials Properties Microstructure and Processing* 2000,**287**:125-137.
54. Carleton FB, Weinberg FJ. ELECTRIC FIELD-INDUCED FLAME CONVECTION IN THE ABSENCE OF GRAVITY. *Nature* 1987,**330**:635-636.
55. Weinberg F, Carleton F, Dunn-Rankin D. Electric field-controlled mesoscale burners. *Combustion and Flame* 2008,**152**:186-193.
56. Rosenband V. Thermo-mechanical aspects of the heterogeneous ignition of metals. *Combustion and Flame* 2004,**137**:366-375.
57. Sanders VE, Asay BW, Foley TJ, Tappan BC, Pacheco AN, Son SF. Reaction propagation of four nanoscale energetic composites (Al/MoO3, Al/WO3, Al/CuO, and Bi2O3). *Journal of Propulsion and Power* 2007,**23**:707-714.
58. Hull S, Norberg ST, Tucker MG, Eriksson SG, Mohn CE, Stolen S. Neutron total scattering study of the delta and beta phases of Bi2O3. *Dalton Transactions* 2009:8737-8745.
59. Shuk P, Wiemhofer HD, Guth U, Gopel W, Greenblatt M. Oxide ion conducting solid electrolytes based on Bi2O3. *Solid State Ionics* 1996,**89**:179-196.
60. Sabioni ACS, Daniel A, Ferraz WB, Pais RWD, Huntz AM, Jomard F. Oxygen Diffusion in Bi2O3-doped ZnO. *Materials Research-Ibero-American Journal of Materials* 2008,**11**:221-225.
61. Ivetic T, Nikolic MV, Slankarnenac M, Zivanov M, Minic D, Nikolic PM, *et al.* Influence of Bi2O3 on microstructure and electrical properties of ZnO-SnO2 ceramics. *Science of Sintering* 2007,**39**:229-240.
62. Takahashi T, Esaka T, Iwahara H. Oxide Ion Conduction in Sintered Oxides of Moo3-Doped Bi2o3. *Journal of Applied Electrochemistry* 1977,**7**:31-35.
63. Martirosyan KS. Nanoenergetic Gas-Generators: principles and applications. *Journal of Materials Chemistry* 2011,**21**:9400-9405.
64. Martirosyan KS, Wang L, Vicent A, Luss D. Nanoenergetic Gas-Generators: Design and Performance. *Propellants Explosives Pyrotechnics* 2009,**34**:532-538.
65. Wang L, Luss D, Martirosyan KS. The behavior of nanothermite reaction based on Bi_2O_3/Al. *Journal of Applied Physics* 2011,**110**:074311.
66. Puszynski JA, Bulian CJ, Swiatkiewicz JJ. Processing and ignition characteristics of aluminum-bismuth trioxide nanothermite system. *Journal of Propulsion and Power* 2007,**23**:698-706.
67. Sullivan KT, Chiou WA, Fiore R, Zachariah MR. In situ microscopy of rapidly heated nano-Al and nano-Al/WO3 thermites. *Applied Physics Letters*,**97**.
68. Sullivan KT, Piekiel NW, Chowdhury S, Wu C, Zachariah MR, Johnson CE. Ignition and Combustion Characteristics of Nanoscale Al/$AgIO_3$: A Potential Energetic Biocidal System. *Combust. Sci. and Tech.* 2011:285-302.
69. Sullivan K, Young G, Zachariah MR. Enhanced reactivity of nano-B/Al/CuO MIC's. *Combustion and Flame* 2009,**156**:302-309.
70. Sullivan K, Piekiel N, Wu C, Chowdhury S, Kelly ST, Hufnagel TC, *et al.* Reactive Sintering: An Important Component in the Combustion of Nanocomposite Thermites. *Combustion and Flame* 2011,**In Press**.

71. Sullivan K, Zachariah MR. Simultaneous Pressure and Optical Measurements of Nanoaluminum Thermites: Investigating the Reaction Mechanism. *Journal of Propulsion and Power In Press* 2010.
72. Anisimova NI, Bordovsky GA, Bordovsky VA, Seldayev VI. Electrical and Thermal Properties of Bi_2O_3, PbO and Mixed Oxides of Bi_2O_3-PbO System. In: *2004 International Conference on Solid Dielectrics*. Toulouse, France; 2004.
73. Denisov VM, Irtyugo LA, Denisova LT. High-Temperature Heat Capacity of Oxides in the Bi_2O_3-SiO_2 and Bi_2O_3-GeO_2 Systems. *Physics of the Solid State* 2011,**53**.
74. Walker P, Tran WH. Handbook of Metal Etchants. In. Edited by CRC; 1991.
75. Kakhan BG, Lazarev VB, Shaplygin IS. Subsolidus Part of the Equilibrium Diagrams of the Bi_2O_3-MO Binary Systems (M = Ni, Cu, or Pd). *Russian Journal of Inorganic Chemistry* 1979,**24**:922-925.
76. Satterfield CN. *Heterogeneous catalysis in industrial practice. 2nd edition*; 1991.
77. Henz BJ, Hawa T, Zachariah MR. On the role of built-in electric fields on the ignition of oxide coated nanoaluminum: Ion mobility versus Fickian diffusion. *Journal of Applied Physics*,**107**.
78. Zhdanov VP, Kasemo B. Cabrera-Mott kinetics of oxidation of nm-sized metal particles. *Chemical Physics Letters* 2008,**452**:285-288.
79. Richter HJ, Knoche KF. REVERSIBILITY OF COMBUSTION PROCESSES. *Acs Symposium Series* 1983,**235**:71-85.
80. Chuang SY, Dennis JS, Hayhurst AN, Scott SA. Development and performance of Cu-based oxygen carriers for chemical-looping combustion. *Combustion and Flame* 2008,**154**:109-121.
81. Shen LH, Wu JH, Xiao J, Song QL, Xiao R. Chemical-Looping Combustion of Biomass in a 10 kW(th) Reactor with Iron Oxide As an Oxygen Carrier. *Energy & Fuels* 2009,**23**:2498-2505.
82. Scott SA, Dennis JS, Hayhurst AN, Brown T. In situ gasification of a solid fuel and CO2 separation using chemical looping. *Aiche Journal* 2006,**52**:3325-3328.
83. Kronberger B, Lyngfelt A, Loffler G, Hofbauer H. Design and fluid dynamic analysis of a bench-scale combustion system with CO2 separation-chemical-looping combustion. *Industrial & Engineering Chemistry Research* 2005,**44**:546-556.
84. Mattisson T, Lyngfelt A, Leion H. Chemical-looping with oxygen uncoupling for combustion of solid fuels. *International Journal of Greenhouse Gas Control* 2009,**3**:11-19.
85. Siriwardane R, Tian HJ, Miller D, Richards G, Simonyi T, Poston J. Evaluation of reaction mechanism of coal-metal oxide interactions in chemical-looping combustion. *Combustion and Flame* 2010,**157**:2198-2208.
86. Piekiel N, Zhou L, Sullivan K, Zachariah MR. Initiation and reaction in Al/Bi2O3 nanothermites: Evidence for Condensed Phase Chemistry In preparation.
87. Brandt O, Roth P. A Tunable Ir-Diode Laser Technique for Measuring Reaction-Rates of High-Temperature Aerosols. *Combustion and Flame* 1989,**77**:69-78.
88. Park C, Appleton JP. Shock-Tube Measurements of Soot Oxidation Rates. *Combustion and Flame* 1973,**20**:369-379.

89. Gilot P, Bonnefoy F, Marcuccilli F, Prado G. Determination of Kinetic Data for Soot Oxidation - Modeling of Competition between Oxygen Diffusion and Reaction During Thermogravimetric Analysis. *Combustion and Flame* 1993,**95**:87-100.
90. Walls JR, Stricklandconstable RF. Oxidation of Carbon between 1000-Degrees-C and 2400-Degrees-C. *Carbon* 1964,**1**:333-&.
91. Neeft JPA, Nijhuis TX, Smakman E, Makkee M, Moulijn JA. Kinetics of the oxidation of diesel soot. *Fuel* 1997,**76**:1129-1136.
92. Higgins KJ, Jung HJ, Kittelson DB, Roberts JT, Zachariah MR. Size-selected nanoparticle chemistry: Kinetics of soot oxidation. *Journal of Physical Chemistry A* 2002,**106**:96-103.
93. Ozawa T. A New Method of Analyzing Thermogravimetric Data. *Bulletin of the Chemical Society of Japan* 1965,**38**:1881-&.
94. Vyazovkin S, Sbirrazzuoli N. Isoconversional kinetic analysis of thermally stimulated processes in polymers. *Macromolecular Rapid Communications* 2006,**27**:1515-1532.
95. Sbirrazzuoli N, Girault Y, Elegant L. Simulations for evaluation of kinetic methods in differential scanning calorimetry .3. Peak maximum evolution methods and isoconversional methods. *Thermochimica Acta* 1997,**293**:25-37.
96. Mikaia A, Zaikin V, Little J, Zhu D, Clifton C, Sparkman D. NIST/EPA/NIH Mass Spectral Library. In: Standard Reference Data Program of the National Institute of Standards and Technology; 2005.
97. Fried LE, Glaesemann KR, Howard WM, Souers PC, Vitello PA. CHEETAH 4.0. In. Edited by Laboratory LLN; 2004.
98. Chadda D, Ford JD, Fahim MA. CHEMICAL ENERGY-STORAGE BY THE REACTION CYCLE CUO/CU2O. *International Journal of Energy Research* 1989,**13**:63-73.
99. Jian G, Zhou L, Piekiel NW, Zachariah MR. Probing Oxygen Release Kinetics of Nanosized Metal Oxides by Temperature-Jump Time of Flight Mass Spectrometry. In: *Fall Technical Meeting of the Eastern States Section of the Combustion Institute*. Storrs, CT; 2011.
100. Klapotke TM. New Nitrogen-Rich High Explosives. *Structure and Bonding* 2007,**125**:85-121.
101. Ma GX, Zhang TL, Zhang JG, Yu KB. Thermal decomposition and molecular structure of 5-aminotetrazolium nitrate. *Thermochimica Acta* 2004,**423**:137-141.
102. Lesnikovich AI, Ivashkevich OA, Levchik SV, Balabanovich AI, Gaponik PN, Kulak AA. Thermal decomposition of aminotetrazoles. *Thermochimica Acta* 2002,**388**:233-251.
103. Paul KW, Hurley MM, Irikura KK. Unimolecular Decomposition of 5-Aminotetrazole and its Tautomer 5-Iminotetrazole: New Insight from Isopotential Searching. *Journal of Physical Chemistry A* 2009,**113**:2483-2490.
104. Chowdhury A, Thynell ST, Lin P. Confined rapid thermolysis/FTIR/ToF studies of tetrazolium-based energetic ionic liquids. *Thermochimica Acta* 2009,**485**:1-13.

105. Brill TB, Ramanathan H. Thermal decomposition of energetic materials 76. Chemical pathways that control the burning rates of 5-aminotetrazole and its hydrohalide salts. *Combustion and Flame* 2000,**122**:165-171.
106. Kiselev VG, Gritsan NP. Theoretical Study of the 5-Aminotetrazole Thermal Decomposition. *Journal of Physical Chemistry A* 2009,**113**:3677-3684.
107. Fischer G, Holl G, Klapotke TM, Weigand JJ. A study on the thermal decomposition behavior of derivatives of 1,5-diamino-1H-tetrazole (DAT): A new family of energetic heterocyclic-based salts. *Thermochimica Acta* 2005,**437**:168-178.
108. Piekiel NW, Cavicchi RE, Zachariah MR. Rapid-Heating of Energetic Materials using a Micro-Differential Scanning Calorimeter. *Thermochimica Acta* 2011,**521**:125.
109. Bottaro JC, Penwell PE, Schmitt RJ. 1,1,3,3-tetraoxo-1,2,3-triazapropene anion, a new oxy anion of nitrogen: The dinitramide anion and its salts. *Journal of the American Chemical Society* 1997,**119**:9405-9410.
110. Linn SH, Ng CY. Photo-Ionization Study of Co2, N2o Dimers and Clusters. *Journal of Chemical Physics* 1981,**75**:4921-4926.
111. Illies AJ. Thermochemistry for the Gas-Phase Ion Molecule Clustering of Co2+Co2, So2+Co2, N2o+N2o, O2+Co2, No+Co2, O2+N2o, and No+N2o - Description of a New Hybrid Drift Tube Ion-Source with Coaxial Electron-Beam and Ion Exit Apertures. *Journal of Physical Chemistry* 1988,**92**:2889-2896.
112. Coe JV, Snodgrass JT, Freidhoff CB, McHugh KM, Bowen KH. Photoelectron-Spectroscopy of the Negative Cluster Ions No-(N2o)N=1,2. *Journal of Chemical Physics* 1987,**87**:4302-4309.
113. Papai I, Stirling A. The covalently bound N3O2 molecule: Two possible isomers. *Chemical Physics Letters* 1996,**253**:196-200.
114. Snis A, Panas I. Characterizations of (NO)(3)- and N3O2- molecular anions. *Chemical Physics Letters* 1999,**305**:285-292.
115. Torchia JW, Sullivan KO, Sunderlin LS. Thermochemistry of N3O2. *Journal of Physical Chemistry A* 1999,**103**:11109-11114.
116. Alijah A, Kryachko ES. On the N3O2- paradigm. *Journal of Molecular Structure* 2007,**844**:193-199.
117. Yang R, Thakre P, Yang V. Thermal decomposition and combustion of ammonium dinitramide (review). *Combustion Explosion and Shock Waves* 2005,**41**:657-679.
118. Rahm M, Brinck T. On the Anomalous Decomposition and Reactivity of Ammonium and Potassium Dinitramide. *Journal of Physical Chemistry A*,**114**:2845-2854.
119. Vyazovkin S, Wight CA. Thermal decomposition of ammonium dinitramide at moderate and high temperatures. *Journal of Physical Chemistry A* 1997,**101**:7217-7221.
120. Singh RP, Verma RD, Meshri DT, Shreeve JM. Energetic nitrogen-rich salts and ionic liquids. *Angewandte Chemie-International Edition* 2006,**45**:3584-3601.
121. Kissinger HE. Reaction Kinetics in Differential Thermal Analysis. *Analytical Chemistry* 1957,**29**:1702-1706.

122. Denlinger DW, Abarra EN, Allen K, Rooney PW, Messer MT, Watson SK, *et al.* Thin-Film Microcalorimeter for Heat-Capacity Measurements from 1.5-K to 800-K. *Review of Scientific Instruments* 1994,**65**:946-958.
123. Lai SL, Ramanath G, Allen LH, Infante P. Heat capacity measurements of Sn nanostructures using a thin-film differential scanning calorimeter with 0.2 nJ sensitivity. *Applied Physics Letters* 1997,**70**:43-45.
124. Olson EA, Efremov MY, Kwan AT, Lai S, Petrova V, Schiettekatte F, *et al.* Scanning calorimeter for nanoliter-scale liquid samples. *Applied Physics Letters* 2000,**77**:2671-2673.
125. Cavicchi RE, Poirier GE, Tea NH, Afridi M, Berning D, Hefner A, *et al.* Micro-differential scanning calorimeter for combustible gas sensing. *Sensors and Actuators B-Chemical* 2004,**97**:22-30.
126. Cook LP, Cavicchi RE, Bassim N, Eustis S, Wong-Ng W, Levin I, *et al.* Enhanced mass transport in ultrarapidly heated Ni/Si thin-film multilayers. *Journal of Applied Physics* 2009,**106**.
127. Certain commercial instruments or materials are identified to adequately specify the experimental procedure. In no case does such identification imply endorsement by the National Institute of Standards and Technology. This statement applies to all instruments mentioned in this article.
128. Osborne KL, III. Temperature-Dependence of the Contact Angle of Water on Graphite, Silicon, and Gold: Worcester Polytechnic Institute; 2009:84.
129. Coutant RW, Penski EC. Experimental Evaluation of Mass-Transfer from Sessile Drops. *Industrial & Engineering Chemistry Fundamentals* 1982,**21**:250-254.
130. Lide DR. *CRC Handbook of Chemistry and Physics*; 2002.
131. NBS-ICTA Standard Reference Material 758: DTA Temperature Standards (125 - 435 ^{o}C). In. Edited by Materials OoSR; 1971.
132. Kumar N, Nath R. Thermal and ferroelectric properties of potassium nitrate: Polyvinyl fluoride composite films. *Ieee Transactions on Dielectrics and Electrical Insulation* 2005,**12**:1145-1150.
133. *The Handbook of Photonics: Second Edition*: CRC Press; 2007.
134. Jordan TOF Products I. Instruction Manual: 25mm MCP Microchannel Plate Z-Gap Detector. In; 2012.
135. Barnstedt J. Advanced Practical Course: Microchannel Plate Detectors. *Kepler Center for Astro and Particle Physics* 2009.
136. Park K, Rai A, Zachariah MR. Characterizing the coating and size-resolved oxidative stability of carbon-coated aluminum nanoparticles by single-particle mass-spectrometry. *Journal of Nanoparticle Research* 2006,**8**:455-464.
137. Ermoline A, Schoenitz M, Dreizin EL. Reactions leading to ignition in fully dense nanocomposite Al-oxide systems. *Combustion and Flame* 2011,**158**:1076-1083.
138. Ermoline A, Stamatis D, Dreizin EL. Low-temperature exothermic reactions in fully dense Al–CuO nanocomposite powders. *Thermochimica Acta* 2012:52-58.